

Nonlinear Finite Element Analysis and Design Optimization
of Thin-Walled Structures

Peyman Khosravi

A Thesis
in
The Department
of
Mechanical and Industrial Engineering

Presented in Partial Fulfillment of the Requirements
for the Degree of Doctor of Philosophy at
Concordia University
Montreal, Quebec, Canada

June 2007

© Peyman Khosravi, 2007



Library and
Archives Canada

Bibliothèque et
Archives Canada

Published Heritage
Branch

Direction du
Patrimoine de l'édition

395 Wellington Street
Ottawa ON K1A 0N4
Canada

395, rue Wellington
Ottawa ON K1A 0N4
Canada

Your file Votre référence

ISBN: 978-0-494-31149-3

Our file Notre référence

ISBN: 978-0-494-31149-3

NOTICE:

The author has granted a non-exclusive license allowing Library and Archives Canada to reproduce, publish, archive, preserve, conserve, communicate to the public by telecommunication or on the Internet, loan, distribute and sell theses worldwide, for commercial or non-commercial purposes, in microform, paper, electronic and/or any other formats.

The author retains copyright ownership and moral rights in this thesis. Neither the thesis nor substantial extracts from it may be printed or otherwise reproduced without the author's permission.

AVIS:

L'auteur a accordé une licence non exclusive permettant à la Bibliothèque et Archives Canada de reproduire, publier, archiver, sauvegarder, conserver, transmettre au public par télécommunication ou par l'Internet, prêter, distribuer et vendre des thèses partout dans le monde, à des fins commerciales ou autres, sur support microforme, papier, électronique et/ou autres formats.

L'auteur conserve la propriété du droit d'auteur et des droits moraux qui protègent cette thèse. Ni la thèse ni des extraits substantiels de celle-ci ne doivent être imprimés ou autrement reproduits sans son autorisation.

In compliance with the Canadian Privacy Act some supporting forms may have been removed from this thesis.

Conformément à la loi canadienne sur la protection de la vie privée, quelques formulaires secondaires ont été enlevés de cette thèse.

While these forms may be included in the document page count, their removal does not represent any loss of content from the thesis.

Bien que ces formulaires aient inclus dans la pagination, il n'y aura aucun contenu manquant.


Canada

Abstract

Nonlinear Finite Element Analysis and Design Optimization of Thin-Walled Structures

Peyman Khosravi, Ph.D.

Concordia University, 2007

In this study, an efficient, accurate and robust methodology for nonlinear finite element analysis and design optimization of thin-walled structures is presented. Main parts of this research are: formulation and development of an accurate and efficient shell element, a robust nonlinear finite element analysis technique, and an efficient optimization methodology. In the first part, a new three-node triangular shell element is developed by combining the optimal membrane element and discrete Kirchhoff triangle (DKT) plate bending element, and is then modified for laminated composite plates and shells so as to include the membrane-bending coupling effect. Also, a moderately thick shell element is developed in a similar manner by combining the discrete Kirchhoff-Mindlin triangular (DKMT) plate bending element and the optimal membrane element. Using appropriate shape functions for the bending and membrane modes of the element, the “inconsistent” stress stiffness matrix is formulated and the

tangent stiffness matrix is determined. In the second part, a robust nonlinear finite element analysis program based on the corotational technique is developed to analyze thin-walled structures with geometric nonlinearity. The new element is thoroughly tested by solving few popular benchmark problems. The results of the analyses are compared with those obtained based on other membrane elements. In the third part, optimization algorithms based on the optimality criteria are developed and then combined with the nonlinear finite element analysis to optimize different types of thin-walled structures with geometric nonlinearity. The optimization problem considers the thickness or geometry design variables, and aims to maximize the critical load of the structure subject to constant total mass, or minimize the total mass subject to constant applied loads. The optimization results based on the developed design optimization algorithm are compared with those based on the gradient-based sequential quadratic programming method to demonstrate the efficiency and accuracy of the developed procedure. An application of the thickness optimization for locating the potential places to add the stiffeners in stiffened panels is also presented. Also a method is presented to efficiently incorporate the effects of local buckling and mode switching during optimization process for stiffened panels.

Acknowledgements

First and foremost, I want to express my gratitude to my supervisors Dr. Sedaghati and Dr. Ganesan for their valuable technical advice, and also for financial support during my research. I would also like to extend my thanks to Dr. Bhat, Dr. Hoa, Dr. Pekau, and Dr. Taheri for taking the time to review my work and serve on my committee.

During my work, I found Dr. Sedaghati's passion beyond the responsibilities of a supervisor. For a student, no support is more valuable and more effective than being constantly encouraged by his advisor. Again, thank you Ramin for your support and for believing in me. I really mean it.

I was fortunate to have good friends among the students in Concordia. I wish them all the best, and I hope we stay in contact for a long time to come.

Eugenie's friendship during these years was priceless. She has always supported me in doing what I liked to do. I cannot thank her enough.

I dedicate this thesis to Eugenie for her friendship, and for our adventurous life between 1998 and 2003.

Vincent (Al Pacino): I don't know how to do anything else.

Neil (Robert De Niro): Neither do I.

Vincent (Al Pacino): I don't much want to either.

Neil (Robert De Niro): Neither do I.

From the movie “Heat”.

Contents

| | |
|--|-------------|
| List of Figures | xii |
| Nomenclature | xvii |
| 1 Introduction | 1 |
| 1.1 Background and motivation | 1 |
| 1.2 Literature survey | 4 |
| 1.2.1 Facet triangular elements | 4 |
| 1.2.2 Geometrically nonlinear analysis | 6 |
| 1.2.3 Structural design optimization | 9 |
| 1.3 Objective and scope of present research | 11 |
| 1.4 Thesis organization | 14 |
| 2 Finite Element Formulation of the New Shell Element | 16 |
| 2.1 Introduction | 16 |
| 2.2 Definition of geometric parameters | 16 |
| 2.3 Formulation of OPT membrane element | 17 |
| 2.4 Formulation of the DKT plate bending element | 21 |
| 2.5 Shell element formulation | 23 |
| 2.6 Extension to the thick shell element | 25 |
| 2.7 Stress stiffness formulation | 27 |

| | | |
|----------|---|-----------|
| 3 | Solutions of Nonlinear Finite Element Equations | 31 |
| 3.1 | Introduction | 31 |
| 3.2 | Concept of “time” in static analysis | 32 |
| 3.3 | Tangent and secant stiffness | 33 |
| 3.4 | Static analysis | 33 |
| 3.5 | Iterative methods for solving nonlinear equations | 34 |
| 3.5.1 | Direct iteration | 35 |
| 3.5.2 | Newton-Raphson (NR) scheme | 38 |
| 3.5.3 | Modified Newton-Raphson (MNR) scheme | 38 |
| 3.5.4 | Quasi-Newton (QN) scheme | 41 |
| 3.6 | Incremental control techniques | 41 |
| 3.6.1 | Force control | 41 |
| 3.6.2 | Displacement control | 42 |
| 3.6.3 | Arc-length control | 43 |
| 3.7 | Convergence criteria | 45 |
| 3.7.1 | Displacement convergence | 46 |
| 3.7.2 | Force convergence | 46 |
| 3.7.3 | Energy convergence | 46 |
| 3.8 | Corotational nonlinear analysis | 47 |
| 3.9 | Computation for critical points | 54 |
| 4 | Structural Design Optimization | 57 |
| 4.1 | Introduction | 57 |
| 4.2 | Geometry and thickness design variables | 57 |

| | | |
|----------|--|-----------|
| 4.3 | Optimization problem | 61 |
| 4.4 | Sensitivity analysis | 62 |
| 4.5 | Optimality criteria for load–capacity maximization of thin-walled structures, subject to constant mass | 65 |
| 4.5.1 | Derivation of the optimality criteria | 65 |
| 4.5.2 | Recurrence relation | 69 |
| 4.5.3 | Strain energy | 70 |
| 4.6 | Optimality criteria for mass minimization of thin-walled structures subject to constant load | 71 |
| 4.7 | Thickness optimization of a plate and its application in optimum design of stiffened panels | 76 |
| 4.8 | Shape optimization of stiffened panels considering local buckling | 81 |
| 4.8.1 | Buckling modes of stiffened panels | 81 |
| 4.8.2 | Bifurcation buckling and modification of the optimization algorithm | 83 |
| 5 | Numerical Examples | 87 |
| 5.1 | Validation of the proposed shell element for thin-walled structures | 87 |
| 5.1.1 | Cantilever plate subjected to end moment | 88 |
| 5.1.2 | Elastica problem | 89 |
| 5.1.3 | Cantilever plate subjected to end shear force | 90 |
| 5.1.4 | Cantilever subjected to end in-plane shear force | 94 |
| 5.1.5 | Cantilever isotropic angle subjected to end shear force | 94 |
| 5.1.6 | Cantilever stiffened plate subjected to end shear force | 95 |

| | | |
|-------|--|-----|
| 5.2 | Validation of the proposed shell element for thick structures | 96 |
| 5.2.1 | Square unsymmetric laminate with simple supports subjected to shear and biaxial compression | 97 |
| 5.2.2 | Cantilever laminated angle subjected to end shear force | 98 |
| 5.2.3 | Thick cantilever beam subjected to end shear force | 99 |
| 5.2.4 | Shallow shell under uniformly distributed transverse load | 102 |
| 5.3 | Numerical results for shape optimization | 104 |
| 5.3.1 | Shape optimization of a shallow spherical shell: mass minimiza- tion subject to the constant load | 104 |
| 5.3.2 | Width optimization of a cantilever plate: mass minimization subject to the constant load | 106 |
| 5.3.3 | Width optimization of a shallow arch: mass minimization sub- ject to the constant load | 109 |
| 5.3.4 | Thickness optimization of a shallow arch: limit load maximiza- tion subject to the constant mass | 111 |
| 5.3.5 | Width optimization of a shallow arch: bifurcation load maxi- mization subject to the constant mass | 113 |
| 5.3.6 | Thickness optimization of a cantilever plate: load maximization subject to the constant mass | 116 |
| 5.3.7 | Thickness optimization of a simply supported square plate: load maximization subject to the constant mass | 118 |

| | | |
|----------|--|------------|
| 5.3.8 | Thickness optimization and rib location for a simply supported square plate with square hole: load maximization subject to the constant mass | 121 |
| 5.3.9 | Thickness optimization and rib location for a simply supported square plate with square hole under downward surface load: load maximization subject to the constant mass | 124 |
| 5.4 | Shape optimization of stiffened panels considering local buckling . . . | 127 |
| 5.4.1 | One-variable design of a stiffened panel | 127 |
| 5.4.2 | Multi-variable design of a stiffened panel | 131 |
| 6 | Discussions, Contributions and Conclusions, Future Work, and Publications | 133 |
| 6.1 | Discussions | 133 |
| 6.2 | Contributions and conclusions | 134 |
| 6.3 | Future work | 137 |
| 6.4 | Publications | 138 |
| | References | 141 |

List of Figures

| | | |
|------|---|----|
| 1.1 | Design optimization algorithm for nonlinear structures | 2 |
| 1.2 | Different parts of the present work | 12 |
| 2.1 | Geometry of the triangular element | 17 |
| 3.1 | Snap-through and snap-back behaviors. | 32 |
| 3.2 | Tangent and secant stiffness matrices. | 33 |
| 3.3 | Direct iteration method. | 36 |
| 3.4 | Newton-Raphson iterative method. | 37 |
| 3.5 | Modified Newton-Raphson iterative method. | 39 |
| 3.6 | Quasi-Newton iterative method. | 40 |
| 3.7 | Incremental control techniques: force control (a), displacement control (b), and arc-length control (c). | 42 |
| 3.8 | Arc-length control technique. | 44 |
| 3.9 | Corotational method | 48 |
| 3.10 | Coplanar corotated and current configurations | 50 |
| 3.11 | Flowchart of the corotational nonlinear analysis | 53 |
| 3.12 | Equilibrium paths and critical points. | 55 |
| 3.13 | Two forms of the nonlinear response curve with limit load | 56 |

| | | |
|------|---|-----|
| 4.1 | Geometry and thickness design variables. | 58 |
| 4.2 | Nodal coordinate as the geometry design variable. | 58 |
| 4.3 | Various forms to define the geometry design variables. | 59 |
| 4.4 | Various forms to define the geometry design variable a in Figure 4.1. | 59 |
| 4.5 | Concept of thickness optimization subject to constant volume. | 77 |
| 4.6 | Identifying potential locations for stiffeners using thickness optimization. | 79 |
| 4.7 | Primary buckling modes of a stiffened panel subject to compressive loads [159]. | 81 |
| 4.8 | Behavior of the perfect and imperfect stiffened panels. | 83 |
| 4.9 | Algorithms for optimization of nonlinear structures. | 85 |
| 4.10 | Discretized panel module used in finite element analysis. | 86 |
| 5.1 | Cantilever plate subjected to end moment | 88 |
| 5.2 | Elastica problem | 90 |
| 5.3 | Cantilever plate subjected to end shear force | 92 |
| 5.4 | Cantilever subjected to end in-plane shear force | 93 |
| 5.5 | Cantilever angle subjected to end shear force | 95 |
| 5.6 | Cantilever stiffened plate subjected to end shear force | 96 |
| 5.7 | Response of the square unsymmetric $[0/90]_8$ laminate subjected to shear and biaxial compression. | 97 |
| 5.8 | Cantilever laminated angle subjected to end shear force. | 99 |
| 5.9 | Response of the cantilever laminated angle (at the tip corner where the load is applied) subjected to end shear force modeled by 40 and 160 elements. | 100 |

| | |
|--|-----|
| 5.10 Thick cantilever beams modeled by triangular shell elements. | 101 |
| 5.11 Nonlinear response of the thick cantilever plates. | 102 |
| 5.12 Shallow shell under downward uniformly distributed load. | 103 |
| 5.13 Response of the shallow shell modeled by 40 and 320 elements. | 103 |
| 5.14 Shallow spherical shell subject to transverse load | 105 |
| 5.15 Optimum shape, and variation of the mass and bending energy ratio for the dome shell (thickness scaling) | 106 |
| 5.16 Cantilever plate with end load | 107 |
| 5.17 Optimum shape and variation of the mass and energy density for the cantilever plate | 108 |
| 5.18 Shallow arch under downward loads | 108 |
| 5.19 Optimum shapes and variation of the mass for shallow shell (present study vs SQP method) | 110 |
| 5.20 Shallow arch subjected to concentrated vertical loads. | 110 |
| 5.21 Optimum results of the thickness optimization (<i>cm</i>) for the shallow arch of Figure 5.20 subject to the constant mass (thicknesses have been exaggerated for better view.) | 111 |
| 5.22 Variation of the critical load (limit load) during the thickness opti- mization for the shallow arch of Figure 5.20. | 112 |
| 5.23 Variation of \tilde{e} during the thickness optimization for the shallow arch of Figure 5.20. | 112 |
| 5.24 Shallow arch made of two different materials under top concentrated vertical loads. | 113 |

| | |
|--|-----|
| 5.25 Limit and bifurcation points for the shallow arch in Figure 5.24 (before optimization.) | 114 |
| 5.26 Results of the shape (width) optimization for the shallow arch in Figure 5.24 subject to constant mass. | 115 |
| 5.27 Variation of the critical load (bifurcation load) during the width optimization for the shallow arch in Figure 5.24. | 115 |
| 5.28 Cantilever plate subject to axial and shear forces at the tip. | 116 |
| 5.29 Variation of the thickness over the length of the cantilever plate of Figure 5.28 after optimization. | 117 |
| 5.30 Nonlinear behavior of the cantilever plate of Figure 5.28 before and after optimization. | 117 |
| 5.31 Square plate with simple supports subjected to biaxial compressive forces. | 118 |
| 5.32 Results of thickness optimization (cm) for a quarter of the plate shown in Figure 5.31: (a) UASEV criterion. (b) USED criterion. | 119 |
| 5.33 Change of load carrying capacity of the plate shown in Figure 5.31 during the thickness optimization using USED and UASEV criteria. | 120 |
| 5.34 Square plate with a square hole in the center, and simple supports, subjected to biaxial compressive forces. | 121 |
| 5.35 Result of thickness optimization (cm) for a quarter of the plate shown in Figure 5.34. Thicknesses of the sections have been exaggerated for better view. | 122 |

| | | |
|------|---|-----|
| 5.36 | A quarter of the plate shown in Figure 5.34 with stiffeners at potential locations. Numbers show the height of the stiffeners (cm). | 123 |
| 5.37 | Result of thickness optimization (cm) for a quarter of the plate shown in Figure 5.34 with hinged supports ($u = v = w = 0$ at the edges) under the downward surface pressure load. Thicknesses of the sections have been exaggerated for better view. | 125 |
| 5.38 | A quarter of the plate in Figure 5.34 with hinged supports under the downward surface with stiffeners at potential locations. Numbers show the height of the stiffeners (cm). | 125 |
| 5.39 | A quarter of the plate in Figure 5.34 with hinged supports under the downward surface and stiffeners at potential locations after the second rounds of rib locating. Numbers show the height of the stiffeners (cm). | 126 |
| 5.40 | Stiffened panel under axial load. | 127 |
| 5.41 | Results of the analysis of the stiffened panel of Figure 5.40 for different values of t_p (mm) | 128 |
| 5.42 | Buckling modes and yielded regions for the stiffened panel in Figure 5.40. | 128 |
| 5.43 | Iteration history for the multi-variable design optimization of a stiffened panel. | 130 |
| 5.44 | Change of the nonlinear behavior during the multi-variable design optimization of a stiffened panel. | 130 |

Nomenclature

Roman Symbols

| | |
|-------------|--|
| A | element area |
| A^e | stretching stiffness matrix |
| B_b | strain–displacement matrix for bending deformation in DKT element |
| B_b° | strain–displacement matrix for bending deformation in DKMT element |
| B_s° | strain-nodal displacement matrix for shear deformation in DKMT element |
| B^e | membrane-bending coupling stiffness matrix |
| B_m | strain–displacement matrix for membrane deformation in OPT element |
| B_\circ | complete strain–displacement matrix matrix for composite element |
| D^e | bending stiffness matrix (flexural rigidity) |
| D_\circ | complete rigidity matrix for composite element |
| $\{d\}$ | element nodal displacement vector |
| $\{d_b\}$ | element nodal displacement vector for bending deformation |
| $\{d_m\}$ | element nodal displacement vector for membrane deformation |

| | |
|--|---|
| E | elasticity matrix |
| E_o | Young's modulus |
| e | strain energy of the element |
| \tilde{e} | average strain energy variation |
| \hat{e} | average strain energy density |
| e_L | strain energy of the element associated with linear part of strains |
| e_σ | strain energy of the element associated with higher order part of strains |
| F | vector of the internally generated nodal forces |
| F_{cr} | critical load |
| f | vector of the element internal forces |
| J | Jacobian matrix |
| K | stiffness matrix |
| K_b | stiffness matrix of DKT element |
| K_b° | stiffness matrix of DKMT element |
| K_m | stiffness matrix of OPT membrane element |
| $K_{mb}, K_{bm}, K_{mb}^\circ, K_{bm}^\circ$ | membrane-bending coupling stiffness matrices |
| K_{basic} | basic stiffness matrix for OPT element |
| $K_{higher\ order}$ | higher order stiffness matrix for OPT element |

| | |
|--------------------|---|
| K_S | secant stiffness matrix |
| K_σ | stress stiffness matrix |
| L | Lagrangian |
| M | total mass |
| M_0 | constant value of the total mass |
| M_x, M_y, M_{xy} | moment resultants |
| m | number of the nodal displacement components |
| N_x, N_y, N_{xy} | in-plane force resultants |
| P | projection matrix |
| P_B | lowest buckling load |
| P_L | limit load of the imperfect structure |
| p | pseudo-load vector |
| Q_x, Q_y | transverse shear resultants |
| q | constant reference applied load vector |
| R | vector of the applied loads |
| r | step size parameter |
| S | new state of nodal triad |
| S_0 | initial state of nodal triad |

| | |
|--|---|
| s | number of shape design variables |
| T_e | transformation matrix for the coordinate system e |
| t | element thickness |
| tol | convergence tolerance |
| U | total strain energy |
| u | complete vector of the nodal displacements |
| u_c | complete vector of the nodal displacements at the critical load level |
| $\bar{u}^{E1}, \bar{u}^{E2}, \bar{u}^{E3}$ | pure nodal displacements in the current local direction |
| V | volume |
| X | vector of the shape design variables |
| X_L | lower bound on the shape design variables X |
| X_U | upper bound on the shape design variables X |
| x_* | geometry design variable |
| XYZ | global coordinate system |
| xyz | element local coordinate system |

Greek Symbols

| | |
|------------|---|
| α | step length |
| α_b | free parameter in the basic membrane stiffness matrix |

β scale factor

β_0, \dots, β_9 free parameters in the higher order membrane stiffness matrix

$\{\bar{\gamma}\}$ vector of transverse shear strains

Δl arc length

$\{\varepsilon_b\}$ vector of bending strains

ε_d displacement tolerance

ε_e energy tolerance

ε_f force tolerance

$\{\varepsilon_m\}$ vector of membrane strains

$\zeta_1, \zeta_2, \zeta_3$ element area coordinates

η iteration number

$\theta_x, \theta_y, \theta_z$ nodal rotations about local axes x, y , and z

$\theta^{E_1}, \theta^{E_2}, \theta^{E_3}$ pure nodal rotations about axes E_1, E_2 , and E_3

$\tilde{\theta}_X, \tilde{\theta}_Y, \tilde{\theta}_Z$ incremental rotations of nodal triad S about global axes X, Y , and Z

ϑ buckling mode

λ load level multiplier (load level factor)

λ_c critical load level factor

μ Lagrange multiplier

ν Poisson's ratio

Π total potential energy of the structure

Π_{opt} total potential energy of the structure associated with the optimum design

ρ material density

σ_{VM} von Mises stress

ϕ potential energy of the element

φ imperfection

Ω spin tensor

Superscripts

(t) “time” index in nonlinear iterative solutions

Subscripts

i element number

(i) iteration number in nonlinear iterative solutions

x_l geometry design variable index

Acronyms

ANDES Assumed Natural Deviatoric Strain template

BCIZ Bazeley–Cheung–Irons–Zienkiewicz element

DKMT Discrete Kirchhoff–Mindlin Triangle

DKT Discrete Kirchhoff Triangle

FDM Finite Difference Method

LBER Least Bending Energy Ratio criterion

LST(Ret) Retrofitted Linear Strain Triangle

NFEA Nonlinear Finite Element Analysis

OPT OPTimum membrane element

SQP Sequential Quadratic Programming

UASED Uniform Average Strain Energy Density criterion

UASEV Uniform Average Strain Energy Variation criterion

USED Uniform Strain Energy Density criterion

Chapter 1

Introduction

1.1 Background and motivation

Structural optimization improves a design by changing the geometrical properties of the structure considering a set of design constraints. In structural optimization, the thickness, shape or topology of the structure is iteratively changed until an optimal design is achieved [1-7]. Over the past decades, the scope of structural shape optimization has widened considerably, and optimization of structures to have minimum mass or maximum load capacity remains an active area of research.

Thin-walled structures consist of components in the form of plates or shells with small thickness compared to other dimensions. These structures, which are the most efficient among all of the structural systems, may display nonlinear behavior under applied loads. This kind of nonlinearity, which is due to the large deformations in the structure, is called “Geometric nonlinearity”.

Optimization of geometrically nonlinear structures based on the nonlinear mathematical programming techniques involves many evaluations of the objective function and constraints at each optimization iteration before a new search direction and

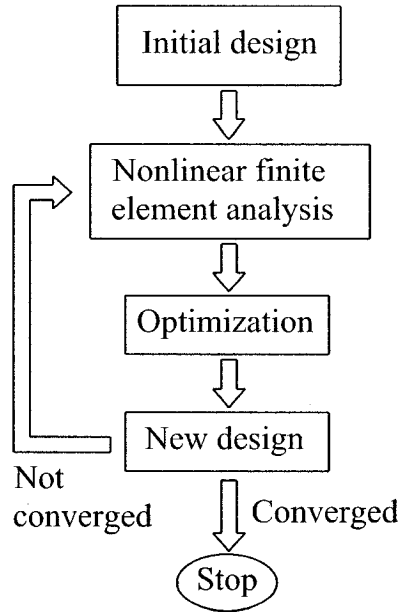


Figure 1.1: Design optimization algorithm for nonlinear structures

step size can be established. This makes the design optimization of nonlinear structures extremely difficult and computationally very expensive as nonlinear analysis by itself is a highly iterative process (Figure 1.1). Developing design optimization techniques that combine together efficiently the iterative optimization process and iterative analysis of nonlinear structures is a challenging and complex task which has not yet received sufficient attention.

Most of the works on the optimization of nonlinear structures subject to system stability constraints have been performed on truss structures considering the cross-sectional areas of the members as the design variables. Relatively few research works have been reported on plate and shell structures, primarily because of the complexity of the buckling analysis. In most of the works, the system stability requirement is posed as a linear buckling analysis in order to increase the efficiency of the optimization process [8-15]. Such an analysis is restricted to small deformations where

linear buckling analysis reduces to the solution of a generalized eigenvalue problem. In the case where the non-linear behavior results in large changes in the geometry of the structure, this definition of system stability may not be conservative [16-18]. As a result, optimization based on the assumption of linearity can lead to unsafe and infeasible designs due to instability problems [19, 20].

Regarding the finite element analysis of plate and shell structures, one of the most popular approaches is to use an assemblage of flat triangular elements as an approximation to the curved surface. A flat shell element can be obtained by combining a membrane and a plate bending element [21-23]. A similar approach has been even applied to curved rods approximated by straight beam elements [24]. The formulation of such flat elements is simple, and computationally more efficient than the curved elements. Most of the flat shell elements available in the literature have been also used for nonlinear analysis because flat elements are not as expensive as the curved elements particularly in iterative nonlinear solutions.

The CST (Constant Strain Triangle) and LST (Linear Strain Triangle) elements are the simplest membrane elements which have been combined frequently with suitable plate bending elements for analysis of plates and shells. Due to the lack of a drilling (or in-plane rotational) degree of freedom, these elements cause rotational singularity in the stiffness matrix. It happens when all the elements sharing one node are coplanar and the local coordinate systems of the elements coincide with the global coordinate system. In this case the global stiffness matrix becomes singular. One way to overcome this problem is to assume a small fictitious stiffness for rotational degree of freedom. Another approach is to use membrane elements with rotational degree

of freedom.

Another problem regarding the flat shell elements is their aspect ratio sensitivity. When modeling a thin-walled structure, it frequently happens for some elements to have a very high or a very low aspect ratio (for example in modeling a stiffened plate). In this case the response of these high or low aspect ratio elements can affect the response of the whole structure significantly. In such cases, the solution converges to the exact result only when a fine mesh is used. However, increasing the number of elements, increases the computational time as well, especially when dealing with nonlinear analysis.

Considering the issues mentioned above, the main objective of this research is to develop an efficient, accurate and robust methodology for design optimization of nonlinear thin-walled structures. Specifically this research aims to develop an accurate and efficient shell element, a robust nonlinear finite element approach, and an efficient optimization algorithm.

1.2 Literature survey

1.2.1 Facet triangular elements

Allman [25] derived the first successful triangular membrane element with in-plane rotational degree of freedom. He later proposed a more complete formulation for this element [26]. Since then, other elements with drilling degree of freedom have been derived but as mentioned before, most of them suffer from aspect ratio locking which means that the response of the element is highly dependent on its geometrical aspect ratio.

Recently, Felippa [27] developed an optimal membrane element (called OPT) with drilling degree of freedom. This element is called “optimal” because for any arbitrary aspect ratio, its response for in-plane pure bending is exact. This element is a LST3/9R membrane element (linear strain triangular membrane element with 3 corner nodes and 9 degrees of freedom, 3 per node, including rotational degree of freedom) and its formulation is based on ANDES (Assumed Natural DEviatoric Strain) template. A template is a general formulation which can produce a group of elements by assigning different values to some free parameters. A special set of values for these free parameters gives the optimal membrane element which is not sensitive to the aspect ratio. The interesting point about template formulation is that most of the elements which have already been published can be reproduced by assigning appropriate values to the free parameters. Felippa [27] also showed that another LST3/9 membrane element with drilling degree of freedom can be generated by retrofitting a “parent” element, in this case the LST6/12 element with 6 nodes and 2 translational degrees of freedom per node. This element is called LST3/9Ret or LST(Ret) membrane element. He also showed that behavior of the Allman membrane element may be improved when its strains are filtered to a linear variation by reduced integration rule [27]. This special case of the Allman element is called Allman(3M). Although OPT, LST(Ret) and Allman(3M) membrane elements have the same number of nodes and degrees of freedom (including the drilling degree of freedom), only the OPT membrane element shows the aspect-ratio-independent behavior. All of these elements are again applications of the ANDES template.

There are several triangular plate bending elements to select from and combine

with a membrane element. The BCIZ element [28] is one of the simplest Kirchhoff plate bending elements. It was developed by Bazeley and co-workers [28] and was called after the authors' initials. Batoz et al. [29] studied several triangular Kirchhoff plate bending elements and showed that Discrete Kirchhoff Triangle (DKT) [30] is the most reliable triangular element for the analysis of thin plates. Katili [31] developed a discrete Kirchhoff-Mindlin triangular plate bending element called DKMT which is capable to include the transverse shear effects. This element coincides with the DKT element in case that transverse shear effects are negligible, and does not suffer from shear locking problem in case of thin plates. As a result, it seems that both thin and thick laminated composite plates can be modeled with this element.

1.2.2 Geometrically nonlinear analysis

There are three different approaches that can be used for nonlinear analysis. In the Total Lagrangian (TL) approach, equations are formulated with respect to a fixed reference configuration which is usually the initial configuration. In Updated Lagrangian (UL) approach the reference configuration is the last converged solution. The Corotational (CR) approach is the most recent formulation developed for geometrically nonlinear structural analysis. In this method the finite element equations are referred to two systems: a fixed configuration and a corotated configuration. The main advantage of corotational formulation is its effectiveness for problems with large-rotations but small strains, since it uses the existing small-strain FEM elements during the analysis [32]. The corotational formulation has not yet penetrated major commercial FEM codes.

Important works related to the development of the Corotational approach are those by Wempner [33], Belytschko and Hsieh [34], Bergan and Horrigmoe [35], Argyris [36] (regarding the large rotations), Rankin and Brogan [37], Szwabowicz [38], Rankin and Nour-Omid [39] and Nour-Omid and Rankin [40] (regarding the projector matrix), Crisfield [41], Peng and Crisfield [42], Pacoste [43], and Battini and Pacoste [44, 45]. Felippa’s comprehensive paper on this approach [46] is also a valuable reference.

Among the first publications on the non-linear large deflection post-buckling behavior of unstiffened rectangular plates are the publications by Marguerre [47], Kromm and Marguerre [48] and Levy [49]. Paik [50] captures the non-linear large deflection response of un-stiffened plates by an incremental Galerkin method, an approach previously outlined by Ueda [51]. Paik also considers stiffened plate with stiffeners “smeared” on the main plate [52, 53]. In this case the stiffened plate is modelled as an orthotropic un-stiffened plate. Byklum [54-56] studied stringer-stiffened plates with large deflections. In those studies, stringers are not smeared on the plate but considered as structural elements.

The effect of imperfections on the limit load of the structures was first investigated by Koiter [57], and then by other researchers [58-67]. Ohsaki and Uetani [68] presented a numerical approach for sensitivity analysis of buckling loads corresponding to a minor imperfection, and applied it for optimization of imperfection sensitive structures [69]. Random nature of the initial imperfections attracted many investigators like Fraser and Budiansky [70], Roorda [71] and Amazigo [72], to apply probabilistic approaches in this field. Reliability of imperfection sensitive shells

was investigated by Cederbaum and Arbocz [73]. Godoy [74] studied the Interactive buckling of fiber-reinforcement thin-walled columns.

The problem of interaction of an Euler buckling with local plate buckling was studied by several researchers [75-77]. Tvergaard [78] presented a detailed analysis of stiffened plates under interactive buckling. Byskov and Hutchinson [79] used an asymptotic approach for the same problem. Interaction of local and overall buckling in stiffened panels and shells was studied by Koiter and Pignat Rao [80, 81].

Comparisons between studies on the ultimate strength for stiffened panels have been presented in [82-85]. Experimental investigation for stiffened panel collapse behavior can be found in [86-88]. An extensive contribution to the ultimate strength design for ship stiffened panels has been provided in [89-92]. Paik et al. [93] studied the local buckling of stiffener webs. The effect of combined axial compression and lateral loads has been studied by Hughes and Ma [94, 95] and Hu et al. [96]. Also closed form solutions, simple physical models and finite strip methods have been extensively used for design optimization of stiffened panels [97-102].

A variety of methods and programs are available for the analysis of stiffened panels, ranging from simple closed form solutions to complicated 3-D discretized solutions. The more complicated or detailed modeling usually employs discretized models such as finite element and boundary element analysis. To avoid the complexity, some researchers perform approximate analyzes, using simplifying assumptions based on the repeating stiffener pattern. The analysis costs typically increase with the level of details considered in the analysis, and the method of analysis (e.g., exact modeling the stiffeners instead of assuming them as smeared, or nonlinear analysis instead of

linear analysis).

1.2.3 Structural design optimization

Research works on shape optimization can be found in [103-111]. Computation of the sensitivities of limit points of non-linear structures can be found in [111-118]. There are also works dealing with bifurcation points, but some of them do not specifically address finite element applications [119, 120], while others are restricted to the semi-analytical approach [16, 17].

In most recent works reported in the literature, the optimization algorithms were mainly based on the optimality criterion technique because of its computational efficiency. For example the optimality criterion method has been employed to minimize the weight of the truss and beam structures under the stress and displacement constraints [121-124], stability constraint [106, 125] or frequency constraint [126]. There are different forms of optimality criteria available in the literature. Those with the most application are “Fully Stress (FS)” design, “Simultaneous Failure Mode (SFM)” design, “Uniform Strain Energy Density (USED)” design, and “Constant Internal Force Distribution (CIFD)” design [127]. Modern optimality criterion algorithms would involve the case of satisfying the multiple constraints (scaling) and Karush-Kuhn-Tucker (KKT) [128] condition (resizing) alternatively.

Gallagher [129] showed that FS design is inadequate for minimum weight design of structures. Prager and Taylor [130] showed that the optimum structure with uniform material properties and linear relation between the stiffness and volume, has uniform energy density distribution. A similar criterion was proposed by Venkayya and co-

workers [131, 132] for discretized structures which states that “the average strain energy density is the same for all elements of the optimum structure.” Venkayya [133] made a more general form for the optimality criteria stating that “the ratio of strain energy to strain energy capacity is constant for every member in the optimum structure.”

Berke [134] proposed an algorithm to satisfy the optimality criteria considering that if a criterion works for statically determinate structures, then it would converge in a few iterations for most indeterminate structures (in the same manner as FS criterion). Berke’s work was extended to multiple constraints by Gellatly and Berke [135, 136] who proposed the envelope method for multiple displacement constraint structures. Nagtegaal [137] directly used the displacement constraint equations to formulate an iteration scheme using the Lagrange multiplier. Berke and Khot [138] proposed an iteration scheme for large scale structures. Khot et al. [139] applied classical optimality criteria method for both stress and displacement constraints. For more detailed literature survey on optimality criteria methods, the reader is referred to a recent paper by Lógó [127].

Layout optimization problems for rib reinforcement were considered almost two decades ago by Bendsøe and Kikuchi [140]. An overview of the research in layout and topology optimization is given in the paper by Rozvany et al. [141]. Stok and Mihelic [142] presented a method to identify the rib location by performing thickness distribution. Chung and Lee [143] employed topology optimization technique to identify the size of the ribs for a pre-determined rib layout. Lee et al. [144] have used the modal design sensitivity analysis for topology optimization of an automobile hood.

Lam and Santhikumar [145] developed a method to find the optimum locations of the ribs subject to design constraints using thickness optimization with uniform strain energy density criterion. All of the above mentioned studies on the stiffened panels are based on the linear analysis, however as mentioned before, many plate and shell structures display nonlinear behavior under applied loads.

1.3 Objective and scope of present research

The objective of this thesis is to present an efficient, accurate and robust methodology for nonlinear finite element analysis and design optimization of thin-walled structures. Two new triangular thin and thick shell elements are developed and modified for laminated composite plates and shells. A finite element code based on the corotational approach combined with the Newton-Raphson technique is developed and used with optimality criteria to analyze and optimize geometrically nonlinear structures. The optimality criteria presented in this study are the new criteria, derived for problems with geometric nonlinearity considering the thickness or geometry design variables. The aim of the optimization is to maximize the critical load of the structure subject to constant total mass, or minimize the total mass subject to constant applied loads. Application of the thickness optimization in optimum design of stiffened panels, and a methodology to efficiently incorporate the effects of local buckling and mode switching in optimization of stiffened panels are also presented.

It should be mentioned that triangular facet shell element is used in this study due to its computational efficiency. This speeds up the optimization process especially for geometrically nonlinear structures, where a large number of analyzes is performed

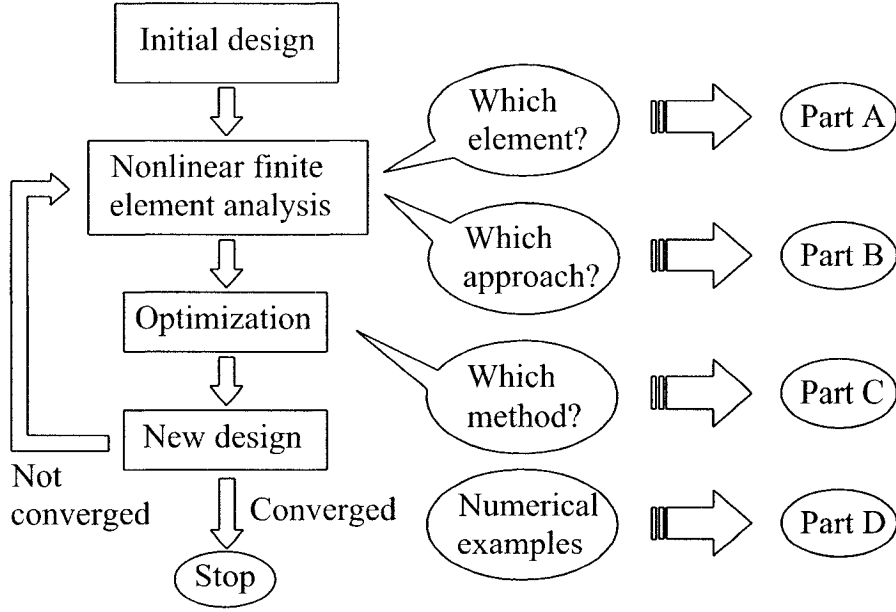


Figure 1.2: Different parts of the present work

before converging to the optimal design.

The present work consists mainly of the following four parts (Figure 1.2):

A) Developing new shell elements with drilling degree of freedom, and without aspect ratio sensitivity.

B) Programming a finite element analysis code for analysis of geometrically non-linear structures using corotational approach and new shell elements.

C) Developing optimality criteria for shape optimization of thin-walled structures.

D) Applying the new shell elements and optimality criteria for nonlinear analysis and design optimization of selected plate and shell structures.

In part **A** a new shell element is developed by combining the DKT plate bending element and the OPT membrane element. Also, a thick composite shell element is developed in a similar process by combining the DKMT plate bending element and the OPT membrane element. The membrane-bending coupling effect of the laminated

composite material is considered in the formulation. Shape functions of BCIZ and LST(Ret) elements with the same degrees of freedom as that of the DKT and OPT elements are used in order to formulate the inconsistent stress stiffness matrix and tangent stiffness matrix.

In part **B**, the shell elements derived in part **A** are used in a finite element analysis code based on corotational approach, to analyze plate and shell structures.

The objective of part **C** is to develop optimality criteria for design optimization of thin-walled structures undergoing large deflections. In this part a methodology is developed for shape optimization of plate and shell structures with geometric nonlinearity using finite element method. Optimality criteria are presented and combined with nonlinear finite element analysis to optimize thin-walled structures. Also a method is presented to find the optimum location of the ribs in stiffened panels, and to efficiently incorporate the effect of possible buckling modes as the initial imperfection.

In part **D**, first, the shell elements derived in part **A** are validated for nonlinear analysis of plate and shell structures. The results of nonlinear analyzes obtained using the proposed elements are compared with analytical solutions, those available in the literature, and with solutions obtained using LST(Ret) and Allman(3M) membrane elements in the formulation. Then, the optimality criteria presented in part **C** are used along with the nonlinear analysis program to perform shape optimization on plate and shell structures. Results are also compared with those obtained using the gradient-based Sequential Quadratic Programming (SQP) method of optimization.

1.4 Thesis organization

This thesis consists of six chapters. The present chapter (chapter 1) provided the background and motivation of this study. In this chapter, a systematic literature review on different aspects of the thesis with most important and relevant contributions to the field was presented.

In chapter 2 a new facet shell element is developed by combining the DKT plate bending element with the optimal triangular membrane element (OPT). Membrane-bending coupling effect for the case of laminated composite material is considered in the formulation. An extension of the new element for the analysis of moderately thick shells is also presented by combining the DKMT and OPT elements in a similar manner.

In chapter 3, different solution strategies for nonlinear equilibrium equations are presented. Computation of the critical points, and general aspects of the corotational approach for analysis of the geometrically nonlinear structures modeled by triangular shell elements are also explained.

In chapter 4, the general form of the shape optimization problem and its solution using the gradient-based optimization algorithm are explained. The alternative method of optimality criteria for two cases of load-capacity maximization under constant mass (along with its application on the design of stiffened panels), and mass minimization under constant load are presented. The shape optimization methodology is also modified to consider the effect of local buckling in stiffened panels.

Chapter 5 presents a large set of numerical examples on geometrically nonlinear static analysis and shape optimization of thin-walled structures. The results are com-

pared with those available analytically, those obtained using other elements, or those found using gradient-based optimization method. Finally, discussions, conclusions, future Work and publications are presented in chapter 6.

Chapter 2

Finite Element Formulation of the New Shell Element

2.1 Introduction

In this chapter a new shell element is developed by combining the DKT plate bending element and the optimal triangular membrane element (OPT). The membrane-bending coupling effect of the laminated composite material is considered in the formulation. Shape functions of BCIZ and LST(Ret) elements with the same degrees of freedom as that of the DKT and OPT elements are used in order to formulate the inconsistent stress stiffness matrix and tangent stiffness matrix. Finally, an extension of the new element for analysis of the moderately thick shells is presented by combining the DKMT and OPT elements in a similar manner.

2.2 Definition of geometric parameters

The geometry of the flat triangular shell element is shown in Figure 2.1. Thickness of the element is represented by t . Node numbering is counterclockwise and there are 6 degrees of freedom at each node (3 translations and 3 rotations). Local and

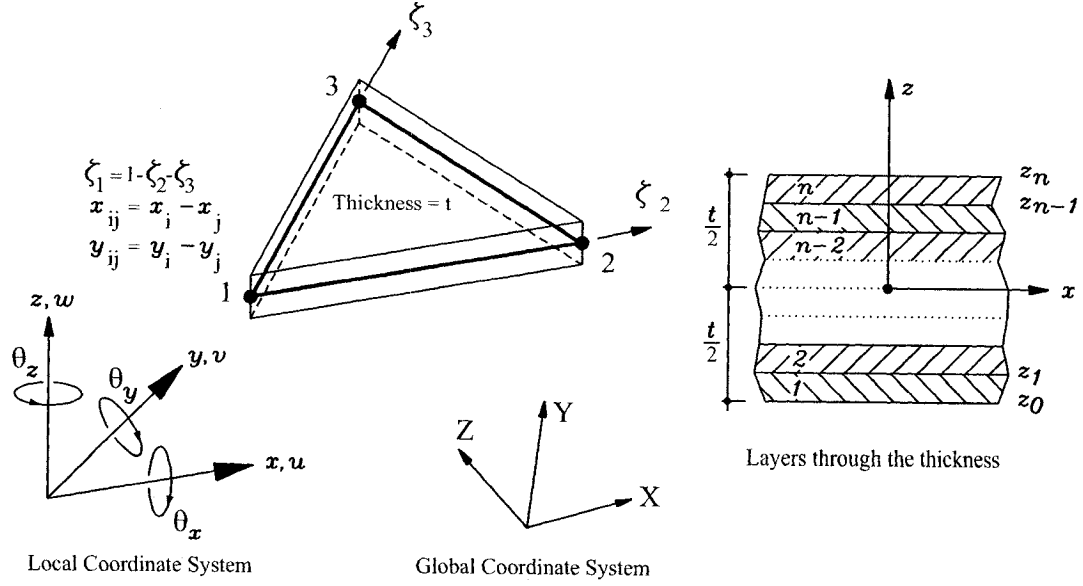


Figure 2.1: Geometry of the triangular element

global coordinate systems are xyz and XYZ , respectively. ζ_2 and ζ_3 are the area co-ordinates and $\zeta_1 = 1 - \zeta_2 - \zeta_3$. Coordinate differences are abbreviated as

$$x_{ij} = x_i - x_j, \quad y_{ij} = y_i - y_j \quad (2.1)$$

Area and volume of the element and the length of the side ij are represented by A , V and l_{ij} , respectively:

$$A = \frac{1}{2}(y_{21} x_{13} - x_{21} y_{13}), \quad V = A.t, \quad l_{ij} = \sqrt{x_{ij}^2 + y_{ij}^2} \quad (2.2)$$

2.3 Formulation of OPT membrane element

The degrees of freedom of OPT membrane element are collected in the nodal displacement vector as

$$\{d_m\} = \{u_1 \ v_1 \ \theta_{z1} \ u_2 \ v_2 \ \theta_{z2} \ u_3 \ v_3 \ \theta_{z3}\}^T \quad (2.3)$$

Formulation of the stiffness matrix of OPT membrane element is based on the following decomposition [27]

$$K_m = K_{basic} + K_{higher \ order} \quad (2.4)$$

where K_{basic} and $K_{higher \ order}$ are the basic and the higher order membrane stiffness components, respectively. The final form of K_m is a template with 11 free parameters:

$$K_m(\alpha_b, \beta_0, \dots, \beta_9) = \frac{1}{V} L E L^T + \int_V B^T E B dV \quad (2.5)$$

where E is the elasticity matrix in xyz system and is described as

$$E = \begin{bmatrix} E_{11} & E_{12} & E_{13} \\ E_{21} & E_{22} & E_{23} \\ E_{31} & E_{32} & E_{33} \end{bmatrix} \quad (2.6)$$

For an isotropic material with the Poisson's ratio ν and the Young's modulus E_o , the elasticity matrix can be written as

$$E = \frac{E_o}{1 - \nu^2} \begin{bmatrix} 1 & \nu & 0 \\ \nu & 1 & 0 \\ 0 & 0 & \frac{1-\nu}{2} \end{bmatrix} \quad (2.7)$$

Matrix B is defined as

$$B = T_e (Q_1 \ \zeta_1 + Q_2 \ \zeta_2 + Q_3 \ \zeta_3) \tilde{T}_{\theta u} \quad (2.8)$$

L , T_e , $\tilde{T}_{\theta u}$ and Q_{1-3} are constant matrices over the element and are defined as [27]

$$L = \frac{t}{2} \begin{bmatrix} y_{23} & 0 & x_{32} \\ 0 & x_{32} & y_{23} \\ \frac{1}{6}\alpha_b y_{23}(y_{13} - y_{21}) & \frac{1}{6}\alpha_b x_{32}(x_{31} - x_{12}) & \frac{1}{3}\alpha_b(x_{31}y_{13} - x_{12}y_{21}) \\ y_{31} & 0 & x_{13} \\ 0 & x_{13} & y_{31} \\ \frac{1}{6}\alpha_b y_{31}(y_{21} - y_{32}) & \frac{1}{6}\alpha_b x_{13}(x_{12} - x_{23}) & \frac{1}{3}\alpha_b(x_{12}y_{21} - x_{23}y_{32}) \\ y_{12} & 0 & x_{21} \\ 0 & x_{21} & y_{12} \\ \frac{1}{6}\alpha_b y_{12}(y_{32} - y_{13}) & \frac{1}{6}\alpha_b x_{21}(x_{23} - x_{31}) & \frac{1}{3}\alpha_b(x_{23}y_{32} - x_{31}y_{13}) \end{bmatrix} \quad (2.9)$$

$$T_e = \frac{1}{4A^2} \begin{bmatrix} y_{23}y_{13}l_{21}^2 & y_{31}y_{21}l_{32}^2 & y_{12}y_{32}l_{13}^2 \\ x_{23}x_{13}l_{21}^2 & x_{31}x_{21}l_{32}^2 & x_{12}x_{32}l_{13}^2 \\ (y_{23}x_{31} + x_{32}y_{13})l_{21}^2 & (y_{31}x_{12} + x_{13}y_{21})l_{32}^2 & (y_{12}x_{23} + x_{21}y_{32})l_{13}^2 \end{bmatrix} \quad (2.10)$$

$$\tilde{T}_{\theta u} = \frac{1}{4A} \begin{bmatrix} x_{32} & y_{32} & 4A & x_{13} & y_{13} & 0 & x_{21} & y_{21} & 0 \\ x_{32} & y_{32} & 0 & x_{13} & y_{13} & 4A & x_{21} & y_{21} & 0 \\ x_{32} & y_{32} & 0 & x_{13} & y_{13} & 0 & x_{21} & y_{21} & 4A \end{bmatrix} \quad (2.11)$$

$$Q_1 = \frac{2A}{3} \begin{bmatrix} \frac{\beta_1}{l_{13}^2} & \frac{\beta_2}{l_{13}^2} & \frac{\beta_3}{l_{13}^2} \\ \frac{\beta_4}{l_{13}^2} & \frac{\beta_5}{l_{13}^2} & \frac{\beta_6}{l_{13}^2} \\ \frac{\beta_7}{l_{13}^2} & \frac{\beta_8}{l_{13}^2} & \frac{\beta_9}{l_{13}^2} \end{bmatrix}, \quad Q_2 = \frac{2A}{3} \begin{bmatrix} \frac{\beta_9}{l_{13}^2} & \frac{\beta_7}{l_{13}^2} & \frac{\beta_8}{l_{13}^2} \\ \frac{\beta_{21}}{l_{13}^2} & \frac{\beta_{21}}{l_{13}^2} & \frac{\beta_{21}}{l_{13}^2} \\ \frac{\beta_3}{l_{13}^2} & \frac{\beta_1}{l_{13}^2} & \frac{\beta_2}{l_{13}^2} \\ \frac{\beta_6}{l_{13}^2} & \frac{\beta_4}{l_{13}^2} & \frac{\beta_5}{l_{13}^2} \end{bmatrix}, \quad Q_3 = \frac{2A}{3} \begin{bmatrix} \frac{\beta_5}{l_{13}^2} & \frac{\beta_6}{l_{13}^2} & \frac{\beta_4}{l_{13}^2} \\ \frac{\beta_{21}}{l_{13}^2} & \frac{\beta_{21}}{l_{13}^2} & \frac{\beta_{21}}{l_{13}^2} \\ \frac{\beta_8}{l_{13}^2} & \frac{\beta_9}{l_{13}^2} & \frac{\beta_7}{l_{13}^2} \\ \frac{\beta_{32}}{l_{13}^2} & \frac{\beta_{32}}{l_{13}^2} & \frac{\beta_{32}}{l_{13}^2} \\ \frac{\beta_2}{l_{13}^2} & \frac{\beta_3}{l_{13}^2} & \frac{\beta_1}{l_{13}^2} \end{bmatrix} \quad (2.12)$$

The exact integration of K_m is obtained using three numerical integration Gauss points (mid point rule). Final form of K_m may be written as [27]

$$K_m = \frac{1}{V} L E L^T + \frac{3}{4}\beta_0 \tilde{T}_{\theta u}^T K_{\theta} \tilde{T}_{\theta u} \quad (2.13)$$

where

$$K_{\theta} = At(Q_4^T E_{nat} Q_4 + Q_5^T E_{nat} Q_5 + Q_6^T E_{nat} Q_6) \quad (2.14)$$

and

$$E_{nat} = T_e^T E T_e, \quad Q_4 = \frac{1}{2}(Q_1 + Q_2), \quad Q_5 = \frac{1}{2}(Q_2 + Q_3), \quad Q_6 = \frac{1}{2}(Q_3 + Q_1) \quad (2.15)$$

α_b and β_1 through β_9 are free dimensionless parameters, and β_0 is an overall scaling coefficient.

It is possible to generate a group of elements by assigning different values to these free parameters. Among these, the two important cases are Allman(3M) and LST(Ret) membrane elements. Allman(3M) is a special case of Allman membrane element with its strains filtered to a linear variation by reduced integration rule in order to improve its behavior. It is an instance of the ANDES template by assigning the following values to the free parameters [27]:

$$\begin{aligned} \alpha_b = 1, \beta_0 = \frac{4}{9}, \beta_1 = \frac{1}{4}, \beta_2 = \frac{5}{4}, \beta_3 = \frac{3}{2}, \beta_4 = 0, \\ \beta_5 = -\beta_6 = 1, \beta_7 = -\frac{1}{4}, \beta_8 = -\frac{3}{2}, \beta_9 = -\frac{5}{4} \end{aligned} \quad (2.16)$$

Similarly assigning the following values to the free parameters leads to the LST(Ret) membrane element:

$$\begin{aligned} \alpha_b = \frac{4}{3}, \beta_0 = \frac{1}{2}, \beta_1 = -\beta_2 = \frac{2}{3}, \beta_3 = \beta_4 = 0, \\ \beta_5 = -\beta_6 = -\frac{4}{3}, \beta_7 = -\frac{2}{3}, \beta_8 = 0, \beta_9 = \frac{2}{3} \end{aligned} \quad (2.17)$$

Felippa [27] has shown that for an isotropic material with Poisson's ratio ν , the following values for the free parameters lead to the optimal membrane element. For this particular element, the strain energy for inplane bending computed by finite element method is exact for any aspect ratio:

$$\alpha_b = \frac{3}{2}, \beta_0 = \frac{1}{2}(1 - 4\nu^2), \beta_{1,3,5} = 1, \beta_2 = 2, \beta_4 = 0, \beta_{6,7,8} = -1, \beta_9 = -2 \quad (2.18)$$

For non-isotropic materials, all the values except β_0 remain the same. In this case only suboptimal performance can be expected, but it is guaranteed that the element does not lock as the aspect ratio increases or decreases. The following average value for β_0 has been proposed for non-isotropic materials [27]:

$$\beta_0 = \max\left(\frac{256\det(E)}{W} - 1.5, 0.01\right) \quad (2.19)$$

where W is presented as the following expression:

$$\begin{aligned} W = & -6E_{12}^3 + 5E_{11}^2E_{22} - 5E_{12}^2E_{22} - E_{22}(75E_{13}^2 + 14E_{13}E_{23} + 3E_{23}^2) + \\ & 2E_{12}(7E_{13}^2 + 46E_{13}E_{23} + 7E_{23}^2) - E_{11}(5E_{12}^2 + 3E_{13}^2 - 6E_{12}E_{22} - \\ & 5E_{22}^2 + 14E_{13}E_{23} + 75E_{23}^2) + (3E_{11}^2 + 82E_{11}E_{22} + 3E_{22}^2 - 4(6E_{12}^2 + \\ & 5E_{13}^2 - 6E_{13}E_{23} + 5E_{23}^2))E_{33} + 4(5E_{11} - 6E_{12} + 5E_{22})E_{33}^2 \end{aligned} \quad (2.20)$$

2.4 Formulation of the DKT plate bending element

The degrees of freedom of the DKT plate bending element are collected in the nodal displacement vector as

$$\{d_b\} = \{w_1 \ \theta_{x1} \ \theta_{y1} \ w_2 \ \theta_{x2} \ \theta_{y2} \ w_3 \ \theta_{x3} \ \theta_{y3} \ \}^T \quad (2.21)$$

The stiffness matrix of DKT element has been formulated by Batoz et al. [30] as

$$K_b = \int_A B_b^T D^e B_b dA = 2A \int_0^1 \int_0^{1-\zeta_3} B_b^T D^e B_b d\zeta_2 d\zeta_3 \quad (2.22)$$

where D^e is the flexural rigidity of the plate which in the case of an isotropic material with Poisson's ratio ν and Young's modulus E_o can be described as

$$D^e = \frac{E_o t^3}{12(1-\nu^2)} \begin{bmatrix} 1 & \nu & 0 \\ \nu & 1 & 0 \\ 0 & 0 & \frac{1-\nu}{2} \end{bmatrix} \quad (2.23)$$

and B_b is defined as

$$B_b = \frac{1}{2A} \begin{bmatrix} y_{31}H_1^T + y_{12}H_3^T & -x_{31}H_2^T - x_{12}H_4^T \\ -x_{31}H_1^T - x_{12}H_3^T + y_{31}H_2^T + y_{12}H_4^T \end{bmatrix} \quad (2.24)$$

where vectors H_1 through H_4 are functions of ζ_2 and ζ_3 and are written as [30]

$$\begin{aligned} H_1 &= \begin{bmatrix} P_6(1-2\zeta_2) + (P_5 - P_6)\zeta_3 \\ q_6(1-2\zeta_2) - (q_5 + q_6)\zeta_3 \\ -4 + 6(\zeta_2 + \zeta_3) + r_6(1-2\zeta_2) - \zeta_3(r_5 + r_6) \\ -P_6(1-2\zeta_2) + \zeta_3(P_4 + P_6) \\ q_6(1-2\zeta_2) - \zeta_3(q_6 - q_4) \\ -2 + 6\zeta_2 + r_6(1-2\zeta_2) + \zeta_3(r_4 - r_6) \\ -\zeta_3(P_5 + P_4) \\ \zeta_3(q_4 - q_5) \\ -\zeta_3(r_5 - r_4) \end{bmatrix} & H_2 = \begin{bmatrix} t_6(1-2\zeta_2) + (t_5 - t_6)\zeta_3 \\ 1 + r_6(1-2\zeta_2) - (r_5 + r_6)\zeta_3 \\ -q_6(1-2\zeta_2) + \zeta_3(q_5 + q_6) \\ -t_6(1-2\zeta_2) + \zeta_3(t_4 + t_6) \\ -1 + r_6(1-2\zeta_2) + \zeta_3(r_4 - r_6) \\ -q_6(1-2\zeta_2) - \zeta_3(q_4 - q_6) \\ -\zeta_3(t_5 + t_4) \\ \zeta_3(r_4 - r_5) \\ -\zeta_3(q_4 - q_5) \end{bmatrix} \\ \\ H_3 &= \begin{bmatrix} -P_5(1-2\zeta_3) - (P_6 - P_5)\zeta_2 \\ q_5(1-2\zeta_3) - (q_5 + q_6)\zeta_2 \\ -4 + 6(\zeta_2 + \zeta_3) + r_5(1-2\zeta_3) - \zeta_2(r_5 + r_6) \\ \zeta_2(P_4 + P_6) \\ \zeta_2(q_4 - q_6) \\ -\zeta_2(r_6 - r_4) \\ P_5(1-2\zeta_3) - \zeta_2(P_5 + P_4) \\ q_5(1-2\zeta_3) + \zeta_2(q_4 - q_5) \\ -2 + 6\zeta_3 + r_5(1-2\zeta_3) + \zeta_2(r_4 - r_5) \end{bmatrix} & H_4 = \begin{bmatrix} -t_5(1-2\zeta_3) - (t_6 - t_5)\zeta_2 \\ 1 + r_5(1-2\zeta_3) - (r_5 + r_6)\zeta_2 \\ -q_5(1-2\zeta_3) + \zeta_2(q_5 + q_6) \\ \zeta_2(t_4 + t_6) \\ \zeta_2(r_4 - r_6) \\ -\zeta_2(q_4 - q_6) \\ t_5(1-2\zeta_3) - \zeta_2(t_5 + t_4) \\ -1 + r_5(1-2\zeta_3) + \zeta_2(r_4 - r_5) \\ -q_5(1-2\zeta_3) - \zeta_2(q_4 - q_5) \end{bmatrix} \end{aligned} \quad (2.25)$$

where

$$\begin{aligned} P_k &= -6x_{ij}/l_{ij}^2 & q_k &= 3x_{ij}y_{ij}/l_{ij}^2 \\ t_k &= -6y_{ij}/l_{ij}^2 & r_k &= 3y_{ij}^2/l_{ij}^2 \end{aligned} \quad (2.26)$$

$$k = 4, 5, 6 \quad \text{for } ij = 23, 31, 12$$

Since the thickness and material properties are constant over the element, the exact integration of K_b is obtained using three Gauss points located at the mid-nodes.

2.5 Shell element formulation

The shell element formulated in this study is a triangular flat element with 18 degrees of freedom:

$$\{d\} = \{u_1 \ v_1 \ w_1 \ \theta x_1 \ \theta y_1 \ \theta z_1 \ u_2 \ v_2 \ w_2 \ \theta x_2 \ \theta y_2 \ \theta z_2 \ \dots \theta z_3\}^T \quad (2.27)$$

We rearrange this vector to separate membrane and bending degrees of freedom:

$$\begin{Bmatrix} \{d_m\} \\ \{d_b\} \end{Bmatrix} = \begin{Bmatrix} \{u_1 \ v_1 \ \theta z_1 \ u_2 \ v_2 \ \theta z_2 \ \dots \ \theta z_3\}^T \\ \{w_1 \ \theta x_1 \ \theta y_1 \ w_2 \ \theta x_2 \ \theta y_2 \ \dots \ \theta y_3\}^T \end{Bmatrix} \quad (2.28)$$

Strain-displacement relationship can be written as

$$\begin{Bmatrix} \{\varepsilon_m\} \\ \{\varepsilon_b\} \end{Bmatrix} = \begin{Bmatrix} [B_m]_{3 \times 9} & [0]_{3 \times 9} \\ [0]_{3 \times 9} & [B_b]_{3 \times 9} \end{Bmatrix} \cdot \begin{Bmatrix} \{d_m\} \\ \{d_b\} \end{Bmatrix} = [B_o] \cdot \begin{Bmatrix} \{d_m\} \\ \{d_b\} \end{Bmatrix} \quad (2.29)$$

The exact expression for the relationship between the strains and nodal displacements in the OPT membrane element is still unknown. In this study, the following expression is considered for B_m based on the formulation of membrane stiffness:

$$B_m = \frac{L^T}{V} + \frac{3}{2}\sqrt{\beta_0} \ T_e \ (Q_1 \ \zeta_1 + Q_2 \ \zeta_2 + Q_3 \ \zeta_3) \ \tilde{T}_{\theta u} \quad (2.30)$$

It can be easily shown that the integral $\int_V B_m^T E B_m dV$ equals to the stiffness matrix of OPT. It is important to note that the integral of the higher order strains over the element is zero. Such an element is called *energy orthogonal element*.

The force-strain relationship for a thin laminated plate based on the classical laminate theory is [146]

$$\begin{Bmatrix} N_x \\ N_y \\ N_{xy} \\ M_x \\ M_y \\ M_{xy} \end{Bmatrix} = \begin{bmatrix} A^e & B^e \\ B^e & D^e \end{bmatrix} \cdot \begin{Bmatrix} \varepsilon_x^\circ \\ \varepsilon_y^\circ \\ \gamma_{xy}^\circ \\ \kappa_x^\circ \\ \kappa_y^\circ \\ \kappa_{xy}^\circ \end{Bmatrix} = [D_\circ] \cdot \begin{Bmatrix} \{\varepsilon_m\} \\ \{\varepsilon_b\} \end{Bmatrix} \quad (2.31)$$

where $\{\varepsilon_m\}$ and $\{\varepsilon_b\}$ are the membrane and flexural strains in the mid-surface of the plate. $\{N_x \ N_y \ N_{xy}\}^T$ and $\{M_x \ M_y \ M_{xy}\}^T$ are force resultants and moment resultants, respectively. A^e , B^e and D^e are the stretching stiffness matrix, membrane-bending coupling stiffness matrix, and bending stiffness matrix, respectively [146]:

$$\begin{aligned} A_{ij}^e &= \sum_{k=1}^n (z_k - z_{k-1}) E_{ij}^k \\ B_{ij}^e &= \sum_{k=1}^n \frac{1}{2} (z_k^2 - z_{k-1}^2) E_{ij}^k \\ D_{ij}^e &= \sum_{k=1}^n \frac{1}{3} (z_k^3 - z_{k-1}^3) E_{ij}^k \end{aligned} \quad (2.32)$$

$k = 1, \dots, n \ (n = \text{number of layers})$

where E^k is the elasticity matrix in xyz system for the k^{th} layer, and z is measured from the midplane surface.

Stiffness matrix of the shell element corresponding to the displacement vector $\begin{Bmatrix} \{d_m\} \\ \{d_b\} \end{Bmatrix}$ can be described as

$$K = \int_A B_o^T D_o B_o dA = \begin{bmatrix} \int B_b^T B^e B_m dA & \int B_m^T B^e B_b dA \\ K_m & K_b \end{bmatrix} = \begin{bmatrix} K_m & K_{mb} \\ K_{bm} & K_b \end{bmatrix} \quad (2.33)$$

It is obvious that the stiffness matrix is symmetric since $K_{mb}^T = K_{bm}$. This stiffness matrix is rearranged corresponding to the nodal displacement vector $\{d\}$.

2.6 Extension to the thick shell element

The shell element derived in the previous section can be extended to the case of thick shells by switching the DKT bending element to DKMT (Discrete Kirchhoff–Mindlin Triangle [31]). The DKMT plate bending element has been formulated based on a generalization of the discrete Kirchhoff technique to include the transverse shear effects [31].

In the most general case, the force-strain relationship for a thick composite flat shell element is [146]

$$\begin{Bmatrix} N_x \\ N_y \\ N_{xy} \\ M_x \\ M_y \\ M_{xy} \\ Q_y \\ Q_x \end{Bmatrix} = \begin{bmatrix} A^e & B^e & [0]_{3 \times 2} \\ B^e & D^e & [0]_{3 \times 2} \\ [0]_{2 \times 3} & [0]_{2 \times 3} & F^e \end{bmatrix} \cdot \begin{Bmatrix} \varepsilon_x^\circ \\ \varepsilon_y^\circ \\ \gamma_{xy}^\circ \\ \kappa_x^\circ \\ \kappa_y^\circ \\ \kappa_{xy}^\circ \\ \bar{\gamma}_{yz} \\ \bar{\gamma}_{xz} \end{Bmatrix} \quad (2.34)$$

or

$$\begin{Bmatrix} \{N\} \\ \{M\} \\ \{Q\} \end{Bmatrix} = [D_o]_{8 \times 8} \cdot \begin{Bmatrix} \{\varepsilon_m\} \\ \{\varepsilon_b\} \\ \{\bar{\gamma}\} \end{Bmatrix} \quad (2.35)$$

where $\{\varepsilon_m\}$ and $\{\varepsilon_b\}$ are the membrane and flexural strains at the mid-surface of the plate, respectively, and $\{\bar{\gamma}\}$ is the transverse shear strains. $\{N\}$, $\{M\}$ and

$\{Q\}$ are in-plane force resultants, moment resultants, and transverse shear resultants, respectively. A^e , B^e , and D^e are the same parameters defined in Equation (2.32) in terms of E_{ij}^k , and F^e is the shear stiffness matrix defined as [146]:

$$F_{ij} = \sum_{k=1}^n (5/6)(z_k - z_{k-1}) C_{ij}^k \quad (2.36)$$

$k = 1, \dots, n \quad (n = \text{number of layers})$

where the coefficient (5/6) is the shear correction factor, and z is measured from the midplane surface. E_{ij}^k and C_{ij}^k are the components of the plane stress reduced stiffness and 3D stiffness matrices in xyz system for the k^{th} layer:

$$\begin{Bmatrix} \sigma_x \\ \sigma_y \\ \tau_{xy} \\ \tau_{yz} \\ \tau_{xz} \end{Bmatrix} = \begin{bmatrix} [E^k]_{3 \times 3} & [0]_{3 \times 2} \\ [0]_{2 \times 3} & [C^k]_{2 \times 2} \end{bmatrix} \cdot \begin{Bmatrix} \{\varepsilon_m\} + z_k \cdot \{\varepsilon_b\} \\ \{\bar{\gamma}\} \end{Bmatrix} \quad (2.37)$$

Strain-nodal displacement relation may be written as

$$\begin{Bmatrix} \{\varepsilon_m\} \\ \{\varepsilon_b\} \\ \{\bar{\gamma}\} \end{Bmatrix} = \begin{bmatrix} B_m & [0]_{3 \times 9} \\ [0]_{3 \times 9} & B_b^\circ \\ [0]_{2 \times 9} & B_s^\circ \end{bmatrix} \cdot \begin{Bmatrix} \{d_m\} \\ \{d_b\} \end{Bmatrix} = [B_o] \cdot \begin{Bmatrix} \{d_m\} \\ \{d_b\} \end{Bmatrix} \quad (2.38)$$

where B_b° and B_s° are the strain-nodal displacement matrices for bending and shear modes of deformation in DKMT element, respectively [31].

Finally, the stiffness matrix of the thick shell element corresponding to the displacement vector $\begin{Bmatrix} \{d_m\} \\ \{d_b\} \end{Bmatrix}$ can be described as

$$K = \int_A B_o^T \cdot D_o \cdot B_o \cdot dA = \begin{bmatrix} \int B_m^T \cdot A^e \cdot B_m \, dA & \int B_m^T \cdot B^e \cdot B_b^\circ \, dA \\ \int B_b^{\circ T} \cdot B^e \cdot B_m \, dA & \int (B_b^{\circ T} \cdot D^e \cdot B_b^\circ + B_s^{\circ T} \cdot F^e \cdot B_s^\circ) \, dA \end{bmatrix} \quad (2.39)$$

$$= \begin{bmatrix} K_m & K_{mb}^\circ \\ K_{bm}^\circ & K_b^\circ \end{bmatrix} \quad (2.40)$$

where K_m and K_b° are the stiffness matrixes of OPT membrane and DKMT plate bending elements respectively [27, 31], and K_{mb}° and K_{bm}° are the membrane-bending coupling stiffness. Similar to the case of the thin element, the integrals in the stiffness matrix can be evaluated exactly using three Gauss points.

2.7 Stress stiffness formulation

In order to have the tangent stiffness, it is necessary to add the stress stiffness $[K_\sigma]$ (also called as geometric stiffness) to the linear conventional stiffness matrix. An expression for the stress stiffness is obtained by considering the work done by the membrane forces N_x, N_y and N_{xy} as they act through displacements associated with small lateral and in-plane deflections [147]. We start by the Green-Lagrange membrane strains associated with the deflections u, v and w :

$$\begin{Bmatrix} \varepsilon_x \\ \varepsilon_y \\ \gamma_{xy} \end{Bmatrix} = \begin{Bmatrix} u'_x + \frac{1}{2}(w'^2_x + u'^2_x + v'^2_x) \\ v'_y + \frac{1}{2}(w'^2_y + u'^2_y + v'^2_y) \\ u'_y + v'_x + (u'_x \cdot u'_y + v'_x \cdot v'_y + w'_x \cdot w'_y) \end{Bmatrix} \quad (2.41)$$

where “ $'$ ” and “ $'$ ” denote the derivatives with respect to x any y , respectively. The initial terms in this equation are the customary engineering definitions of strains, and the added terms in parentheses are the nonlinear strains arise from higher-order terms. Work is done, and strain energy e is stored, as constant membrane forces act through these strains:

$$e = \int \int \begin{Bmatrix} \varepsilon_x \\ \varepsilon_y \\ \gamma_{xy} \end{Bmatrix}^T \begin{Bmatrix} N_x \\ N_y \\ N_{xy} \end{Bmatrix} dx dy = e_L + e_\sigma \quad (2.42)$$

e_L is the work done by the membrane forces acting through displacements associated with the engineering strains $u'_x, v'_y, u'_y + v'_x$. This part of work leads to nodal

loads associated with N_x, N_y, N_{xy} . The second part of the work, e_σ , is related to stress stiffness $[K_\sigma]$, which is the work done by the membrane forces acting through displacements associated with higher-order contributions to strains:

$$e_\sigma = \frac{1}{2} \int \int \left\{ \begin{matrix} u'_x \\ u'_y \\ v'_x \\ v'_y \\ w'_x \\ w'_y \end{matrix} \right\}^T \begin{bmatrix} [\tilde{N}] & [0]_{2 \times 2} & [0]_{2 \times 2} \\ [0]_{2 \times 2} & [\tilde{N}] & [0]_{2 \times 2} \\ [0]_{2 \times 2} & [0]_{2 \times 2} & [\tilde{N}] \end{bmatrix} \left\{ \begin{matrix} u'_x \\ u'_y \\ v'_x \\ v'_y \\ w'_x \\ w'_y \end{matrix} \right\} dx dy \quad (2.43)$$

where $[\tilde{N}]$ is $\begin{bmatrix} N_x & N_{xy} \\ N_{xy} & N_y \end{bmatrix}$.

If the element is isoparametric, shape functions are expressed in terms of natural coordinates ζ_1 , ζ_2 and ζ_3 . In this case we invoke the Jacobian matrix $[J]$:

$$\left\{ \begin{matrix} u'_x \\ u'_y \\ v'_x \\ v'_y \\ w'_x \\ w'_y \end{matrix} \right\} = \begin{bmatrix} [J]^{-1} & [0]_{2 \times 2} & [0]_{2 \times 2} \\ [0]_{2 \times 2} & [J]^{-1} & [0]_{2 \times 2} \\ [0]_{2 \times 2} & [0]_{2 \times 2} & [J]^{-1} \end{bmatrix} \cdot \left\{ \begin{matrix} u'_{\zeta_2} \\ u'_{\zeta_3} \\ v'_{\zeta_2} \\ v'_{\zeta_3} \\ w'_{\zeta_2} \\ w'_{\zeta_3} \end{matrix} \right\} = [J_t]_{6 \times 6} [G]_{6 \times 18} \left\{ \begin{matrix} \{d_m\} \\ \{d_b\} \end{matrix} \right\} \quad (2.44)$$

where $[J] = \begin{bmatrix} x'_{\zeta_2} & y'_{\zeta_2} \\ x'_{\zeta_3} & y'_{\zeta_3} \end{bmatrix}$, and $[J_t] = \begin{bmatrix} [J]^{-1} & [0]_{2 \times 2} & [0]_{2 \times 2} \\ [0]_{2 \times 2} & [J]^{-1} & [0]_{2 \times 2} \\ [0]_{2 \times 2} & [0]_{2 \times 2} & [J]^{-1} \end{bmatrix}$. Components of $[G]$ are derivatives of shape functions with respect to ζ_2 and ζ_3 :

$$[G] = \begin{bmatrix} N_1^u)'_{\zeta_2} & N_2^u)'_{\zeta_2} & \cdots & N_9^u)'_{\zeta_2} & 0 & 0 & \cdots & 0 \\ N_1^u)'_{\zeta_3} & N_2^u)'_{\zeta_3} & \cdots & N_9^u)'_{\zeta_3} & 0 & 0 & \cdots & 0 \\ N_1^v)'_{\zeta_2} & N_2^v)'_{\zeta_2} & \cdots & N_9^v)'_{\zeta_2} & 0 & 0 & \cdots & 0 \\ N_1^v)'_{\zeta_3} & N_2^v)'_{\zeta_3} & \cdots & N_9^v)'_{\zeta_3} & 0 & 0 & \cdots & 0 \\ 0 & 0 & \cdots & 0 & N_1^w)'_{\zeta_2} & N_2^w)'_{\zeta_2} & \cdots & N_9^w)'_{\zeta_2} \\ 0 & 0 & \cdots & 0 & N_1^w)'_{\zeta_3} & N_2^w)'_{\zeta_3} & \cdots & N_9^w)'_{\zeta_3} \end{bmatrix} \quad (2.45)$$

where $u = \sum_{i=1}^9 N_i^u \{d_m\}$, $v = \sum_{i=1}^9 N_i^v \{d_m\}$, $w = \sum_{i=1}^9 N_i^w \{d_b\}$.

Formulation of OPT membrane and DKT (and also DKMT) plate bending elements are based on the assumptions on strains. Therefore the internal displacements

u , v , and w are not known. One solution is using the shape functions of other elements with the same degrees of freedom. BCIZ is a plate bending element with the same nodes and degrees of freedom as the DKT and DKMT elements. Its shape functions were originally developed for the quadratic strain triangle [148] but then used for the plate bending formulation :

$$w = \left\{ \begin{array}{c} \zeta_1^2(3 - 2\zeta_1) + 2\zeta_1\zeta_2\zeta_3 \\ -\zeta_1^2(y_{12}\zeta_2 + y_{13}\zeta_3) - 0.5(y_{12} + y_{13})\zeta_1\zeta_2\zeta_3 \\ \zeta_1^2(x_{12}\zeta_2 + x_{13}\zeta_3) + 0.5(x_{12} + x_{13})\zeta_1\zeta_2\zeta_3 \\ \zeta_2^2(3 - 2\zeta_2) + 2\zeta_1\zeta_2\zeta_3 \\ -\zeta_2^2(y_{23}\zeta_3 + y_{21}\zeta_1) - 0.5(y_{23} + y_{21})\zeta_1\zeta_2\zeta_3 \\ \zeta_2^2(x_{23}\zeta_3 + x_{21}\zeta_1) + 0.5(x_{23} + x_{21})\zeta_1\zeta_2\zeta_3 \\ \zeta_3^2(3 - 2\zeta_3) + 2\zeta_1\zeta_2\zeta_3 \\ -\zeta_3^2(y_{31}\zeta_1 + y_{32}\zeta_2) - 0.5(y_{31} + y_{32})\zeta_1\zeta_2\zeta_3 \\ \zeta_3^2(x_{31}\zeta_1 + x_{32}\zeta_2) + 0.5(x_{31} + x_{32})\zeta_1\zeta_2\zeta_3 \end{array} \right\}^T \cdot \{d_b\} \quad (2.46)$$

Similarly the shape functions of LST(Ret) [27] with the same nodes and degrees of freedom as the OPT membrane element are considered to relate deflections u , v and w to the nodal membrane deflections as

$$\left\{ \begin{array}{c} u \\ v \end{array} \right\} = \left[\begin{array}{cccccc} \zeta_1 & 0 & \frac{\alpha_b\zeta_1}{2}(y_{12}\zeta_2 - y_{31}\zeta_3) & \cdots & \zeta_3 & 0 \\ 0 & \zeta_1 & \frac{\alpha_b\zeta_1}{2}(x_{21}\zeta_2 - x_{13}\zeta_3) & \cdots & 0 & \zeta_3 \end{array} \right] \cdot \{d_m\} \quad (2.47)$$

The final expression for stress stiffness matrix $[K_\sigma]$ corresponding to the nodal displacement vector $\left\{ \begin{array}{c} \{d_m\} \\ \{d_b\} \end{array} \right\}$ is

$$[K_\sigma] = 2A \int_0^1 \int_0^{1-\zeta_3} [G]^T [J_t]^T \left[\begin{array}{ccc} [\tilde{N}] & [0]_{2 \times 2} & [0]_{2 \times 2} \\ [0]_{2 \times 2} & [\tilde{N}] & [0]_{2 \times 2} \\ [0]_{2 \times 2} & [0]_{2 \times 2} & [\tilde{N}] \end{array} \right] [J_t][G] d\zeta_2 d\zeta_3 \quad (2.48)$$

This integral can be evaluated exactly using seven Gauss points in the area coordinate system [147]. $[K_\sigma]$ is then rearranged corresponding to the nodal displacement

vector $\{d\}$.

Using the stress stiffness, linear buckling analysis is performed by solving the following eigenvalue problem:

$$\det([K] + \lambda[K_\sigma]) = 0 \quad (2.49)$$

where the smallest eigenvalue λ defines the smallest level for which the buckling happens:

$$\{Load\}_{cr} = \lambda\{Load\}_{ref} \quad (2.50)$$

Membrane forces used in computing the stress stiffness are found from the resultant strains of linear analysis under reference load.

In the case of nonlinear analysis, an iterative method such as Newton–Raphson scheme, along with the tangent stiffness matrix is used to find the load–displacement equilibrium path. This will be explained in the next chapter.

Chapter 3

Solutions of Nonlinear Finite Element Equations

3.1 Introduction

For nonlinear problems, the stiffness of the structure, the applied loads, and/or boundary conditions can be affected by the induced displacements. As a result, the equilibrium of the structure must be established in the current configuration (which is unknown). At each equilibrium state along the equilibrium path, the resulting set of simultaneous equations are nonlinear. Therefore, a direct solution will not be possible and an iterative method is required. Several strategies have been devised to perform nonlinear analysis. As opposed to linear problems, it is extremely difficult, if not impossible, to implement one single strategy of general validity for all problems. Very often, the particular problem at hand will force the analyst to try different solution procedures to succeed in obtaining the correct solution. For example, “Snap-through” buckling problems of frames and shells (Figure 3.1) require deformation-controlled loading strategies such as “Displacement” and “Arc-length” based controls rather than force-controlled loading.

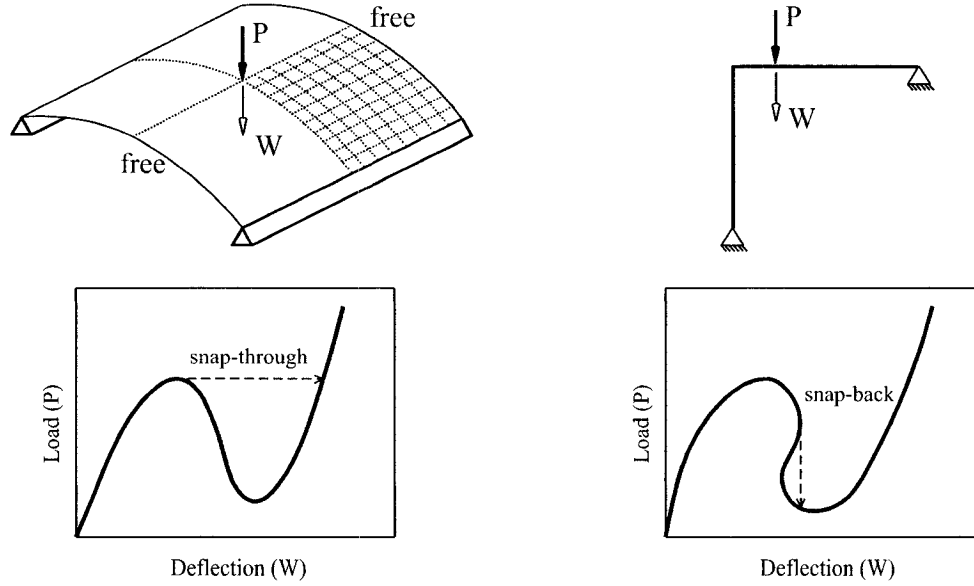


Figure 3.1: Snap-through and snap-back behaviors.

In this chapter, different solution strategies for nonlinear equilibrium equations are presented. Also, computation of the critical points, and general aspects of the corotational approach for analysis of the geometrically nonlinear structures modeled by triangular shell elements are explained.

3.2 Concept of “time” in static analysis

For nonlinear static analysis, the loads are applied in incremental steps through the use of “time”. The “time” value represents a pseudo-variable which denotes the intensity of the applied loads at a certain step. While, for nonlinear dynamic analysis and nonlinear static analysis with time-dependent material properties (e.g., creep), “time” represents the real time associated with the load application. The choice of “time” step size depends on several factors such as the level of nonlinearities of the problems and the solution procedure.

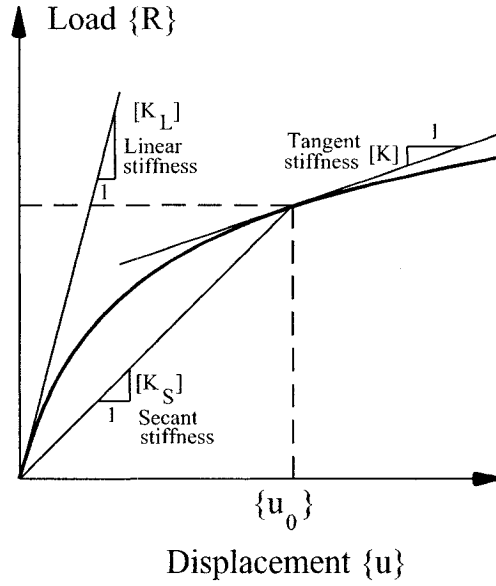


Figure 3.2: Tangent and secant stiffness matrices.

3.3 Tangent and secant stiffness

In nonlinear finite element analysis, the linear stiffness equation $[K]\{u\} = \{R\}$ with stiffness matrix $[K]$, nodal displacement vector $\{u\}$ and vector of applied load $\{R\}$, changes to $[K(u)]\{u\} = \{R\}$. Stiffness matrix $[K(u)]$ is a function of $\{u\}$ and is called the “Secant stiffness matrix” and is shown as $[K_S]$.

Slope of the tangent to the load-displacement curve at any point is called the “tangent stiffness matrix” shown as $[K]$:

$$[K] = \frac{\partial R}{\partial u} = \frac{\partial([K_S]\{u\})}{\partial u} \Rightarrow [K]_{ij} = \frac{\partial R_i}{\partial u_j} = [K_S]_{ij} + \sum_{k=1}^n \frac{\partial (K_S)_{ik}}{\partial u_j} u_k \quad (3.1)$$

Figure 3.2 shows the secant and the tangent stiffness matrices at $\{u\} = \{u_0\}$.

3.4 Static analysis

There are different numerical procedures that can be incorporated in the solution of nonlinear problems using the finite element method. A successful procedure must

include the following:

- An iterative method to satisfy the nonlinear equations governing the equilibrium state along the path.
- A control technique capable of controlling the progress of the computations along the equilibrium path of the system.
- Termination schemes to end the solution process.

In the following sections, these concepts are explained in more details.

3.5 Iterative methods for solving nonlinear equations

In nonlinear static analysis, the basic set of equations to be solved at any time step $t + \Delta t$, is

$$R^{(t+\Delta t)} - F^{(t+\Delta t)} = 0 \quad (3.2)$$

where

$R^{(t+\Delta t)}$ = Vector of externally applied nodal loads.

$F^{(t+\Delta t)}$ = Vector of internally generated nodal forces.

Since the internal nodal forces $F^{(t+\Delta t)}$ depend on nodal displacements $u^{(t+\Delta t)}$ at time $t + \Delta t$, an iterative method must be used. The following equations represent the basic outline of an iterative scheme to solve the equilibrium equations at a certain time step $t + \Delta t$:

$$\Delta R_{(i-1)} = R^{(t+\Delta t)} - F_{(i-1)}^{(t+\Delta t)} \quad (3.3)$$

$$K_{(i-1)}^{(t+\Delta t)} \Delta u_{(i)} = \Delta R_{(i-1)} \quad (3.4)$$

$$u_{(i)}^{(t+\Delta t)} = u_{(i-1)}^{(t+\Delta t)} + \Delta u_{(i)} \quad (3.5)$$

$$u_{(0)}^{(t+\Delta t)} = u^{(t)}; \quad F_{(0)}^{(t+\Delta t)} = F^{(t)} \quad (3.6)$$

where

$R^{(t+\Delta t)}$ = Vector of externally applied nodal loads. This vector shows the current load level and is constant during the iterations converging to this load level.

$F_{(i-1)}^{(t+\Delta t)}$ = Vector of internally generated nodal forces at the beginning of iteration (i).

$\Delta R_{(i-1)}$ = The out-of-balance load vector at the beginning of iteration (i).

$\Delta u_{(i)}$ = Vector of incremental nodal displacements during iteration (i).

$u_{(i)}^{(t+\Delta t)}$ = Vector of total displacements after iteration (i).

$K_{(i-1)}^{(t+\Delta t)}$ = Tangent stiffness matrix at the beginning of iteration (i).

There exists different schemes to perform the above iteration. In the following, a brief description of some methods of the Newton type will be furnished.

3.5.1 Direct iteration

In the direct iteration method, the nonlinear equilibrium equation is solved using the secant stiffness matrix (Figure 3.3). Starting from a previously converged point $(R^{(t)}, u^{(t)})$, the new displacement is found using the initial tangent stiffness. Then, the secant stiffness is updated, and the new displacement is found using the new secant stiffness. This is continued until convergence under loading $R^{(t+\Delta t)}$ is achieved. Then, loading is increased to the next level and iteration begun again.

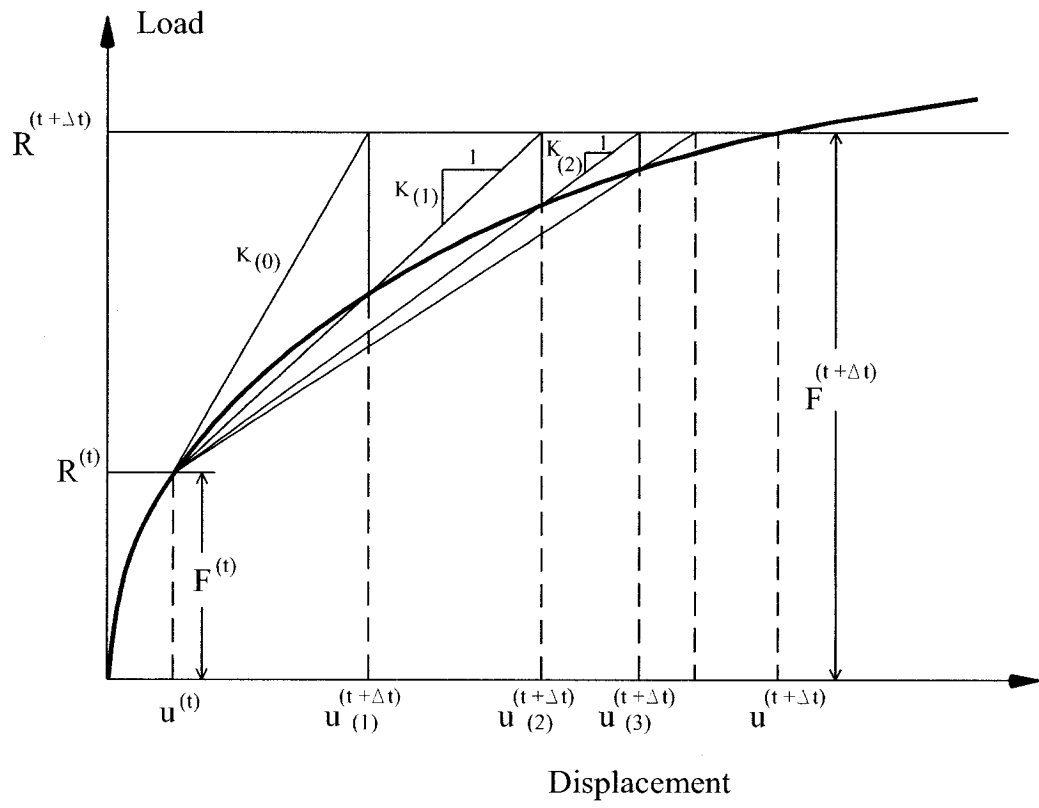


Figure 3.3: Direct iteration method.



3.5.2 Newton-Raphson (NR) scheme

In this scheme, the tangential stiffness matrix is formed at each iteration within a particular load step (Figure 3.4). The NR method has a high convergence rate and its rate of convergence is quadratic for relatively smooth non-linear response. However, since the tangent stiffness matrix should be computed at each iteration, this method can be expensive for large systems. In such cases it may be advantageous to use another iterative method.

The Newton-Raphson (NR) method is based on the following equation resulted from Equations (3.3) and (3.4):

$$K_{(i-1)}^{(t+\Delta t)} \Delta u_{(i)} = R^{(t+\Delta t)} - F_{(i-1)}^{(t+\Delta t)} \quad (3.7)$$

and the displacement increment $\Delta u_{(i)}$ is used to obtain the next displacement approximation using Equation (3.5). The iteration is continued until the out-of-balance load vector $\Delta R_{(i-1)}$ or the displacement increment $\Delta u_{(i)}$ are sufficiently small. A complete explanation for the convergence criteria will be later presented in this chapter.

3.5.3 Modified Newton-Raphson (MNR) scheme

In this scheme, the tangential stiffness matrix is formed at the beginning of each load step and used throughout the iterations (Figure 3.5). This method is not computationally as expensive as the Newton-Raphson method, but it needs usually more number of iterations to converge.

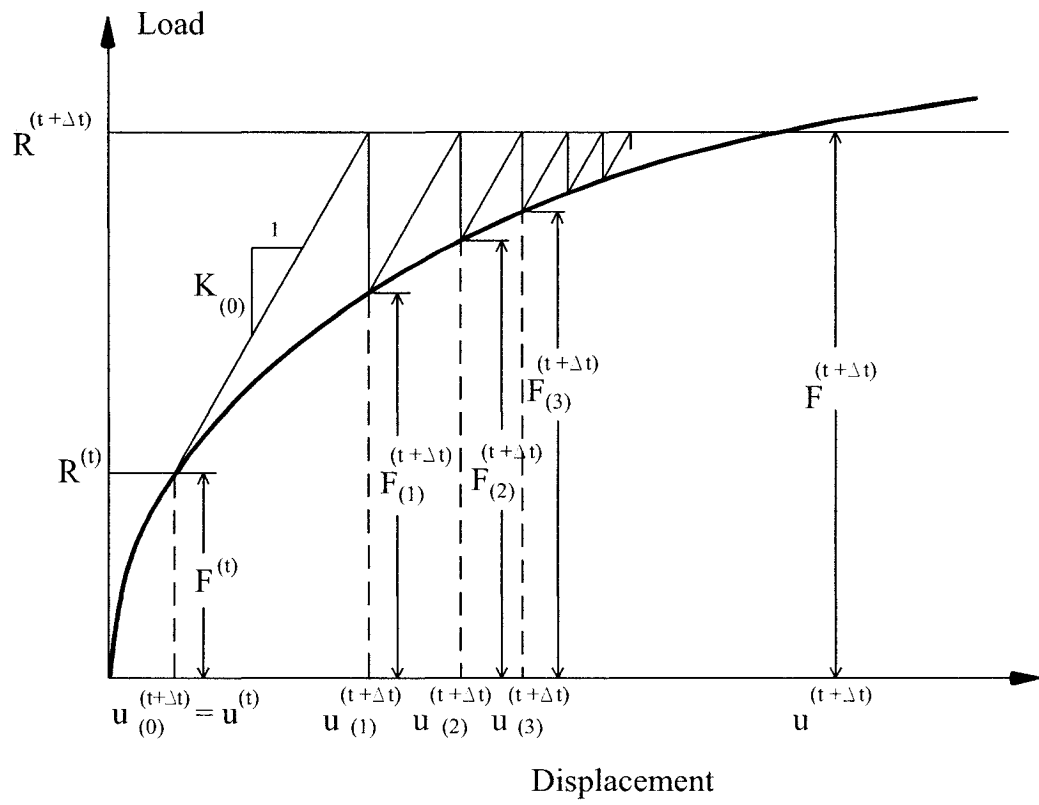


Figure 3.5: Modified Newton-Raphson iterative method.

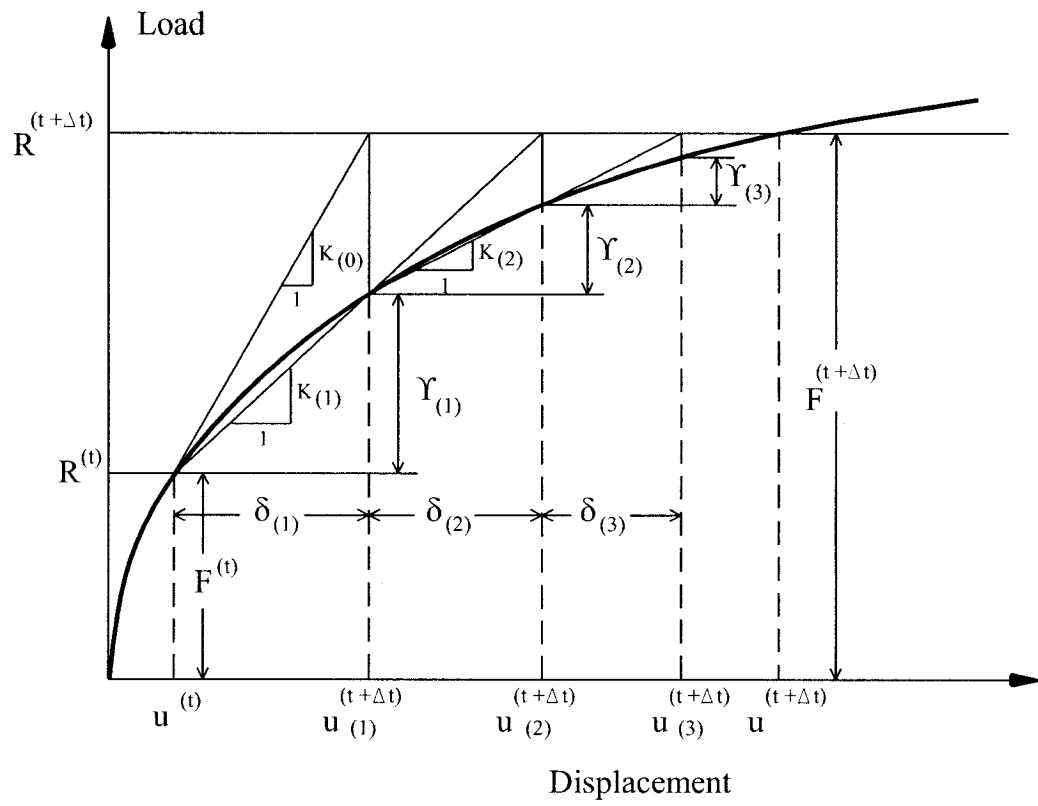


Figure 3.6: Quasi-Newton iterative method.

3.5.4 Quasi-Newton (QN) scheme

Unlike the NR and MNR iterative schemes, the QN family of schemes employs a lower-rank matrix to update the stiffness matrix (or its inverse) and to provide secant approximation from iteration $(i - 1)$ to iteration (i) (Figure 3.6). Defining a displacement increment as

$$\delta_{(i)} = u_{(i)}^{(t+\Delta t)} - u_{(i-1)}^{(t+\Delta t)} \quad (3.8)$$

and an increment in the out-of-balance loads;

$$\gamma_{(i)} = \Delta R_{(i-1)} - \Delta R_{(i)} \quad (3.9)$$

the updated iterative matrix should satisfy the QN equation:

$$K_{(i)}^{(t+\Delta t)} \delta_{(i)} = \gamma_{(i)} \quad (3.10)$$

Among the quasi-Newton methods available, the BFGS (Broyden-Fletcher-Goldfarb-Shanno) method appears to be most effective. For further explanation the reader is referred to Ref. [22].

3.6 Incremental control techniques

Different control techniques have been developed in existing works to perform non-linear analysis. These techniques can be classified as: force control, displacement control, and arc-length control (see Figure 3.7).

3.6.1 Force control

In this technique the applied load in each step is held constant (as in proportion to the total applied load). The load level is then increased to the next level after

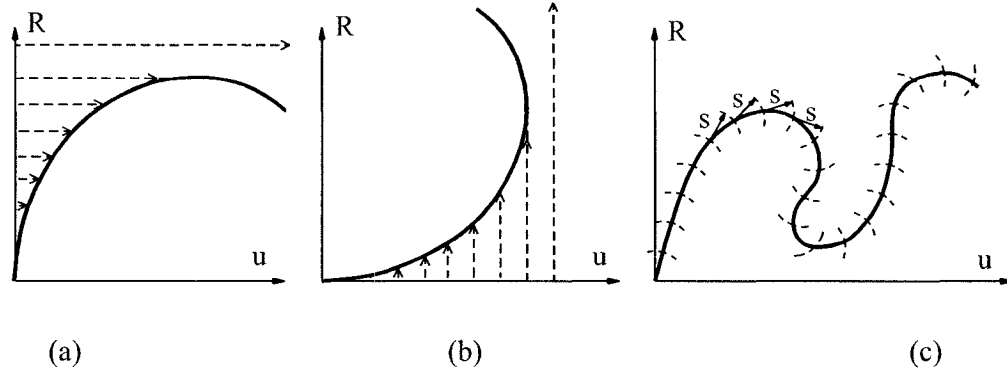


Figure 3.7: Incremental control techniques: force control (a), displacement control (b), and arc-length control (c).

convergence is achieved.

The force control technique can trace the load-displacement curve before the occurrence of a limit point (see Figure 3.7a). In such cases, to trace the complete load-displacement curve, it is necessary to use other path following techniques such as the displacement control, or arc-length control techniques.

3.6.2 Displacement control

In this technique, one of the displacement degrees of freedom is considered as the control parameter. This control parameter is then incrementally changed, and by each change, the corresponding load level multiplier λ and the point of the load-displacement path is found by an iterative method. This method is capable to handle problems with snap-through (for example a shallow shell under downward load), but again fails in snap-back problems (Figure 3.7b). Further explanation can be found in Ref.s [149, 150].

3.6.3 Arc-length control

The major difference between force control and arc-length control is that in the case of force control the applied load in any given step is held constant, whereas in the case of arc-length control the applied load is allowed to vary in any given step. In other words, the load factor λ does not remain constant in a step in the case of arc-length control. Let a known equilibrium configuration exist at some instant t , the total load λq applied to arrive at this configuration be $R^{(t)}$ and $u^{(t)}$ be the solution at this instant (Figure 3.8). Let $\Delta\lambda_0$ be a constant incremental load parameter. The solution for the first incremental step is obtained from $K_{(0)}^{(t+\Delta t)} \cdot \Delta u_{(1)} = \Delta\lambda_0 q$. In the subsequent iterations the correction to the solution is obtained from

$$\Delta u_{(i)} = \left(K_{(i-1)}^{(t+\Delta t)} \right)^{-1} \underbrace{\left(R_{(i-1)}^{(t+\Delta t)} - F_{(i-1)}^{(t+\Delta t)} \right)}_{\Delta R_{(i-1)}} + \delta\lambda_{(i)} \cdot q = \delta\bar{u} + \delta\lambda_{(i)} \delta u_t \quad (3.11)$$

Since the change in the load factor, $\delta\lambda_{(i)}$, is an unknown, an equation in addition to the equilibrium equations is required to determine the change in the load factor in each step. This is achieved by imposing a constraint

$$(\delta u_{(i)}^T \cdot \delta u_{(i)}) = \Delta l^2 \quad (3.12)$$

where $\delta u_{(i)} = \Delta u_{(i)} + \delta u_{(i-1)}$ is the total change of u at the end of the current iteration, and $\delta u_{(1)} = \Delta u_{(1)}$ and Δl is called the arc-length.

The arc length Δl is determined in the first step as:

$$\Delta l = \sqrt{\delta u_{(1)}^T \cdot \delta u_{(1)}} \quad (3.13)$$

where

$$\delta u_{(1)} = \Delta u_{(1)} = \left(K_{(0)}^{(t+\Delta t)} \right)^{-1} \cdot (\Delta\lambda_0 q) \quad (3.14)$$

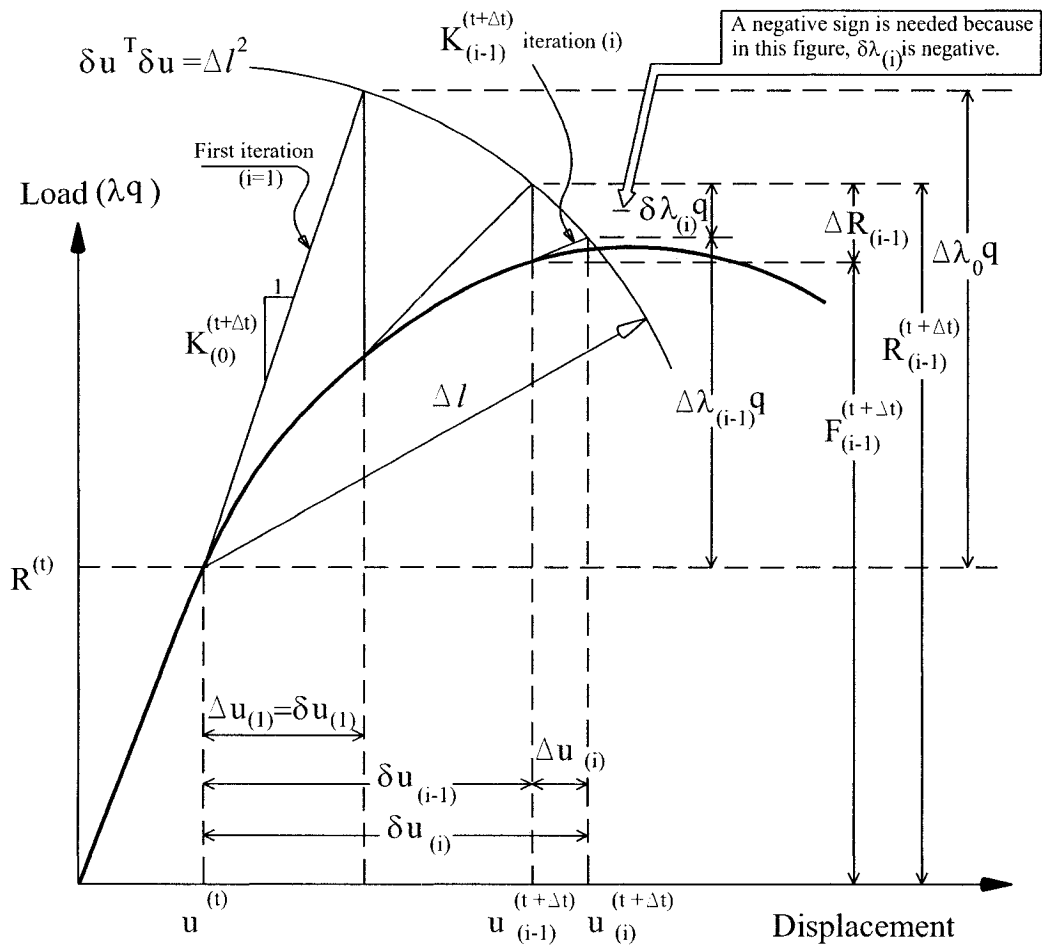


Figure 3.8: Arc-length control technique.

and parameter Δl is kept constant during iterations.

When $\Delta u_{(i)}$ from Equation (3.11) is substituted into the constraint equation (Equation (3.12)), the resulting quadratic equation is given by

$$a_1 \delta \lambda_{(i)}^2 + a_2 \delta \lambda_{(i)} + a_3 = 0 \quad (3.15)$$

where

$$\begin{aligned} a_1 &= \delta u_t^T \delta u_t \\ a_2 &= 2(\delta \bar{u} + \delta u_{(i-1)})^T \delta u_t \\ a_3 &= (\delta \bar{u} + \delta u_{(i-1)})^T (\delta \bar{u} + \delta u_{(i-1)}) - \Delta l^2 \end{aligned} \quad (3.16)$$

Out of the two roots of Equation (3.15), the one which results in the least root mean square error between the solution at the end of the previous iteration $u_{(i-1)}^{(t+\Delta t)}$ and the solution at the end of the current iteration $u_{(i)}^{(t+\Delta t)}$, is selected.

The arc length may also be adjusted such that a more or less constant number of iterations is required to obtain convergence, using the following relation:

$$\Delta l_i = \Delta l_{i-1} N_d / N_{i-1} \quad (3.17)$$

where Δl_i is the constant arc length to be used in the current step, Δl_{i-1} is the constant arc length used in the previous step, N_{i-1} is the number of iterations needed in the previous step and N_d is the desired number of iterations to be performed in any step to obtain convergence based on the chosen convergence criterion.

3.7 Convergence criteria

For any incremental procedure based on iterative methods, to be effective, practical termination schemes should be provided. At the end of each iteration, a check should be made to test if the iteration converged within realistic tolerances or it is diverging.

Very loose tolerance will initiate inaccurate results, while very strict one can needlessly make the computational cost high. On the other side, bad divergence check can end the iterative process when the solution is not diverging or allow the process to continue for searching unrealizable solution. In the following, three convergence criteria for terminating an iterative process will be discussed.

3.7.1 Displacement convergence

This criterion is based on the displacement increments during iterations. It is given by

$$|\Delta U_{(i)}| \leq \varepsilon_d |\Delta U_{(1)}| \quad (3.18)$$

where $||$ denotes the Euclidean norm, and ε_d is the displacement tolerance.

3.7.2 Force convergence

This criterion is based on the out-of-balance (residual) loads during iterations. It requires that the norm of the residual load vector to be within a tolerance ε_f of the applied load increment, i.e.

$$|R^{(t+\Delta t)} - F_{(i-1)}^{(t+\Delta t)}| \leq \varepsilon_f |R^{(t+\Delta t)} - F^{(t)}| \quad (3.19)$$

where ε_f is the force tolerance.

3.7.3 Energy convergence

In this criterion, the increment in the internal energy during each iteration, which is the work done by the residual forces through the incremental displacements, is compared with the initial energy increment. Convergence is assumed to reach when

the following is satisfied:

$$(\Delta U_{(i)})^T (R^{(t+\Delta t)} - F_{(i-1)}^{(t+\Delta t)}) \leq \varepsilon_e (\Delta U_{(1)})^T (R^{(t+\Delta t)} - F^{(t)}) \quad (3.20)$$

where ε_e is the energy tolerance.

3.8 Corotational nonlinear analysis

In this section, the general aspects of corotational approach combined with Newton-Raphson iterative method for the analysis of geometric nonlinear shells modeled by triangular elements are explained. In corotational approach the total motion of an element is decomposed into a rigid body motion and a pure deformation. Then the contribution of the rigid body motion to the total deformation of the element is removed before performing the element computations. This will enable to upgrade the structural elements to treat problems with large rotations but small strains. This is the case with many thin-walled plate and shell structures undergoing large deformations.

Figure 3.9 shows the undeformed (initial) and current configurations of a general triangular shell element, moving in the global coordinate system g . The displacement vector of node i with position vector X_i^g in the global coordinate is denoted by u_i^g . E_0 is the local coordinate system in the initial configuration with the origin at node 1 and axis E_{01} along the side 1-2 and axis E_{03} perpendicular to the element plane. In the current configuration, the position vector of node i is given by $x_i^g = X_i^g + u_i^g$. Using x_i^g , local coordinate system E in the current configuration is established (again with axis E_1 along the current side 1-2 and axis E_3 perpendicular to the current element plane.)

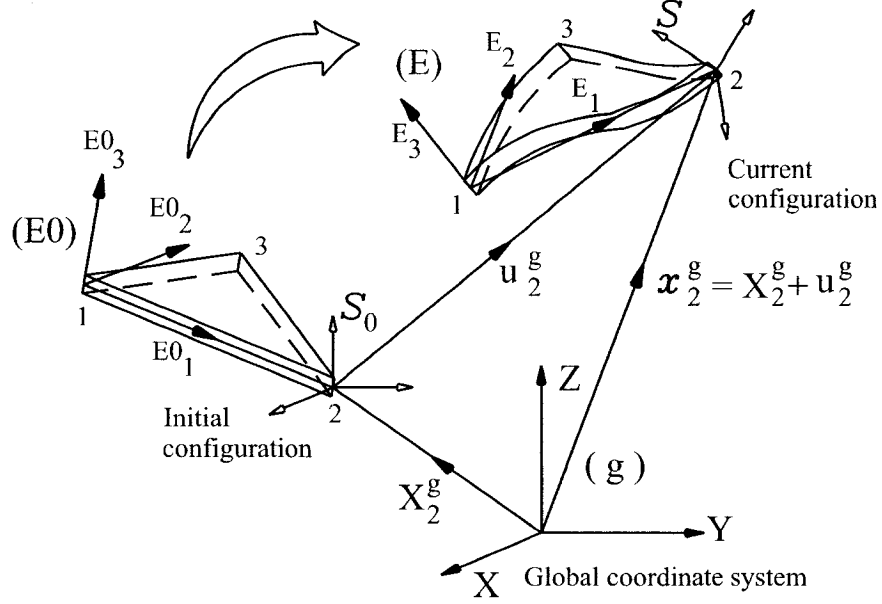


Figure 3.9: Corotational method

Rotations of each node in global system are expressed by a triad which is rigidly tied to the node and rotates with the node from its initial state S_0 (parallel to global system g) to its current state S . Updating triad S for incremental rotations after each iteration is performed by updating its transformation matrix. Based on the definition, the transformation matrix for the coordinate system e is shown as T_e , which transforms vector X_g in global coordinate system into vector X_e in coordinate system e by the orthogonal transformation $X_g = T_e X_e$. Entries of this matrix are direction cosines of coordinate system e with respect to global coordinate system. Assuming $\tilde{\theta}_X$, $\tilde{\theta}_Y$ and $\tilde{\theta}_Z$ as the incremental rotations of triad S resulted from the last iteration computed in global coordinate system, T_S may be updated by the following expression [37]:

$$(T_S)_{new} = \tilde{T} \cdot (T_S)_{old} \quad (3.21)$$

where

$$\tilde{T} = I + \frac{\tilde{\Omega} + 0.5\tilde{\Omega}^2}{1 + 0.25|\omega|^2}, \quad |\omega| = \sqrt{\tilde{\theta}_X^2 + \tilde{\theta}_Y^2 + \tilde{\theta}_Z^2}, \quad \tilde{\Omega} = \begin{bmatrix} 0 & -\tilde{\theta}_Z & \tilde{\theta}_Y \\ \tilde{\theta}_Z & 0 & -\tilde{\theta}_X \\ -\tilde{\theta}_Y & \tilde{\theta}_X & 0 \end{bmatrix}. \quad (3.22)$$

Pure nodal rotations in local coordinate system E may be computed by the following two steps [37]:

I) An orthogonal transformation matrix T , which describes rotation of nodal triad S_0 to S in local coordinate E , is found by the following expression:

$$T = T_E^T T_S T_{E_0} \quad (3.23)$$

where T_E , T_S , and T_{E_0} are the transformation matrices for coordinate system E , triad S , and coordinate system E_0 , respectively.

II) Pure nodal rotations expressed in E are equal to the components of an anti-symmetric matrix $\Omega_{3 \times 3}$ (called spin tensor) as [37]

$$\Omega = \begin{bmatrix} 0 & -\theta^{E_3} & \theta^{E_2} \\ \theta^{E_3} & 0 & -\theta^{E_1} \\ -\theta^{E_2} & \theta^{E_1} & 0 \end{bmatrix} \quad (3.24)$$

where Ω is found by the following expression using orthogonal matrix T computed in step (I):

$$\Omega = 2(T - I)(T + I)^{-1} \quad (3.25)$$

Pure nodal displacements in E are computed by comparing the current configuration with a “corotated” configuration (which is exactly similar to the initial configuration and is considered in the $E_1 E_2$ plane) with nodes $\hat{1}, \hat{2}$ and $\hat{3}$, coinciding points $\hat{1}$ and 1 and also sides $\hat{1} - \hat{2}$ and $1 - 2$, as shown in Figure 3.10. Pure nodal

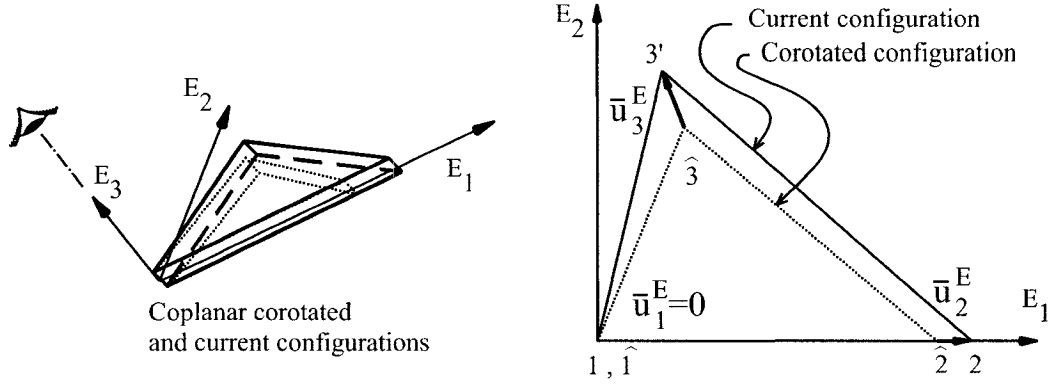


Figure 3.10: Coplanar corotated and current configurations

displacements at node i in E may be expressed by the relation [37]

$$\bar{u}_i^E = \begin{Bmatrix} \bar{u}_i^{E1} \\ \bar{u}_i^{E2} \\ \bar{u}_i^{E3} \end{Bmatrix} = T_E^T (u_i^g + X_i^g - u_1^g - X_1^g) - X_i^{E0} \quad i = 1, 2, 3 \quad (3.26)$$

where X_i^{E0} is the initial coordinates of node i in E_0 . \bar{u}_i^E components are shown in Figure 3.10. Obviously \bar{u}_i^{E3} (the pure nodal translations in E_3 direction) are zero, since both corotated and current configurations are coplanar.

Finally the pure deformations at node i computed in local coordinate system E can be expressed as

$$d_i = \begin{Bmatrix} \bar{u}_i^{E1} \\ \bar{u}_i^{E2} \\ \bar{u}_i^{E3} \\ \theta_i^{E1} \\ \theta_i^{E2} \\ \theta_i^{E3} \end{Bmatrix} \quad i = 1, 2, 3 \quad (3.27)$$

In case that these pure deformations are small, a *linear* theory may be adopted to bring the nodes $\hat{1}, \hat{2}$ and $\hat{3}$ of corotated configuration into their final positions 1, 2 and 3 [43]. In this case the stiffness matrix of the corotated element in E (which is the same as the stiffness matrix of initial element in E_0) may be used to compute the local element forces f . However, some difficulties are observed with this approach. The computed local element forces f will be naturally related to the points $\hat{1}, \hat{2}, \hat{3}$ rather

than the actual nodal positions 1, 2, 3. In other words, f will not be a self-equilibrating set of forces on the current configuration. Also these pure deformations are not really *pure* (without rigid body motion), which can cause problem in case that the element stiffness matrix does not have the correct rigid body properties. The problem is even more severe in warping-sensitive elements like many four node quadrilateral shell elements [39]. In order to overcome such difficulties, a projector matrix with a number of interesting properties is used [39, 40]. The action of the projector matrix on a non-equilibrated force vector brings it into equilibrium. Moreover, the rigid body components of an incremental displacement vector are eliminated when multiplied by the projector matrix. Finally it can transform a linear element stiffness matrix to one with correct rigid body properties. Nodal deflections d , vector of the internal forces f , and element stiffness matrix k can be modified using the projection matrix P as [39]

$$\bar{d} = P d \quad (3.28)$$

$$\bar{f} = P^T f \quad (3.29)$$

$$\bar{k} = P^T k P \quad (3.30)$$

The results of this transformation are to produce \bar{d} as the vector of pure deformational part of the nodal deflections, \bar{f} as a self-equilibrating set of nodal forces, and \bar{k} as a stiffness matrix with correct rigid body modes. The potential energy of the element associated with deformations \bar{d} , stiffness matrix \bar{k} , and nodal force vector \bar{f} may be expressed as

$$\phi = \frac{1}{2} d^T \bar{k} d - d^T \bar{f} \quad (3.31)$$

Considering that P is a projector matrix (i.e. $P^2 = P$), it can be seen that ϕ is still equal to the energy computed by stiffness matrix k and nodal force f during the pure deformations \bar{d} , but now the nodal force vector \bar{f} , strain energy ϕ , and stiffness matrix \bar{k} correspond to the new (current) configuration, and nodal forces \bar{f} are in self equilibrium.

The general form of the projection matrix is $P = I - \Psi \Gamma^T$ where Ψ components for each node is the cross-product operator (skew-symmetric matrix) corresponding to the current relative position vector of the node, and Γ represents the variation of the base vectors of local system with respect to the displacements at all nodes [39]. For triangular element shown in Figure 3.10 with local coordinate axis E_1 along the edge 1 – 2 we have [39, 43]

$$\Psi_{18 \times 3} = \begin{bmatrix} 0 & 0 & 0 & 0 & 0 & 0 & 0 & E_3^2 & 0 & 0 \\ 0_{3 \times 3} & I_{3 \times 3} & 0 & 0 & -E_2^1 & I_{3 \times 3} & 0 & 0 & -E_3^1 & I_{3 \times 3} \\ 0 & E_2^1 & 0 & -E_3^2 & E_3^1 & 0 & 0 & 0 & 0 & 0 \end{bmatrix}^T \quad (3.32)$$

and

$$\Gamma_{18 \times 3} = \begin{bmatrix} 0 & 0 & \frac{E_3^1 - E_2^1}{E_3^2 E_2^1} & 0 & 0 & -\frac{E_3^1}{E_3^2 E_2^1} & 0 & 0 & \frac{1}{E_3^2} & 0 \\ 0 & 0 & \frac{1}{E_2^1} & 0_{3 \times 3} & 0 & 0 & -\frac{1}{E_2^1} & 0_{3 \times 3} & 0 & 0 \\ 0 & -\frac{1}{E_2^1} & 0 & 0 & \frac{1}{E_2^1} & 0 & 0 & 0 & 0 & 0 \end{bmatrix}^T \quad (3.33)$$

where E_i^1, E_i^2, E_i^3 are the coordinates of node i in E .

Figure 3.11 shows a typical algorithm for corotational nonlinear analysis with force control. At each load level, the new local coordinate system E is established using only the new nodal global positions. Then pure nodal deformations d in coordinate system E are found using the method explained before. Nodal forces $f = k d$ are found in coordinate system E using the element stiffness matrix k . projector matrix P is operated on k and f to get modified stiffness matrix \bar{k} and force vector \bar{f} . If

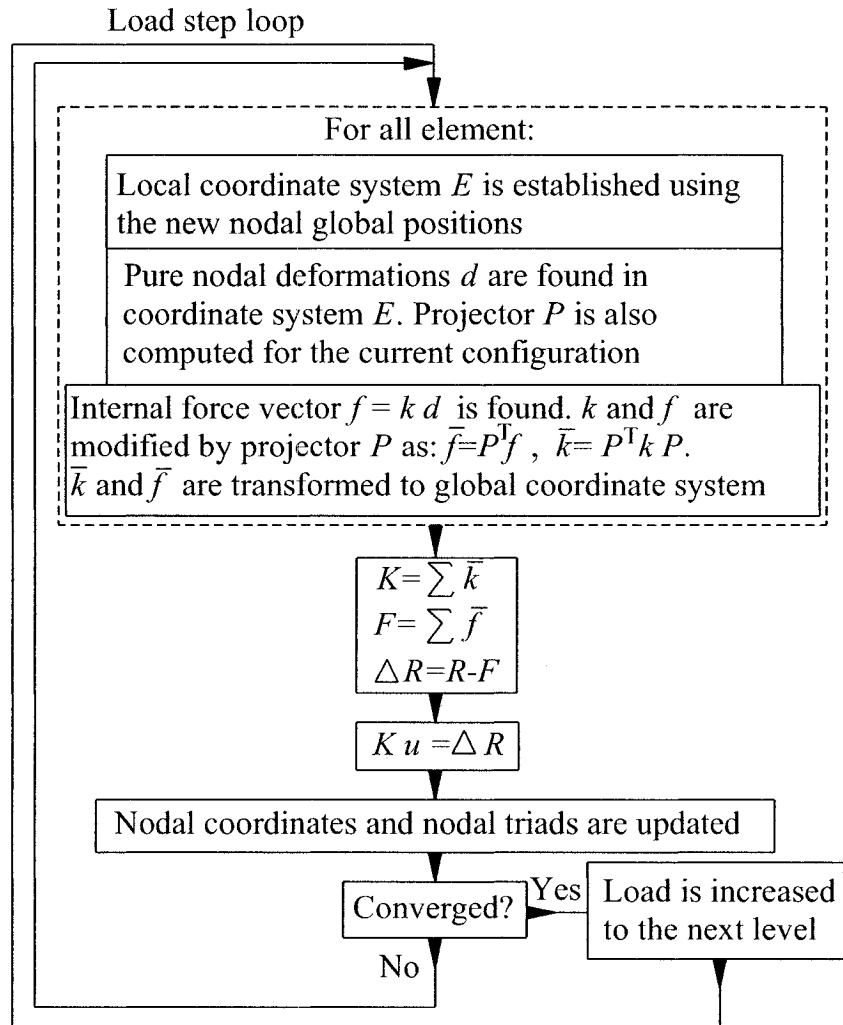


Figure 3.11: Flowchart of the corotational nonlinear analysis

membrane forces are significant, particularly in compression, stress stiffness matrix k_σ should also be added to the stiffness matrix at this stage. Transforming \bar{k} and \bar{f} to the global coordinate system, the procedure is repeated for all elements to assemble current structure stiffness $K = \Sigma \bar{k}$ and balanced force $F = \Sigma \bar{f}$. Load imbalance (residual) ΔR is found by subtracting F from the vector of applied loads R . Structural stiffness equation $K \Delta u = \Delta R$ is then solved for displacement increments Δu . Nodal global coordinates are updated adding the incremental nodal displacements to the nodal coordinates, whereas rotational state of each node is updated by updating nodal triad S . Convergence is checked, and if it is not satisfied the whole process repeats, otherwise load R is increased to the next level. Similar algorithms may be used with displacement or arc-length controls.

It should be mentioned that due to the change of variables from rotations to spin tensor in Equations (3.24) and (3.25), some convergence problems may arise. However when the element deformations are sufficiently small, this effect is less. Usually the correctness of the results is not affected by this approximation [40, 43]. Also Equations (3.21) and (3.22) for updating triad S are valid only for rotations up to about 30 degrees [37]. As a result, convergence for large load steps may be difficult in most cases.

3.9 Computation for critical points

There are two different types of critical points. A limit point arises when the load-displacement curve reaches a local extremum, as the points B and C shown in Figure 3.12, while a bifurcation occurs when different equilibrium paths meet at a certain

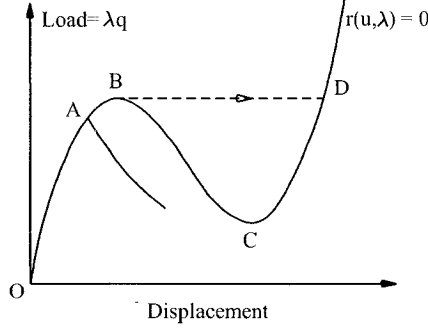


Figure 3.12: Equilibrium paths and critical points.

point, as the point A in Figure 3.12. Detection and classification of the critical points are usually performed by checking the null eigenvector condition, and orthogonality between the load vector and the buckling mode [118]:

$$K(u, \lambda)\vartheta = 0 \quad (3.34)$$

where K is the tangent stiffness matrix and ϑ is the associated eigenvector representing the buckling mode. Critical points can be classified using the following criteria [118]:

$$\begin{aligned} \vartheta^T R = 0 &\Rightarrow \text{bifurcation point} \\ \vartheta^T R \neq 0 &\Rightarrow \text{limit point} \end{aligned} \quad (3.35)$$

Figure 3.13 shows two cases of nonlinear response with limit loads. Graph (a) is called “snap-through behavior”, which is one of the most frequent forms of nonlinear response of shallow structures. Graph (b) shows another case in which the structure has no post-buckling strength. In both cases the limit point is identified as the point in which the tangent stiffness matrix becomes singular. The load level at the limit point is selected as the constraint for optimization against system stability.

In practical cases, the tangent stiffness matrix rarely becomes exactly singular, thus in this study an alternative method is used to find the limit load of the nonlinear

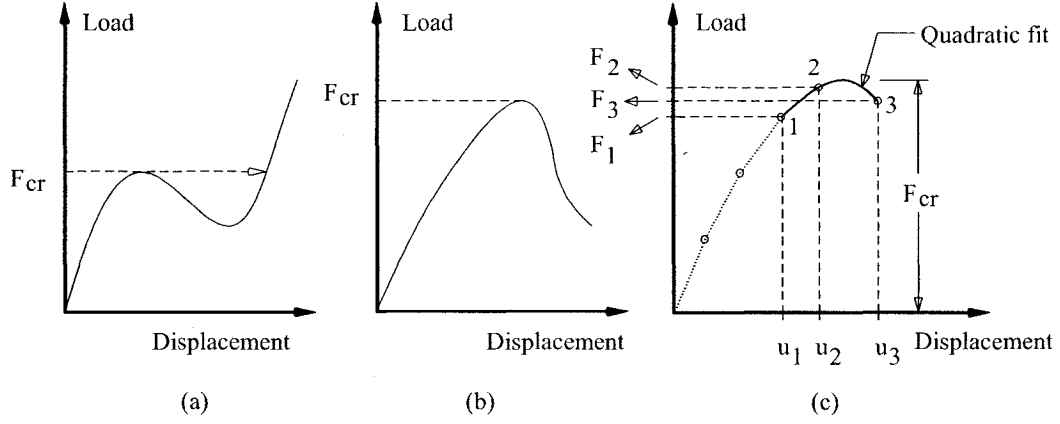


Figure 3.13: Two forms of the nonlinear response curve with limit load

path. Since the arc-length method is capable to trace the post buckling path, one can use this method to follow the equilibrium path beyond the limit point. As shown in Figure 3.13(c), analysis is stopped when the load level at a newly converged point of the path (point 3) becomes less than that of the previous converged point (point 2). Now, using the values corresponding to the three last points 1, 2 and 3, it is possible to perform a quadratic fit to the load displacement curve near the limit point and find F_{cr} . The peak load determined through this procedure was found to be very accurate.

The critical load found by the nonlinear analysis is used in the shape optimization problem of the geometrically nonlinear structure. In the next chapter, methodology for shape optimization in order to maximize the critical load of the structure is explained.

Chapter 4

Structural Design Optimization

4.1 Introduction

In this chapter, the shape optimization problem is described in detail. First, the definition of the shape design variables is presented, and the general form of the shape optimization problem and its solution using the gradient-based optimization algorithm are explained. Then the alternative method of optimality criteria for two cases of load-capacity maximization under constant mass (along with its application on the design of stiffened panels), and mass minimization under constant load are explained. Finally, the shape optimization methodology is modified to consider the effect of local buckling in stiffened panels.

4.2 Geometry and thickness design variables

Figure 4.1 shows an example of a thin-walled structure modeled by facet elements. We assume that the length of this structure is kept constant, thus the shape is defined by seven design variables $a, b, c, d, t_1, t_2, t_3$. In this study, variables such as a, b, c , and d which control the nodal positions in finite element model, are called “geometry

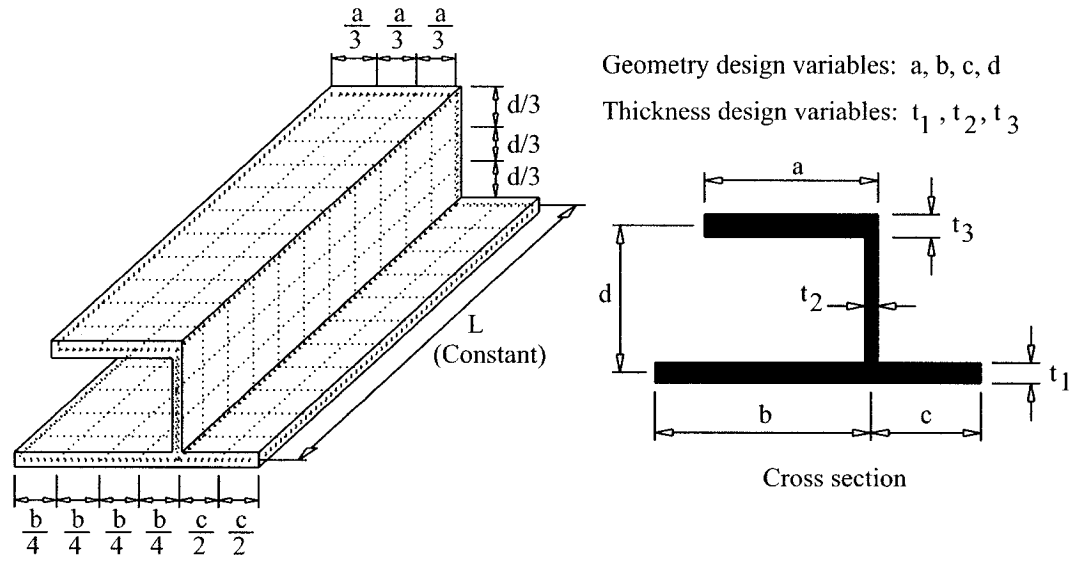


Figure 4.1: Geometry and thickness design variables.

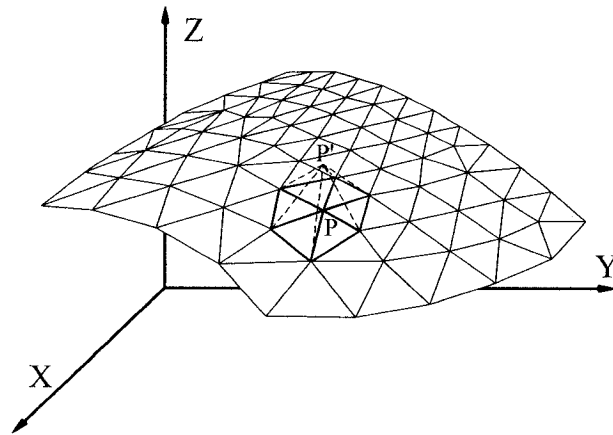


Figure 4.2: Nodal coordinate as the geometry design variable.

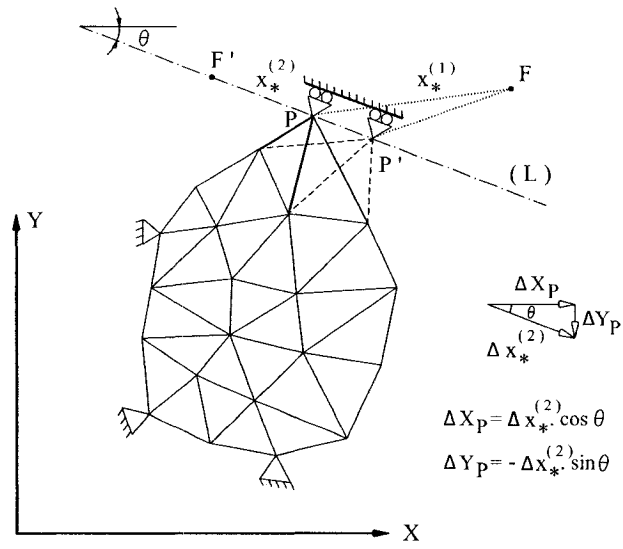


Figure 4.3: Various forms to define the geometry design variables.

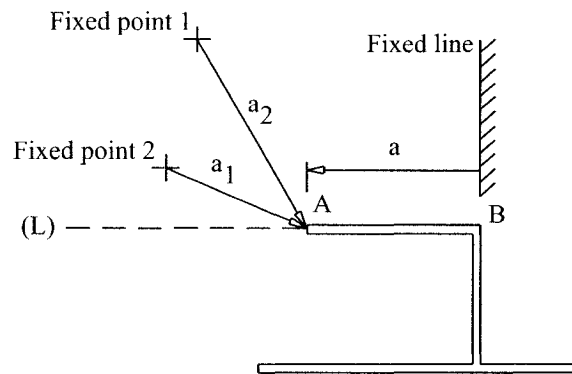


Figure 4.4: Various forms to define the geometry design variable a in Figure 4.1.

design variables”. The rest of the design variables (i.e. t_1, t_2 , and t_3) which control the thickness of the elements, are called “thickness design variables”. As an example, Figure 4.2 shows that how nodal global coordinate can be selected (here, coordinate Z of the point P) as a geometry design variable to control the nodal position.

A geometry design variable can be defined in various ways since it can be measured from various origins and in various directions. Figure 4.3 shows how a geometry design variable may be defined to control the position of the point P with inclined boundary condition. Assuming that the points P and P' are the positions of a free nodal point moving on line (L) during the optimization process, geometry design variable $x_\star^{(1)}$ can be selected as the distance of the free node from a fixed point F . Another way to describe the position of the point is measuring the distance from a fixed point F' on the line (L) using the geometry design variable $x_\star^{(2)}$. It is obvious that the number of ways to define a geometry design variable (to describe the position of a node) is infinite. Similarly, Figure 4.4 shows how the geometry design variable a in Figure 4.1 may be defined in other ways. Considering that point B is fixed and point A is moving horizontally on line (L), parameter a_1 or a_2 may also be selected (as the distance of point A from a selected fixed point), to control the position of point A .

It is important to note that the change of the shape during optimization should not violate the design constraints or manufacturing requirements. Any manufacturing requirement such as a straight edge remaining straight or portions of the boundary remaining unchanged should be considered when defining a shape design variable. Some studies consider an auxiliary structure to satisfy these requirements during the shape optimization [151, 152]. In the present study, change of the shape is performed

by shape design variables which do not violate the design constraints and boundary conditions.

4.3 Optimization problem

We assume that a plate or shell structure is analyzed under the applied force vector λq in which q is a constant reference force vector, and λ is a load level factor which is gradually increased until the stability constraint is violated. At this instant, λq is called the “critical load” of this structure with respect to the stability constraints, and is shown as $\lambda_c q$. Considering X as the vector of the shape design variables, the optimization problem is to maximize the critical load factor λ_c subject to the constant total mass M_0 :

Maximize (λ_c) **Subject to:**

$$h(X) = M - M_0 = 0$$

$$X_L \leq X \leq X_U$$

where $h(X)$ is the equality constraint, X_L , and X_U are the lower and upper bounds on the design variables X , and M and M_0 are the total mass and constant value for the total mass, respectively. The Lagrangian can be defined as

$$L(X, \mu) = -\lambda_c + \mu \cdot h \tag{4.1}$$

where μ is the Lagrange multiplier. The stationarity conditions of this function (Karush-Kuhn-Tucker conditions [128]) together with the equilibrium equation and critical point condition, describe the optimization problem as:

$$-\nabla_X \lambda_c + \mu \cdot \nabla_X h = 0 ; \quad \nabla_X : \text{total derivative}$$

$$h = 0$$

$$F - \lambda q = 0$$

$$K(u, \lambda) \vartheta = 0$$

$$\| \vartheta \| - 1 = 0$$

where K is the tangent stiffness matrix, ϑ is representing the buckling mode, and F is the internally generated nodal forces. This nonlinear system of equations has to be solved within the optimization loop. Optimization process starts with the analysis of the structure and computation of the critical point. At the critical point, the sensitivity analysis is performed and a search direction ΔX is produced which is used in the line-search procedure. Using the first guess $\alpha = 1.0$ for the step length, and letting $X = X + \alpha \Delta X$, a new analysis is performed. If there is no improvement, the line-search procedure generates a new step length α and the structural analysis is repeated until an improvement is obtained. The process repeats, continuing with the sensitivity analysis until the optimum design is reached.

4.4 Sensitivity analysis

Sensitivity analysis is an important and computationally expensive part of the gradient-based optimization algorithms. The main task during the sensitivity analysis is to obtain the derivatives of the solution (u_c, λ_c) for the critical points with respect to the optimization variables X . For the sake of simplicity and without loss of generality, it will be considered that the shape of the structure is controlled by only one design variable x . First, the system of equilibrium equations is rewritten in terms of the variables u, x [118]:

$$F(u, x) - \lambda q(x) = 0 \tag{4.2}$$

where F is the internally generated nodal forces. Differentiation of this equation yields [118]

$$\frac{\partial F}{\partial u} \frac{du}{dx} + \frac{\partial F}{\partial x} - \frac{d\lambda}{dx} q - \lambda \frac{dq}{dx} = 0 \quad (4.3)$$

Since $K = \partial F / \partial u$, Equation (4.3) can be rewritten as

$$K \frac{du}{dx} - \frac{d\lambda}{dx} q = \lambda \frac{dq}{dx} - \frac{\partial F}{\partial x} = p \quad (4.4)$$

where p is called the “pseudo-load” vector [118]. Multiplying Equation (4.4) by ϑ^T and using the critical load condition ($\vartheta^T K = 0$), we obtain

$$\frac{d\lambda}{dx} = - \frac{\vartheta^T p}{\vartheta^T q} \quad (4.5)$$

This equation can be used for the computation of the critical load sensitivity. However, it can not be used at bifurcation points since the product $\vartheta^T q$ vanishes.

In order to compute the sensitivity of a bifurcation load, we start with Equation (3.34) and differentiate it with respect to x [118]:

$$\frac{d(K\vartheta)}{dx} = \frac{\partial(K\vartheta)}{\partial u} \frac{du}{dx} + \frac{\partial K}{\partial x} \vartheta + K \frac{\partial \vartheta}{\partial x} = 0 \quad (4.6)$$

Using Equation (4.4) we have

$$\frac{du}{dx} = \frac{d\lambda}{dx} \delta u_q + \delta u_p \quad (4.7)$$

where

$$\begin{aligned} K \delta u_q &= q \\ K \delta u_p &= p \end{aligned} \quad (4.8)$$

Substituting Equation (4.7) into Equation (4.6) leads to

$$\frac{d\lambda}{dx} \frac{\partial(K\vartheta)}{\partial u} \delta u_q + \frac{\partial(K\vartheta)}{\partial u} \delta u_p + \frac{\partial K}{\partial x} \vartheta + K \frac{\partial \vartheta}{\partial x} = 0 \quad (4.9)$$

Multiplying this equation by ϑ^T and using the condition $\vartheta^T K = 0$, the following expression is obtained for the computation of the sensitivity of bifurcation loads [118]:

$$\frac{d\lambda}{dx} = -\frac{\vartheta^T(h_p + w)}{\vartheta^T h_q} \quad (4.10)$$

where $w = (\partial K/\partial x)\vartheta$, and h_p and h_q are the directional derivatives defined as $h_q = (K\vartheta)_{,u}\delta u_q$ and $h_p = (K\vartheta)_{,u}\delta u_p$ in which $(K\vartheta)_{,u}$ is computed using the finite difference method. Although it seems impossible to use Equation (4.8) because of singularity of the stiffness matrix at a critical point, this expression can be applied in most practical cases since we will rarely reach a precise singular point during solution.

As an alternative approach, the finite difference method (FDM) may also be used for sensitivity analysis:

$$\frac{d\lambda}{dx} = \frac{\lambda(x + \Delta x) - \lambda(x)}{\Delta x} \quad (4.11)$$

The accuracy of the FDM is strongly dependent on the perturbation size Δx . A relative perturbation between 10^{-5} and 10^{-8} generally leads to results with sufficient accuracy for engineering applications. The major drawback of the FDM is its high computational cost, thus it is mainly used in validation of other schemes for sensitivity analysis.

4.5 Optimality criteria for load–capacity maximization of thin-walled structures, subject to constant mass

4.5.1 Derivation of the optimality criteria

As mentioned before, optimality criterion method significantly reduces the time and cost of the optimization process for geometrically nonlinear structures since the time-consuming task of sensitivity analysis is not required in this method. In this section two optimality criteria are developed for load–capacity maximization subject to constant mass, using Karush-Kuhn-Tucker conditions [128].

As described in section 4.3, the optimization problem is to find the optimum values for shape design variables in order to maximize λ_c subject to constant total mass

$$M = \sum_{i=1}^N \rho_i V_i = M_0 \quad (4.12)$$

where N is the number of elements, ρ_i is the material density of the i^{th} element, and $V_i = t_i A_i$ is the volume of the i^{th} element with area A_i and thickness t_i , and M_0 is a constant. The Lagrangian for this optimization problem is

$$L = -\lambda_c + \mu(M - M_0) \quad (4.13)$$

where μ is the Lagrange multiplier. Assuming $X = \{x_1, x_2, \dots, x_s\}^T$ as the vector of shape design variables (whether the geometry or thickness design variables), the KKT conditions [128] for minimization of L with respect to X become

$$\frac{\partial L}{\partial x_l} = 0 \quad ; \quad l = 1, \dots, s \quad (4.14)$$

Thus

$$-\frac{\partial \lambda_c}{\partial x_l} + \mu \sum_{i=1}^N \rho_i \frac{\partial V_i}{\partial x_l} = 0 \quad ; \quad l = 1, \dots, s \quad (4.15)$$

where s is the number of shape design variables. Now we write the total potential energy of the structure as

$$\Pi = \sum_{i=1}^N e_i - \lambda_c u^T q \quad (4.16)$$

where u and $\lambda_c q$ are the nodal displacement vector in the global coordinate system and the vector of the applied loads, respectively, and e_i is the strain energy of the i^{th} element which may be written in terms of the vector of the pure nodal displacements after removing the rigid body motions due to large deflections. It should be mentioned that pure displacements may also be written generally as a function of global displacement vector $\{u\}$. Considering Π_{opt} as the total potential energy associated with the optimum design, the equation $\Pi = \Pi_{opt}$ should also be satisfied for the optimum design. Taking derivative from both sides of this equation with respect to design variable x_l (noticing that u and λ_c are also functions of the design variable x_l) we have

$$\sum_{i=1}^N \frac{\partial e_i}{\partial x_l} + \sum_{j=1}^m \frac{\partial \Pi}{\partial u_j} \frac{\partial u_j}{\partial x_l} + \frac{\partial \Pi}{\partial \lambda_c} \frac{\partial \lambda_c}{\partial x_l} = 0 \quad ; \quad l = 1, \dots, s \quad (4.17)$$

where m is the number of the nodal displacement components. From the principle of stationary total potential energy we have $\frac{\partial \Pi}{\partial u} = 0$, thus Equation(4.17) changes to

$$\sum_{i=1}^N \frac{\partial e_i}{\partial x_l} + 0 - u^T q \frac{\partial \lambda_c}{\partial x_l} = 0 \quad ; \quad l = 1, \dots, s \quad (4.18)$$

in which $\frac{\partial \Pi}{\partial \lambda_c}$ has been substituted by $-u^T q$. Substituting for $\frac{\partial \lambda_c}{\partial x_l}$ from Equation (4.15) into (4.18) results in

$$\mu \sum_{i=1}^N \rho_i \frac{\partial V_i}{\partial x_l} - \frac{1}{u^T q} \sum_{i=1}^N \frac{\partial e_i}{\partial x_l} = 0 \quad ; \quad l = 1, \dots, s \quad (4.19)$$

or

$$\sum_{i=1}^N \rho_i \frac{\partial V_i}{\partial x_l} - \Lambda \sum_{i=1}^N \frac{\partial e_i}{\partial x_l} = 0 \quad ; \quad l = 1, \dots, s \quad (4.20)$$

where $\Lambda = 1/(\mu u^T q)$

In the case that x_l is a thickness design variable, Equation (4.20) leads to

$$\sum_{x_l} \rho_i A_i - \Lambda \sum_{x_l} \frac{\partial e_i}{\partial x_l} = 0 \quad (4.21)$$

where \sum_{x_l} means that the sum is on all the elements related to thickness design variable x_l . Equation (4.21) may be simplified as

$$1 = \Lambda \left(\frac{\sum_{x_l} \partial e_i / \partial x_l}{\sum_{x_l} \rho_i A_i} \right) = \Lambda \tilde{e}_{x_l} \quad (4.22)$$

where \tilde{e}_{x_l} is called “average strain energy variation” for the thickness design variable x_l . Equation (4.22) (hereinafter called “Uniform Average Strain Energy Variation” or UASEV criterion) states that in a structure with optimum thickness, \tilde{e} or average strain energy variation is the same for all thickness design variables.

For x_l being a geometry design variable, Equation (4.20) leads to

$$\left(\sum_{x_l} \rho_i t_i \frac{\partial A_i}{\partial x_l} \right) - \Lambda \left(\sum_{x_l} \frac{\partial e_i}{\partial A_i} \frac{\partial A_i}{\partial x_l} \right) = 0 \quad (4.23)$$

Since the strain energy of a facet element is in proportion to the element area (see Equation (4.35)), $\partial e_i / \partial A_i = e_i / A_i$. Thus

$$\sum_{x_l} \left(\rho_i t_i - \Lambda \frac{e_i}{A_i} \right) \left(\frac{\partial A_i}{\partial x_l} \right) = 0 \quad (4.24)$$

As mentioned before, geometry design variables can be defined in various ways since they can be measured from various origins and in various directions. Considering the fact that the final optimum shape should be independent of how a geometry design

variable is defined, the only possible way to satisfy this equation is

$$\left(\rho_i t_i - \Lambda \frac{e_i}{A_i} = 0 \right)_{x_l} \quad (4.25)$$

or

$$(\rho_i t_i A_i = \Lambda e_i)_{x_l} \quad (4.26)$$

where $()_{x_l}$ means that the equation is valid for all elements affected by the geometry design variable x_l . In order to obtain an equation similar to Equation (4.22), we consider Equation (4.26) for all elements affected by the geometry design variable x_l :

$$\sum_{x_l} \rho_i t_i A_i = \Lambda \sum_{x_l} e_i \quad (4.27)$$

or

$$1 = \Lambda \left(\frac{\sum_{x_l} e_i}{\sum_{x_l} \rho_i t_i A_i} \right) = \Lambda \hat{e}_{x_l} \quad (4.28)$$

where again \sum_{x_l} means that the sum is on all the elements modified by x_l . In this case, \hat{e} is called “average strain energy density”. Equation (4.28) (hereinafter called “Uniform Average Strain Energy Density” or UASED criterion) states that in a structure with optimum nodal positions, \hat{e} or average strain energy density is the same for all geometry design variables.

Equations (4.22) and (4.28) are called the “optimality criteria” and should be satisfied through an iterative process in order to obtain the optimum design. In the next section, this iterative process is explained. It should be noted that since the second variation of the Lagrangian was not examined in this study, these optimality criteria are only empirical local-optimality conditions. Also, since these criteria are satisfied only at the final load (load capacity), it assumes monotonic structural behavior and excludes path dependency.

It should be noted that the optimality criteria found here, are valid for displacement or stress constraints as well. The only difference is that the load capacity of the structure is found based on these constraints and the optimality criteria are also satisfied at that load level (load capacity).

4.5.2 Recurrence relation

In order to satisfy an optimality criterion, an iterative scheme is used. Substituting x_l by x for simplicity, a recurrence relation may be written by multiplying both sides of Equations (4.22) or (4.28) by x and taking the r^{th} root as

$$(x)_{\eta+1} = (x)_{\eta} \cdot (\Lambda \bar{e}_x)^{1/r} \quad (4.29)$$

where $\eta + 1$ and η are the iteration numbers, and r is the step size parameter which can be changed by assigning appropriate value, and \bar{e}_x is defined as

$$\bar{e}_x = \begin{cases} \frac{\sum_x \partial e_i / \partial x}{\sum_x \rho_i A_i}; & \text{if } x \text{ is a thickness design variable} \\ \frac{\sum_x e_i}{\sum_x \rho_i t_i A_i}; & \text{if } x \text{ is a geometry design variable} \end{cases} \quad (4.30)$$

The value of Λ at the optimal design is determined by minimizing the sum of the squares of the residuals at iteration η :

$$Res_{\eta} = \sum_{i=1}^s (1 - \Lambda \bar{e}_i)^2 \quad (4.31)$$

Thus, Λ can be obtained as

$$\Lambda = \left(\sum_{i=1}^s \bar{e}_i \right) / \left(\sum_{i=1}^s \bar{e}_i^2 \right) \quad (4.32)$$

Substituting Equation (4.32) into Equation (4.29) we finally obtain

$$(x)_{\eta+1} = (x)_{\eta} \cdot \left(\left(\sum_{i=1}^s \bar{e}_i \right) / \left(\sum_{i=1}^s \bar{e}_i^2 \right) \cdot \bar{e}_x \right)^{1/r}_{\eta} \quad (4.33)$$

This equation is used at the limit or bifurcation point in order to iteratively modify the geometry or the thickness design variables and obtain the optimum shape. The new design variables after each iteration are scaled to satisfy the volume equality constraint, and the process repeats until the following condition for the convergence is satisfied:

$$(\Delta\lambda)_\eta \leq (tol) \cdot (\Delta\lambda)_1 \quad (4.34)$$

where $(\Delta\lambda)_1$ and $(\Delta\lambda)_\eta$ is the change in the critical load factor in the first and η^{th} iteration respectively, and tol is usually chosen in the range of $tol \leq 10^{-2}$ depending on the accuracy required.

4.5.3 Strain energy

Equations (4.29) and (4.30) contain strain energy of the elements affected by the design variables at the limit or bifurcation point. For a flat shell element, in the case of isotropic material with the Poisson's ratio ν and the Young's modulus E_o , e_i can be obtained by the following relation:

$$e_i = \frac{1}{2} \int_{A_i} (\{\varepsilon_m\}^T A_i^e \{\varepsilon_m\} + \{\varepsilon_b\}^T D_i^e \{\varepsilon_b\}) dA_i \quad (4.35)$$

where A_i^e and D_i^e are the membrane and flexural stiffness matrices at the location of the i^{th} element with thickness t_i , respectively, and can be written as:

$$A_i^e = \frac{E_o t_i}{1 - \nu^2} \begin{bmatrix} 1 & \nu & 0 \\ \nu & 1 & 0 \\ 0 & 0 & \frac{1-\nu}{2} \end{bmatrix}, \quad D_i^e = \frac{E_o t_i^3}{12(1 - \nu^2)} \begin{bmatrix} 1 & \nu & 0 \\ \nu & 1 & 0 \\ 0 & 0 & \frac{1-\nu}{2} \end{bmatrix} \quad (4.36)$$

and $\{\varepsilon_m\} = \{\varepsilon_x^\circ \ \varepsilon_y^\circ \ \gamma_{xy}^\circ\}^T$ and $\{\varepsilon_b\} = \{\kappa_x^\circ \ \kappa_y^\circ \ \kappa_{xy}^\circ\}^T$ are the membrane and flexural strains in the mid-surface of the i^{th} element respectively. In the case that x is a

thickness design variable, the value of $\frac{\partial e_i}{\partial x}$ for $x = t_i$ is:

$$\frac{\partial e_i}{\partial t_i} = \frac{1}{2} \int_{A_i} \left(\{\varepsilon_m\}^T \cdot \frac{A_i^e}{t_i} \cdot \{\varepsilon_m\} + \{\varepsilon_b\}^T \cdot \frac{3D_i^e}{t_i} \cdot \{\varepsilon_b\} \right) dA_i \quad (4.37)$$

and $\frac{\partial e_i}{\partial x}$ is zero when $x \neq t_i$. It should be noted that $\frac{\partial e_i}{\partial t_i}$ computed by Equation (4.37)

is different from $\frac{e_i}{t_i}$:

$$\frac{e_i}{t_i} = \frac{1}{2} \int_{A_i} \left(\{\varepsilon_m\}^T \cdot \frac{A_i^e}{t_i} \cdot \{\varepsilon_m\} + \{\varepsilon_b\}^T \cdot \frac{D_i^e}{t_i} \cdot \{\varepsilon_b\} \right) dA_i \quad (4.38)$$

and as a result, for the general case of the membrane and bending deformations, UASEV and “Uniform Strain Energy Density (USED)” criteria are not equivalent.

4.6 Optimality criteria for mass minimization of thin-walled structures subject to constant load

The problem of mass minimization subject to constant load is equivalent to the problem of load maximization subject to the constant mass. Thus, the optimality criteria found in the previous section are valid for mass minimization problems as well. Here, we consider a special case in which the design variables are the geometry design variables and one overall thickness variable. The optimization problem is to find a set of design variables X to minimize the total mass M :

$$M = \rho t \sum_{i=1}^N A_i \quad (4.39)$$

for a shell with overall thickness t under constant applied force vector R subject to the constraint:

$$\Pi - \tilde{\Pi} = 0 \quad (4.40)$$

where N and ρ are the number of elements, and material density of the structure respectively. A_i is the area of the i^{th} flat shell element, Π is the total potential energy

and $\tilde{\Pi}$ is the total potential energy associated with the optimum design, satisfying any design constraint such as stability, displacement, ... Here, as mentioned before, the set of design variables X consists of geometry design variables, x_* , and overall thickness of the shell, t . In order to simplify the presentation, and without loss of generality, it will be considered that the shape of the structure is described by only one shape design variable x_* , and overall thickness t . The total potential energy of the structure may be expressed as

$$\Pi = \sum_{i=1}^N e_i - u^T R = U - u^T R \quad (4.41)$$

where U is the total strain energy of the thin shell, u is the global nodal displacement vector, and R is the vector of the externally applied loads. From the principal of stationary total potential energy, we have

$$\frac{\partial \Pi}{\partial u} = \frac{\partial U}{\partial u} - R = 0 \quad (4.42)$$

Using Equations (4.39) and (4.40) the Lagrangian can be defined as

$$L = \rho t \sum_{i=1}^N A_i - \mu(\Pi - \tilde{\Pi}) \quad (4.43)$$

where μ is the Lagrange multiplier. The KKT conditions [128] for minimization of L with respect to shape design variable x_* and thickness t become

$$\frac{\partial L}{\partial x_*} = 0 \quad (4.44)$$

$$\frac{\partial L}{\partial t} = 0 \quad (4.45)$$

$$\Pi - \tilde{\Pi} = 0 \quad (4.46)$$

It is obvious that in case of several shape design variables, Equation (4.44) is valid for each x_* . From Equations (4.44), (4.43) and (4.41) we have

$$\rho t \left(\sum_{x_*} \frac{\partial A_i}{\partial x_*} \right) - \mu \left(\sum_{x_*} \frac{\partial e_i}{\partial x_*} + \sum_{j=1}^m \frac{\partial \Pi}{\partial u_j} \frac{\partial u_j}{\partial x_*} \right) = 0 \quad (4.47)$$

where \sum_{x_*} means that the sum is on all the elements related to shape design variable x_* , and m is the number of the nodal displacement components. Considering Equation (4.42) the term $\frac{\partial \Pi}{\partial u_j}$ vanishes and Equation (4.47) may be written as

$$\rho t \left(\sum_{x_*} \frac{\partial A_i}{\partial x_*} \right) - \mu \left(\sum_{x_*} \frac{\partial e_i}{\partial x_*} \right) = 0 \quad (4.48)$$

or

$$\rho t \left(\sum_{x_*} \frac{\partial A_i}{\partial x_*} \right) - \mu \left(\sum_{x_*} \frac{\partial e_i}{\partial A_i} \frac{\partial A_i}{\partial x_*} \right) = 0 \quad (4.49)$$

Since the strain energy of a flat shell element is in proportion to the element area, $\partial e_i / \partial A_i = e_i / A_i$. Thus

$$\sum_{x_*} \left(\rho t - \mu \frac{e_i}{A_i} \right) \left(\frac{\partial A_i}{\partial x_*} \right) = 0 \quad (4.50)$$

or

$$\sum_{x_*} \left(1 - \mu \frac{e_i}{\rho t A_i} \right) \left(\frac{\partial A_i}{\partial x_*} \right) = 0 \quad (4.51)$$

Defining the strain energy density as $\hat{e}_i = e_i / (\rho t A_i)$, we have

$$\sum_{x_*} (1 - \mu \hat{e}_i) \left(\frac{\partial A_i}{\partial x_*} \right) = 0 \quad (4.52)$$

Similar to the previous case, considering the fact that the final optimum shape should be independent of how a geometry design variable is defined, the only possible way to satisfy this equation is

$$(1 - \mu \hat{e}_i) = 0|_{x_*} \Rightarrow (1 - \mu \hat{e}_i)|_{x_*} \quad (4.53)$$

where $|_{x_*}$ means that the equation is valid for all elements affected by the shape design variable x_* . Equation (4.53) may be rewritten in the form of $\rho t A_i = \mu e_i$, and then it may be applied to all elements connected to x_* :

$$\begin{aligned}\rho t A_1 &= \mu e_1 \\ \rho t A_2 &= \mu e_2 \\ &\dots \\ \rho t A_k &= \mu e_k\end{aligned}\tag{4.54}$$

where k is the number of elements affected by the variable x_* . Summing both sides we have

$$\rho t \sum_{x_*} A_i = \mu \sum_{x_*} e_i\tag{4.55}$$

or

$$1 = \mu \frac{\sum_{x_*} e_i}{\rho t \sum_{x_*} A_i}\tag{4.56}$$

and again \sum_{x_*} means that the sum is on all the elements related to shape design variable x_* . This equation is what we already called “Uniform Average Strain Energy Density” or UASED criterion. Applying similar steps for Equation (4.45), we have

$$\rho \left(\sum_{i=1}^N A_i \right) - \mu \left(\sum_{i=1}^N \frac{\partial e_i}{\partial t} \right) = 0\tag{4.57}$$

Considering Equation (4.53) and substituting $\mu = 1/\hat{e}_i = \rho t A_i/e_i$ into Equation (4.57), we have the following criterion for all possible optimum solutions:

$$\sum_{i=1}^N \left(\rho A_i - \frac{\rho t A_i}{e_i} \cdot \frac{\partial e_i}{\partial t} \right) = 0\tag{4.58}$$

or

$$\sum_{i=1}^N \rho A_i \left[1 - \left(\frac{\partial e_i}{\partial t} \right) / \left(\frac{e_i}{t} \right) \right] = 0\tag{4.59}$$

In case of pure membrane behavior, strain energy is provided by only the membrane stiffness, thus e_i is in proportion to t and $(\partial e_i/\partial t)$ is equal to (e_i/t) . In any other

case $(\partial e_i / \partial t)$ is always greater than (e_i / t) because of the t^2 and t^3 terms associated with the membrane-bending coupling and pure bending behavior, respectively. So in general case, $(\partial e_i / \partial t)$ is always equal or greater than (e_i / t) and all the terms in the sum in Equation (4.59) are negative or zero. Thus the only possible solution for Equation (4.59) is

$$\frac{\partial e_i}{\partial t} = \frac{e_i}{t} \quad (4.60)$$

which states that at the optimum point, all the strain energy is provided by the membrane mode. In other words:

$$\frac{e_{ib}}{e_i} \rightarrow 0 \quad (4.61)$$

where e_{ib} is the strain energy provided by bending and membrane-bending coupling effects. This relation may also be extended to the whole structure:

$$\frac{\text{Total bending strain energy}}{\text{Total strain energy}} = \frac{\Sigma e_{ib}}{\Sigma e_i} \rightarrow 0 \quad (4.62)$$

This relation (hereinafter called “Least Bending Energy Ratio” or LBER criterion) states that among all optimum designs with different thicknesses and shapes, the one which has the least bending energy ratio has the minimum mass. Equations (4.56) and (4.62) should be iteratively satisfied in order to minimize the total mass of a shell structure. Similar to Equation (4.33), the following recurrence equation may be used to iteratively satisfy Equation (4.56):

$$(x_*)_{\eta+1} = (x_*)_{\eta} \cdot \left(\frac{\sum_{i=1}^{N_e} \hat{e}_i}{\sum_{i=1}^{N_e} \hat{e}_i^2} \cdot \frac{\sum_{x_*} e_i}{\rho t \sum_{x_*} A_i} \right)^{1/r} \quad (4.63)$$

In the case that the system stability is the optimization constraint, the solution after each iteration should be scaled so that the limit load of the structure is equal

to or greater than the applied load. The same procedure is done for the case of displacement constraint to limit the nodal displacement to a maximum allowable value. Here, we scale the design by changing the general thickness of the shell, and Equation (4.62) is used to guarantee that change of the thickness is in the proper direction towards the optimal design. Obviously if the overall thickness of the structure is not considered as a design variable, this optimality criterion is relaxed and scaling is done by changing shape design variables. Obviously if the limit load is greater than the applied load, the thickness should be reduced and vice versa. As for displacement constraint, if the maximum displacement is greater than the allowable displacement, the thickness should be increased and vice versa.

It should be noted that the strain energy is not a linear function of the thickness, and as a result, scaling the thickness of the shell by a scale factor has not the effect of scaling the limit load by the same scale factor. In other words, by changing the thickness of the shell, the displacement pattern also changes and a simple proportional reduction or increase of the thickness would not lead to the desired critical load. Selecting the new thickness is usually done through an iterative process. However, this process is not highly iterative since the new thickness is usually selected among a set of available thicknesses, and this process converges after few iterations.

4.7 Thickness optimization of a plate and its application in optimum design of stiffened panels

In this section thickness optimization of a plate (or shell) modeled by N facet elements is investigated. In this study, the thickness of each element in the finite element

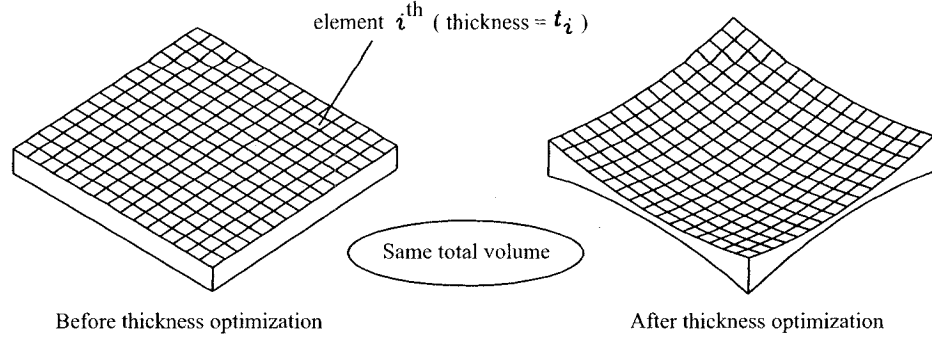


Figure 4.5: Concept of thickness optimization subject to constant volume.

mesh is considered as a design variable, and optimum thickness t_i ($i = 1, \dots, N$) for each element is found in order to maximize the critical load (or load capacity) factor λ_c subject to constant total volume of the plate (i.e. $V = V_0$ where V is the total volume of the material – see Figure 4.5). Load factor λ_c is found with respect to displacement, stress, or stability constraint. Based on the UASEV criterion for thickness optimization, it can be concluded that for the optimum shape, the following value should be the same for all elements:

$$\tilde{e}_i = \frac{1}{A_i} \frac{\partial e_i}{\partial t_i} = \frac{1}{2 A_i} \int_{A_i} \left(\{\varepsilon_m\}^T \cdot \frac{A_i^e}{t_i} \cdot \{\varepsilon_m\} + \{\varepsilon_b\}^T \cdot \frac{3D_i^e}{t_i} \cdot \{\varepsilon_b\} \right) dA_i \quad (4.64)$$

As mentioned before, one can easily see that \tilde{e}_i computed by Equation (4.64) in general case of the combination of membrane and bending deformations, is different from the strain energy density, which is usually defined as $e_i/(t_i A_i)$:

$$\bar{e}_i = \frac{e_i}{t_i A_i} = \frac{1}{2 A_i} \int_{A_i} \left(\{\varepsilon_m\}^T \cdot \frac{A_i^e}{t_i} \cdot \{\varepsilon_m\} + \{\varepsilon_b\}^T \cdot \frac{D_i^e}{t_i} \cdot \{\varepsilon_b\} \right) dA_i \quad (4.65)$$

As a result, thickness optimization of plates and shells using uniform strain energy density criterion with the values computed by Equation (4.65) in general case of the combination of membrane and bending deformations is unjustified. However in case of pure membrane strain energy (i.e. $\{\varepsilon_b\} = 0$), using uniform strain energy density

criterion (USED) instead of UASEV leads to the same result (because in this case, Equations (4.64) and (4.65) are equivalent). Also, in case of the pure bending strain energy (i.e. $\{\varepsilon_m\} = 0$) results are again the same since based on Equations (4.64) and (4.65), uniform distribution of $\bar{\varepsilon}_i$ and uniform distribution of $\tilde{\varepsilon}_i$ in case of $\{\varepsilon_m\} = 0$ are equivalent by a scale factor 3.

The recurrence relation mentioned in section 4.5.2 is used in order to optimize the thickness of each element iteratively. In order to keep the total volume equal to constant V_0 , after each iteration, all t_i are scaled by a scale factor β :

$$\beta = \frac{V_0}{V} = \frac{V_0}{\sum_{i=1}^N t_i A_i} \quad (4.66)$$

Considering element thicknesses as the design variables is not the only possible approach in thickness optimization. One may instead, consider nodal thicknesses as the design variables, which has the advantage of leading to a smooth thickness profile. However in that case, the related equations are more complicated, since each design variable is connected to more than one element.

In this study, the optimal shape after performing the thickness optimization is smoothed by passing to nodal thicknesses. The thickness of the plate at each node is found by taking the average of the thicknesses of all elements connected to that node. Then, a smooth thickness profile is created by linear interpolation using nodal thicknesses.

Thickness optimization of plates, can be used to identify the potential places for adding stiffeners. To do so, first thickness optimization is performed, then regions where elements have higher thickness values are identified as potential rib locations. Finally, stiffeners with variable height according to the results found in the first step,

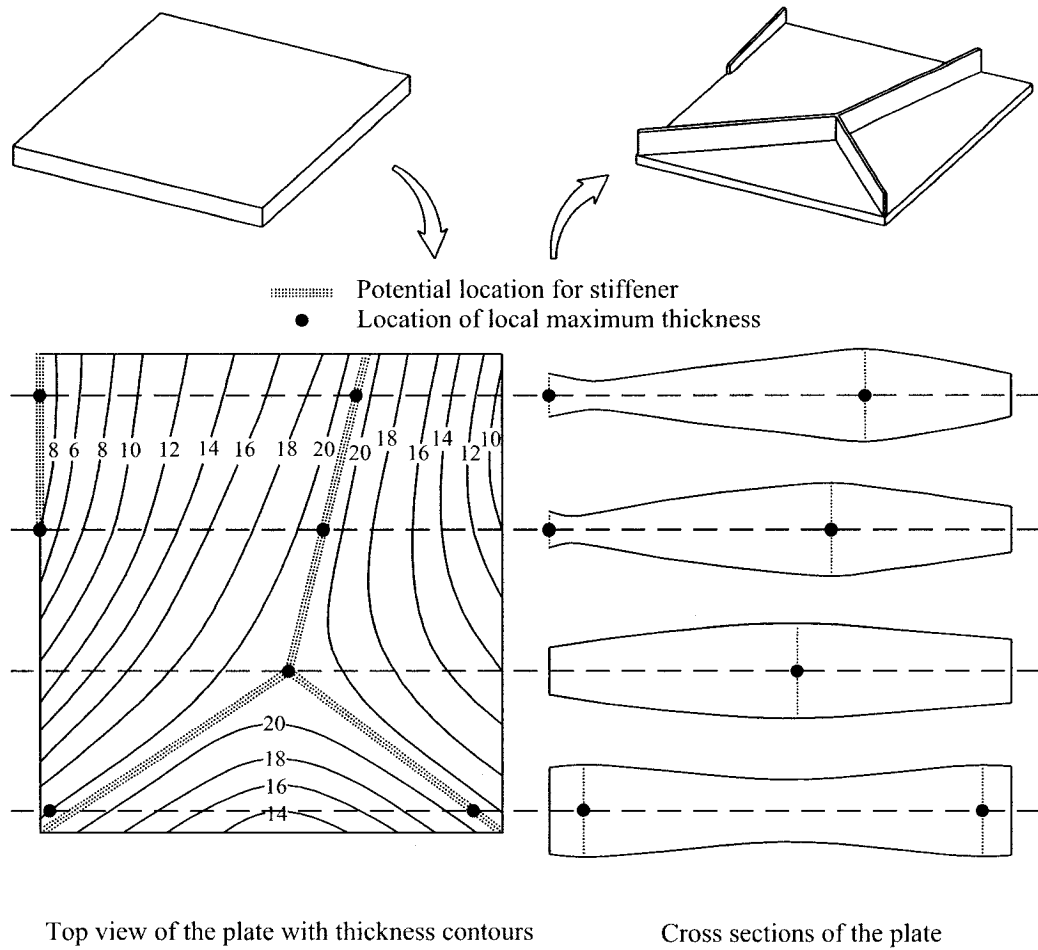


Figure 4.6: Identifying potential locations for stiffeners using thickness optimization.

are added to the plate with constant thickness. Height of the ribs vary proportional to the obtained thickness distribution, but not more than a maximum value considered in the design constraint. Thickness of the plate and stiffeners are found such that the constant volume constraint is satisfied. The whole process may be repeated to find additional stiffeners.

As an example, Figure 4.6 shows how the potential locations for adding the stiffeners are found for a simple plate. Variation of the thickness after performing the thickness optimization is shown by thickness contours. Considering the cross sections of the plate at different locations, one can identify the locations of the local maximum

thickness at each section. The lines which connect these points of local maximum thickness are called the “lines of maximum thickness”, and are selected as the potential locations for stiffeners. Any design constraint or limitation is also considered in locating the stiffeners. The locations and the directions of the sections are arbitrary, and usually they are selected by the designer in a way to perform the design with the least number of sections. Obviously, the final design may not be completely unique, and will somehow depend on the designer’s point of view.

This method is similar to the one used by Stok and Mihelic [142], and Lam and Santhikumar [145], except that in their studies “Uniform Strain Energy Density” (USED) criterion was used instead of UASEV. As mentioned before, it is important to note that using USED criterion instead of UASEV in general case of the combination of membrane and bending deformations is unjustified and generates erroneous results, and only in case of pure membrane or pure bending behavior the results are the same.

In topology optimization the checker board pattern, which is an unnatural result with artificially high stiffness may frequently happen [153, 154]. Several techniques have been proposed to avoid the checker board pattern as an optimal solution [155, 156, 157]. In this study we use a simple procedure similar to the one used by Gáspár et al. [158], in which a primary meshing is subdivided into further finite elements called secondary elements. Here, first a primary mesh is considered with square elements and then each square in the primary mesh is divided into two triangular elements. The new thickness of each square in the primary mesh (after each iteration) is found by taking the average of the new thicknesses of its two triangular elements.

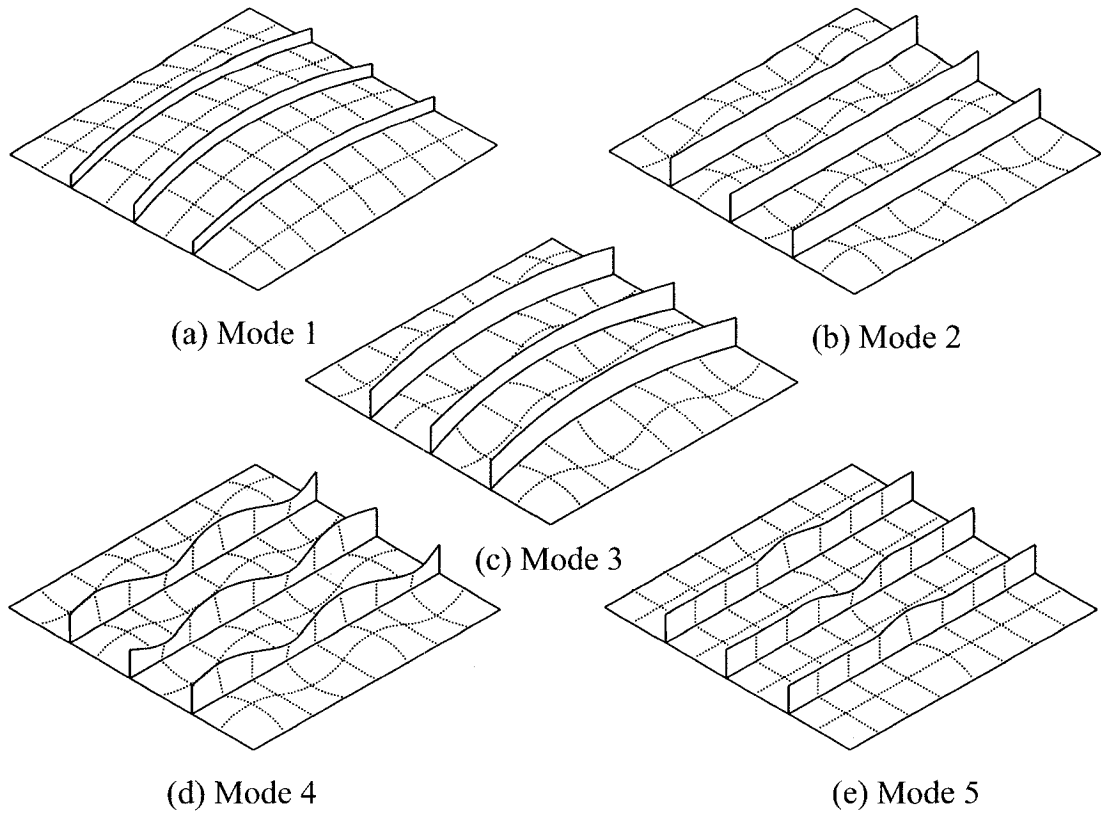


Figure 4.7: Primary buckling modes of a stiffened panel subject to compressive loads [159].

4.8 Shape optimization of stiffened panels considering local buckling

In this section the shape optimization methodology is modified to consider the effect of local buckling in stiffened panels. First, buckling modes in stiffened panels are briefly investigated, and then a method is presented to modify the optimization solution strategy to consider the local buckling in stiffened panels.

4.8.1 Buckling modes of stiffened panels

Figure 4.7 shows the buckling modes of a typical stiffened panel. According to Ref. [159], the primary failure modes for a stiffened panel subject to compressive loads are

categorized into the following six groups:

Mode 1: Overall (global) buckling of the plate and stiffeners- Figure 4.7(a). This mode typically happens when the stiffeners are relatively weak, and as a result they buckle together with the plate.

Mode 2: Local buckling of the plate between the stiffeners- Figure 4.7(b). In this mode the panel collapses due to the local buckling and consequently yielding of the plate between the stiffeners.

Mode 3: Beam-column type buckling of the combination of stiffener and effective plate- Figure 4.7(c). In this mode the failure happens by beam-column type collapse of the combination of stiffener and the associated effective (reduced) plate.

Mode 4: Local buckling of the stiffener web- Figure 4.7(d). This mode is usually called a “Stiffener-induced failure”.

Mode 5: Lateral-torsional buckling of the stiffener web- Figure 4.7(e). This mode is similar to mode 4 except that buckling of the stiffener is a lateral-torsional (tripping) buckling.

Modes 4 and 5 typically happen when the height to thickness ratio of the stiffener web is too large and/or when the stiffener flange (e.g. in “Z” stiffeners) is inadequate to keep it straight.

Mode 6: Entire yielding of the panel cross section. This mode usually happens when the panel slenderness is very small or when the panel is subjected to the tensile load. In this case the panel cross section yields entirely, without any local or overall buckling.

Most studies consider only one or two forms of buckling (buckling modes) since

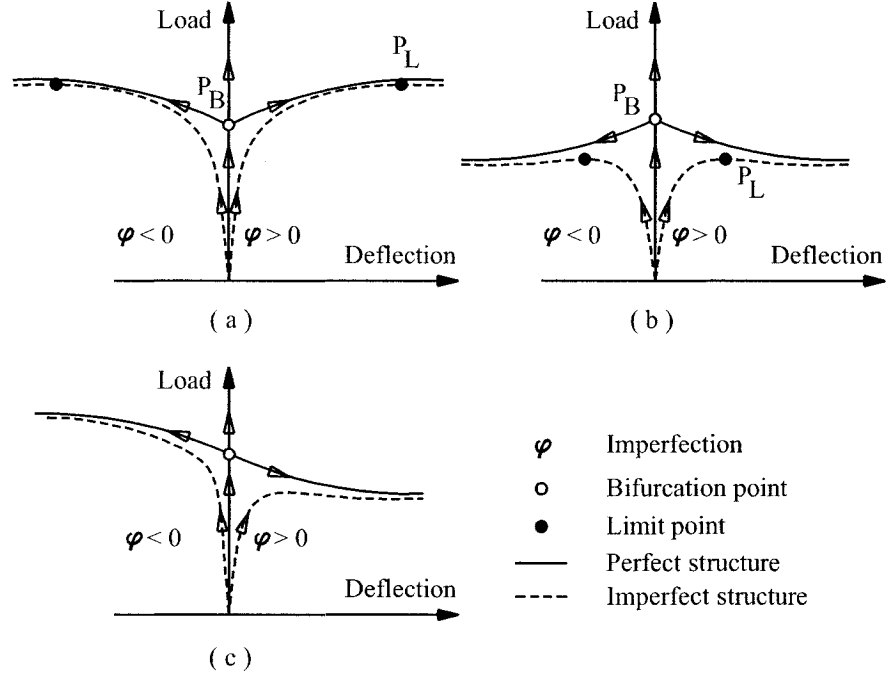


Figure 4.8: Behavior of the perfect and imperfect stiffened panels.

considering all possible mode shapes in nonlinear analysis of stiffened panels (particularly during the iterative process of optimization) is a complex and time-consuming task. In this study, before performing each nonlinear analysis, the buckling mode corresponding to the lowest buckling load is found using a linear eigenvalue analysis, and then an imperfection similar to that mode shape is considered in the nonlinear analysis of the stiffened panel. This procedure along with optimization methodology is explained in the next section.

4.8.2 Bifurcation buckling and modification of the optimization algorithm

Figure 4.8 shows the behavior of the perfect and imperfect stiffened panels, under axial loads. In a perfect structure, the equilibrium path reaches to a bifurcation point and follows the second branch as the nonlinear post-buckling deformations. In case

that the structure is not perfect, the equilibrium path falls below that curve with a margin depending on the amount of imperfection.

Two forms of the bifurcation points are usually observed in equilibrium paths. First type which has been depicted in Figure 4.8(a,b) is called symmetric bifurcation, in which the behavior or strength of the structure does not depend on the direction of imperfection. In this case (which usually happens in buckling modes 2, 4, and 5) a small imperfection similar to the buckling mode (with either positive or negative sign) leads to the correct result for the imperfect structure. The second form of the bifurcation point is usually observed in global buckling (and also mode 3), where the direction of the global bending makes difference in the behavior, and consequently strength of the structure, as shown in Figure 4.8(c). In this case, usually two analysis are necessary for the imperfect structure, with small imperfections in the positive and negative directions.

Figure 4.9(a) shows a typical algorithm for optimization of structures with geometric nonlinearity. The optimization process usually starts with nonlinear analysis of an initial design. In the next step, optimization is performed and design variables are modified, leading to a new design. The whole process is repeated until convergence is achieved. As mentioned before, this algorithm is very time consuming, since an iterative process (nonlinear finite element analysis) has to be performed inside another iterative process (nonlinear optimization problem). Obviously performing nonlinear finite element analysis (NFEA) for all the possible buckling modes (during each optimization iteration) makes the complex task of optimization even more complex and practically impossible to perform. As a result, a criterion should be

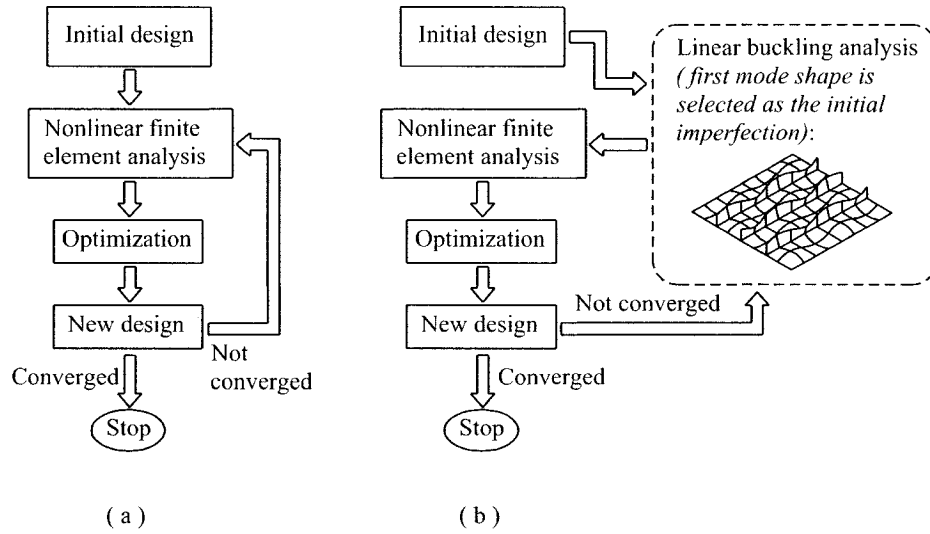


Figure 4.9: Algorithms for optimization of nonlinear structures.

employed to efficiently find the appropriate buckling mode and select that as the imperfection shape before each NFEA.

Figure 4.9(b) shows how the optimization algorithm can be modified to consider the effect of initial imperfections and buckling modes. Before each NFEA, a linear eigenvalue analysis is performed and linear buckling mode shapes of the perfect structure are found. Then, a small imperfection similar to the buckling mode shape corresponding to the lowest buckling load (load P_B in Figure 4.8(a,b)) is considered in the NFEA. Performing the NFEA, the critical load of the structure is then considered as $P_{cr} = P_L$ where P_L is the limit load of the imperfect structure. Using this methodology, NFEA is performed only for the first buckling mode in each iteration of the optimization process, and also mode switching due to the change of the shape (during the optimization process) can be captured.

It should be mentioned that if stress or displacement constraint is also considered in the optimization process, the critical load should be reduced to the load corre-

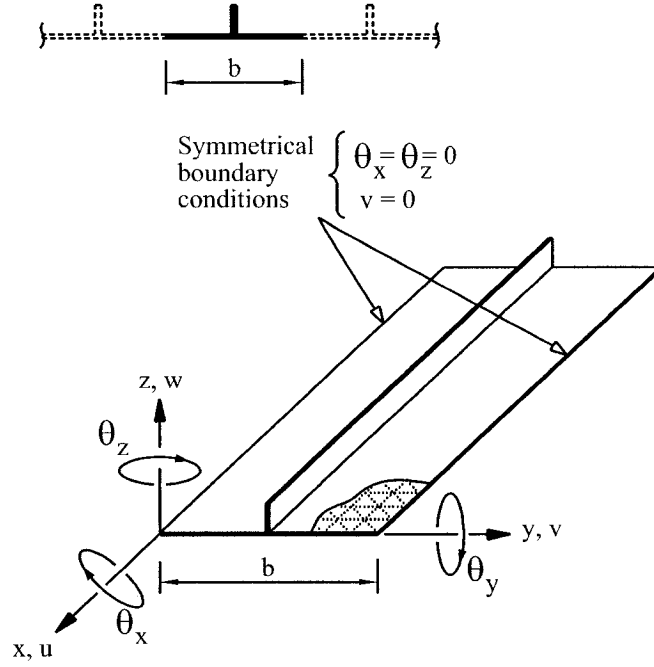


Figure 4.10: Discretized panel module used in finite element analysis.

sponding the allowable stress or displacement, if that constraint becomes active prior the stability constraint.

In order to simplify the process, instead of the whole structure a single module of the stiffened panel with appropriate boundary conditions is considered (Figure 4.10). This model has already been used in Ref. [160], and has been proven to be accurate enough. Buckling mode shapes of the single module are found by performing the following familiar eigenvalue analysis:

$$([K] + \lambda_i [K_\sigma]) \vartheta_i = 0 \quad (4.67)$$

where $[K]$ and $[K_\sigma]$ are the stiffness and stress stiffness matrixes in the global coordinate system, respectively, and ϑ_i represents the i^{th} buckling mode shape. The ϑ_i corresponding to the smallest λ_i is the first buckling mode, and is selected as the initial imperfection in NFEA.

Chapter 5

Numerical Examples

A set of problems on geometrically nonlinear static analysis, and shape optimization of thin-walled structures were solved in order to demonstrate the accuracy of the proposed flat shell element, and developed optimization methodologies. The results presented in this chapter are categorized in different sections, and are compared with those available in the literature using other elements, analyses, or design optimization techniques.

5.1 Validation of the proposed shell element for thin-walled structures

In this section some of the popularly employed geometric nonlinear benchmark problems are selected to evaluate the accuracy of the new shell element for thin-walled structures. The corotational approach with Newton-Raphson technique along with the load control method and convergence criterion based on incremental displacement (with $\varepsilon_d = 10^{-4}$) is used for these examples. In each example, load steps are depicted on the load-displacement path.

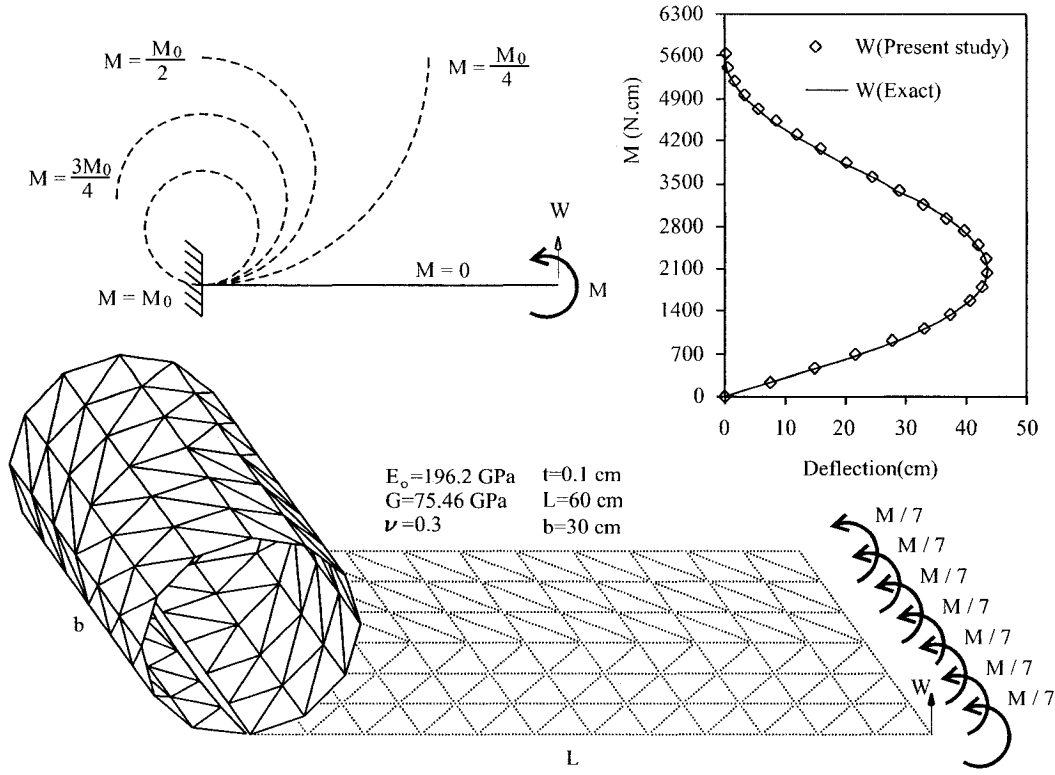


Figure 5.1: Cantilever plate subjected to end moment

5.1.1 Cantilever plate subjected to end moment

A cantilever plate with length $L = 60$ cm, width $b = 30$ cm, and thickness $t = 0.1$ cm made of an isotropic material and subjected to an end moment is considered (Figure 5.1). Due to the applied end moment M , the cantilever forms a circular arc with radius R equal to $E_o I / M(1 - \nu^2)$ and central angle θ equal to $\frac{L}{R}$. Thus, one can show that the transverse tip deflection can be computed by the following analytical formula:

$$W = R(1 - \cos\theta) = \frac{E_o I}{M(1 - \nu^2)} \left(1 - \cos \frac{ML(1 - \nu^2)}{E_o I}\right) \quad (5.1)$$

The plate is modeled by 144 triangular flat shell elements (developed in this study)

and the end moment $M = 5644.5 \text{ N.cm}$ is applied in 25 equal steps. Figure 5.1 plots the transverse tip deflection W against the end moment M . Analysis is done by total number of 147 iterations (almost 6 iterations per load step). As it can be realized, the result is in complete agreement with the analytical solution.

5.1.2 Elastica problem

Figure 5.2 shows a cantilever plate with length $L = 10 \text{ cm}$, width $b = 1 \text{ cm}$, and thickness $t = 0.1 \text{ cm}$ subjected to axial compression force at its free end. This problem which is one of the earliest examples of post buckling analysis, has been investigated in detail in Ref. [161]. The problem was originally investigated for columns, but it can be used to evaluate the developed shell element as well. The contribution of Poisson's ratio is neglected by considering $\nu = 0$. The analytical linear buckling load is $F_{cr} = \frac{\pi^2 E_o I}{4L^2} = 40.3416 \text{ N}$. Linear buckling analysis using the proposed shell element also gives almost the same value $F_{cr} = 40.3544 \text{ N}$.

Considering any value for the angle α and neglecting the axial deformation, the following expressions have been derived [161] to find the tip coordinates, X_A , Y_A versus applied force P :

$$\begin{aligned} L &= \frac{1}{k} \int_0^{\pi/2} \frac{d\phi}{\sqrt{1 - \tilde{P}^2 \sin^2 \phi}} \\ X_A &= \left(\frac{2}{k} \int_0^{\pi/2} \sqrt{1 - \tilde{P}^2 \sin^2 \phi} \cdot d\phi \right) - L \\ Y_A &= \frac{2\tilde{P}}{k} \end{aligned} \tag{5.2}$$

where $\tilde{P} = \sin(\frac{\alpha}{2})$ and $k^2 = \frac{P}{E_o I}$.

To evaluate the new shell element in nonlinear analysis, the cantilever plate is

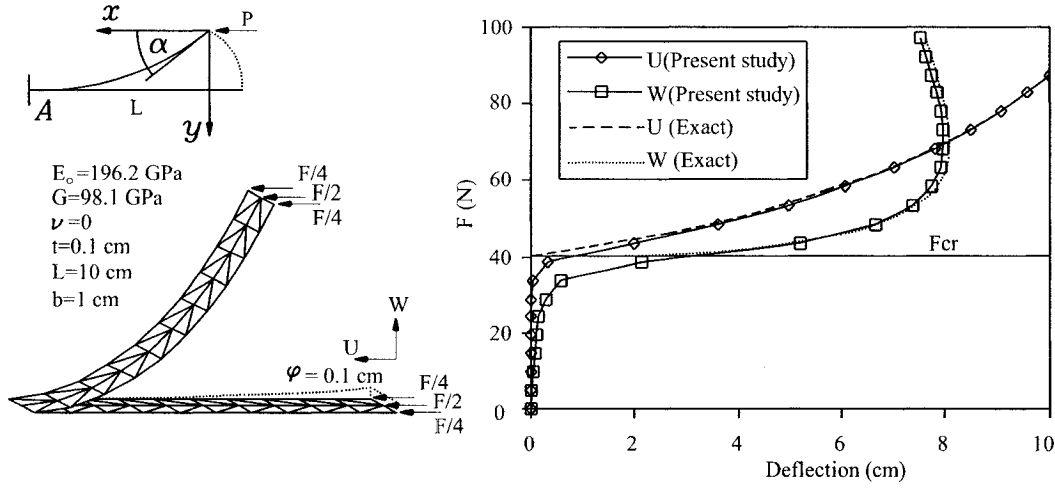


Figure 5.2: Elastica problem

modeled using 40 triangular elements, and $10\text{ Kgf} = 98.1\text{ N}$ axial force is applied in 20 equal steps. Since the plate is initially completely flat, it is necessary to consider a very small imperfection to start the lateral deflection. Figure 5.2 shows the deflections at the tip against the applied load, when a quadratic imperfection with the maximum value of 0.1 cm at the tip is considered. Analysis is performed by total number of 135 iterations (almost 7 iterations per load step). The difference between the analytical solution and the results based on the proposed shell element is very small. It should be noted that the nonlinear response is dependent on the amount of imperfection particularly for pre-buckling part of the graph.

5.1.3 Cantilever plate subjected to end shear force

Figure 5.3 shows a cantilever plate with dimensions similar to those of the one in the Elastica problem (section 5.1.2) but with different material properties, subjected to the end shear force. Similar to the Elastica problem, it is possible to derive an

expression for the tip deflections at any load level, neglecting the axial deformation:

$$E_o I \frac{d\phi}{ds} = M = -Px \quad (5.3)$$

Differentiating both sides with respect to s yields

$$E_o I \frac{d^2\phi}{ds^2} = -P \cos\phi \quad (5.4)$$

or

$$\frac{d^2\phi}{ds^2} = -k^2 \cos\phi \quad (5.5)$$

where $k^2 = \frac{P}{E_o I}$. Now, integrating both sides of Equation (5.5) with respect to ϕ , we have

$$\int \frac{d^2\phi}{ds^2} \cdot d\phi = -k^2 \int \cos\phi \cdot d\phi \quad (5.6)$$

or

$$\int \frac{d^2\phi}{ds^2} \cdot \frac{d\phi}{ds} \cdot ds = -k^2 \int \cos\phi \cdot d\phi \quad (5.7)$$

Thus

$$\frac{1}{2} \int \frac{d}{ds} \left(\frac{d\phi}{ds} \right)^2 \cdot ds = -k^2 \int \cos\phi \cdot d\phi \quad (5.8)$$

or

$$\frac{1}{2} \left(\frac{d\phi}{ds} \right)^2 = -k^2 \sin\phi + c \quad (5.9)$$

At $x = 0$ we have $M = 0$, $\frac{d\phi}{ds} = 0$, $\phi = \alpha$ therefore

$$c = k^2 \sin\alpha \quad (5.10)$$

Now, substituting Equation (5.10) into Equation (5.9) yields:

$$\left(\frac{d\phi}{ds} \right)^2 = 2k^2 (\sin\alpha - \sin\phi) \quad (5.11)$$

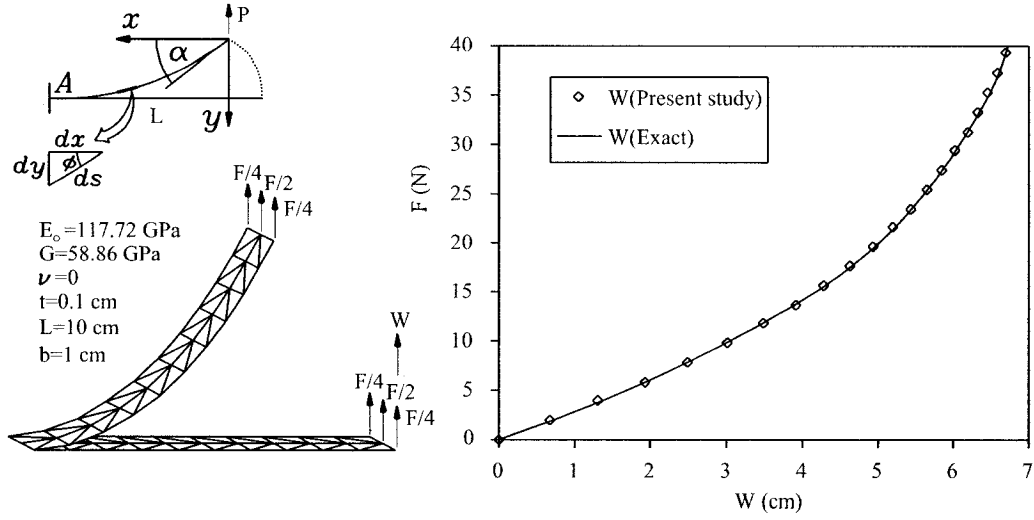


Figure 5.3: Cantilever plate subjected to end shear force

Since $\frac{d\phi}{ds} < 0$, we conclude that

$$ds = \frac{-d\phi}{k\sqrt{2} \cdot \sqrt{\sin\alpha - \sin\phi}} \quad (5.12)$$

Finally

$$\begin{aligned} L &= \int_{\alpha}^0 ds = \int_0^{\alpha} (-ds) = \frac{1}{k\sqrt{2}} \int_0^{\alpha} \frac{d\phi}{\sqrt{\sin\alpha - \sin\phi}} \\ X_A &= \int_{\alpha}^0 dx = \int_{\alpha}^0 ds \cdot \cos\phi = \int_0^{\alpha} (-ds) \cdot \cos\phi = \frac{1}{k\sqrt{2}} \int_0^{\alpha} \frac{\cos\phi d\phi}{\sqrt{\sin\alpha - \sin\phi}} \\ Y_A &= \int_{\alpha}^0 dy = \int_{\alpha}^0 ds \cdot \sin\phi = \int_0^{\alpha} (-ds) \cdot \sin\phi = \frac{1}{k\sqrt{2}} \int_0^{\alpha} \frac{\sin\phi d\phi}{\sqrt{\sin\alpha - \sin\phi}} \end{aligned} \quad (5.13)$$

where $k^2 = \frac{P}{E_o I}$.

For the finite element simulation, the cantilever plate is modeled with 40 shell elements and $4 \text{ Kgf} = 39.24 \text{ N}$ shear force is applied in 20 steps at the tip. Analysis is performed by 104 iterations (almost 5 iterations per load step). The results are shown in Figure 5.3 in which analytical solution is compared with finite element solution based on the developed shell element.

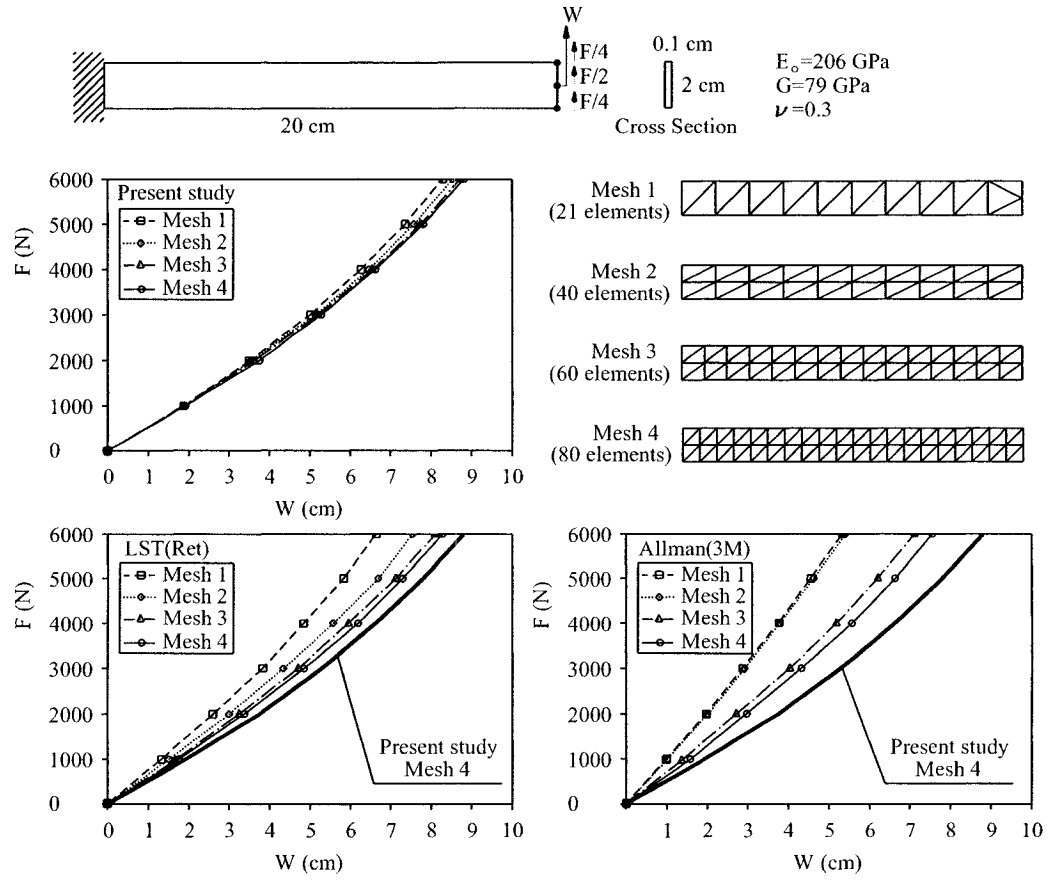


Figure 5.4: Cantilever subjected to end in-plane shear force

5.1.4 Cantilever subjected to end in-plane shear force

In order to compare the response of a structure modeled by different membrane elements, a cantilever beam subjected to end in-plane shear force is considered in Figure 5.4. It should be noted that this example does not fall into the category of “large displacements and rotations–small strains”, but as long as the strains remain in the range of small strains (i.e. less than 5%) it is possible to use the proposed approach. Also material nonlinearity is not considered in this example, which means that we assume only elastic strains. Four different mesh configurations with 21, 40, 60 and 80 elements are used, and load $F = 6000\text{ N}$ is applied in 6 steps at the tip. Nonlinear behaviors of different elements are investigated in pure membrane action. Figure 5.4 shows the tip deflection against the applied load using different membrane elements. It can be realized that different mesh configurations have insignificant effect on the result obtained by the proposed new element. The same analysis using LST(Ret) and Allman(3M) membrane elements shows that by increasing the number of elements, the nonlinear response approaches to the same final result but they converge slower than the proposed element. This example shows the efficiency of the proposed element in geometrical nonlinear problems compared to the other membrane elements.

5.1.5 Cantilever isotropic angle subjected to end shear force

Figure 5.5 shows a cantilever angle subjected to end shear force. The beam is modeled with 160 triangular elements, and load $F = 1200\text{ N}$ is applied in 6 steps at the tip. Tip deflections obtained using the new shell element are compared with those obtained

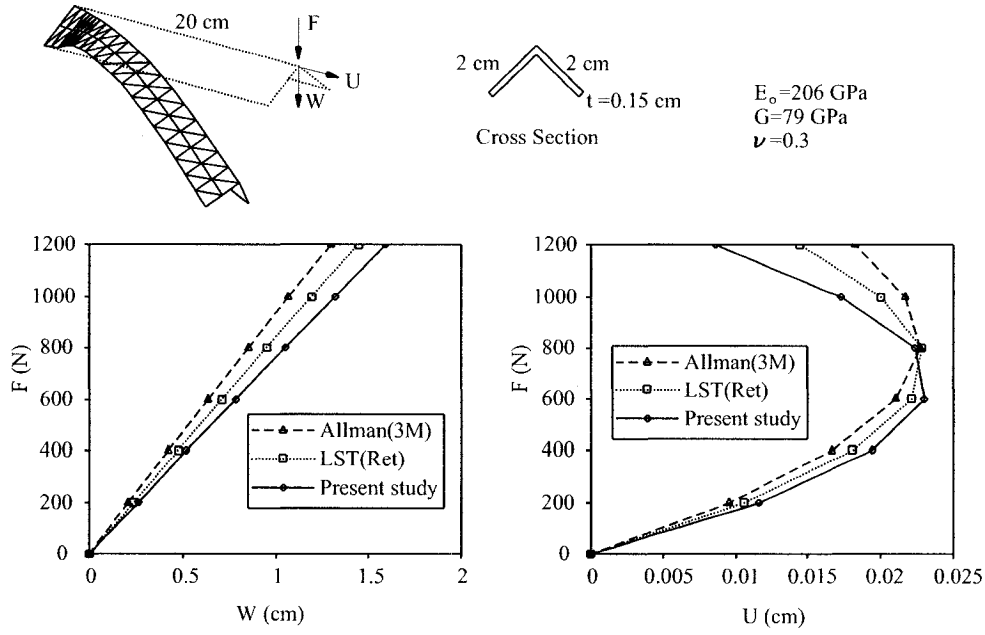


Figure 5.5: Cantilever angle subjected to end shear force

with LST(Ret) and Allman membrane elements combined with DKT plate bending element. It is again observed that the choice of the membrane element affects the response of the structure significantly.

5.1.6 Cantilever stiffened plate subjected to end shear force

Figure 5.6 shows a cantilever stiffened plate subjected to end shear. The structure is modeled with 320 triangular elements, and load $F = 2400$ N is applied in 6 steps at the tip. The result obtained by the new shell element is compared with the one obtained using DKT element combined with the Allman(3M) and LST(Ret) membrane elements. In all the cases the same imperfection is considered in the form of a half sine wave with the maximum value of 1 mm at the middle of the free edges of the stiffeners. Since most of the bending resistance is provided by the membrane

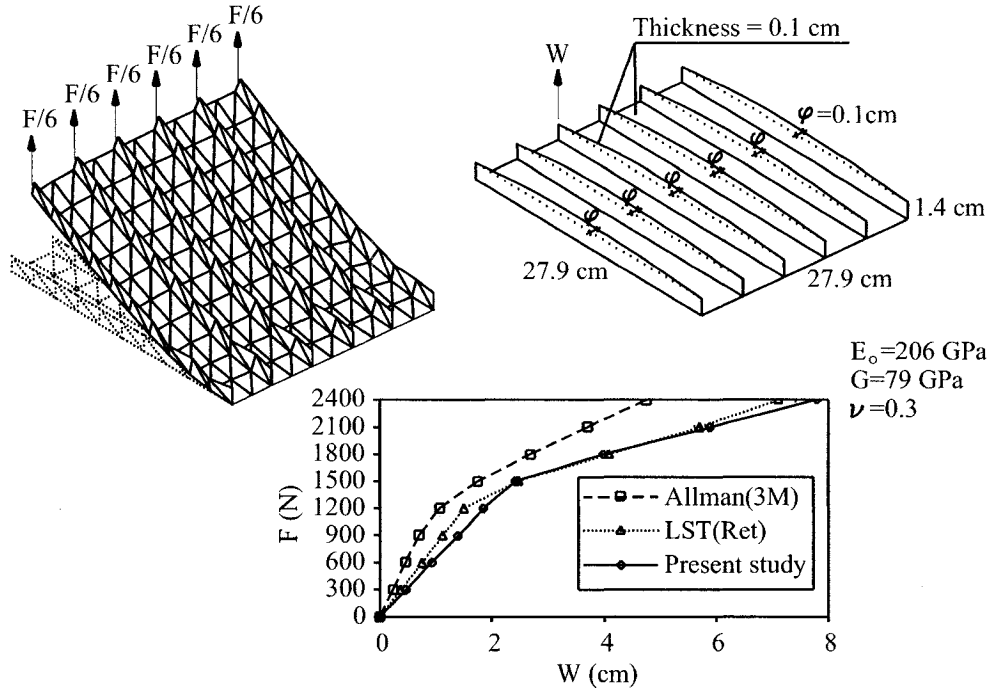


Figure 5.6: Cantilever stiffened plate subjected to end shear force

action in the stiffener plates, the choice of the membrane element can affect the results significantly. It is observed that use of Allman element leads to significant errors in the computed response of the structure. The error is less in the case of LST(Ret).

5.2 Validation of the proposed shell element for thick structures

In this section, some example structures with geometric nonlinearity are analyzed using the proposed element for thick structures, and the results are compared with those obtained using Allman(3M) and LST(Ret) membrane elements combined with the same DKMT plate bending element. To trace the complete load-displacement curve in the following examples, corotational approach with Newton-Raphson technique combined with the arc length method [162, 163] and convergence criterion on

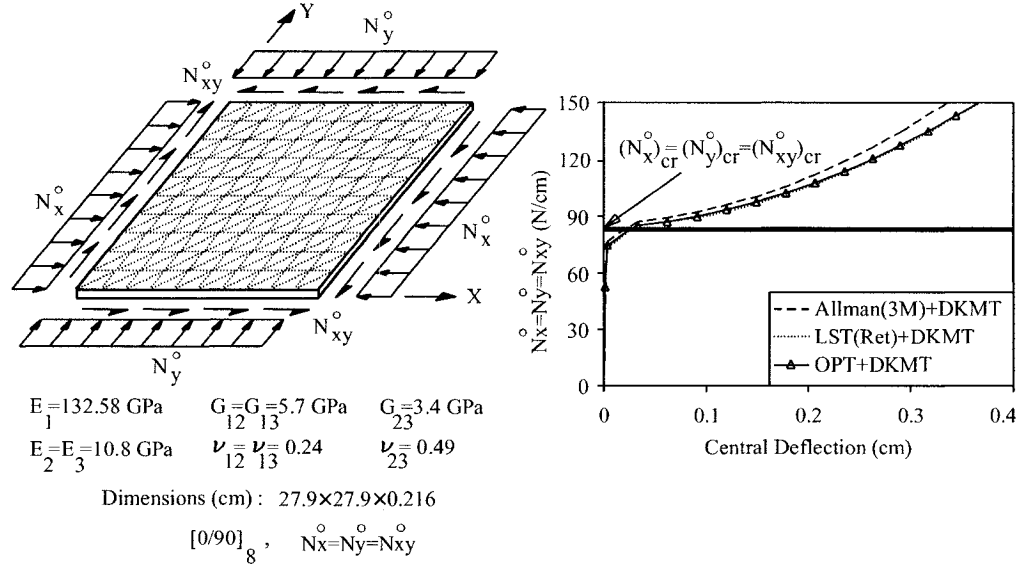


Figure 5.7: Response of the square unsymmetric $[0/90]_8$ laminate subjected to shear and biaxial compression.

incremental displacement is used. In each example, load steps are depicted on the load–displacement path. Fiber angles in composite laminates are measured from the x axis shown in the figures.

5.2.1 Square unsymmetric laminate with simple supports subjected to shear and biaxial compression

Figure 5.7 shows a simply supported unsymmetric laminate $[0/90]_8$, under in-plane loading $N_x^o = N_y^o = N_{xy}^o$. The dimensions of the laminate are $27.9 \text{ cm} \times 27.9 \text{ cm} \times 0.216 \text{ cm}$ and it is made of 16 layers of graphite-epoxy material with the following mechanical properties:

$$E_1 = 132.58 \text{ GPa} , E_2 = 10.8 \text{ GPa} , G_{12} = G_{13} = 5.7 \text{ GPa} ,$$

$$G_{23} = 3.4 \text{ GPa} , \nu_{12} = \nu_{13} = 0.24 , \nu_{23} = 0.49$$

The plate is modeled by 200 triangular elements, and X displacements along the edge ($x = 0$) and Y displacements along the edge ($y = 0$) are constrained. The other

two edges are free to move in the x and y directions. Z displacement along all the four edges is constrained. The linear buckling analysis with the proposed shell element gives the value $(N_x^o = N_y^o = N_{xy}^o)_{cr} = 83.28 \text{ N/cm}$ for the critical buckling load.

Using corotational approach and proposed thick shell element, the nonlinear analysis is performed and the load–deflection path is found for this plate. Due to the coupling effect between membrane and bending modes, this unsymmetric laminate deforms in-plane and out-of-plane simultaneously and no imperfection is needed to start the lateral deformation. The variation of the central deflection against the applied loads is plotted and compared with those obtained using LST(Ret) and Allman(3M) membrane elements combined with DKMT plate bending element. It is observed that in the pre–buckling part of the nonlinear curve, there is no significant difference between the results obtained by different membrane elements combined with DKMT. However, in the post–buckling part of the response, where membrane forces are larger, the result found by Allman(3M) combined with DKMT becomes less accurate.

For this example, results of the analysis using the proposed thin shell element are found to be the same as those shown in Figure 5.7, which indicates that in this case, DKMT coincides with DKT due to negligible effect of shear deformation.

5.2.2 Cantilever laminated angle subjected to end shear force

Figure 5.8 shows a cantilever angle subjected to end shear force F . The beam is made of $[(0/90)_4]_s$ composite laminate with mechanical properties similar to those in the previous example (section 5.2.1). Tip deflections obtained using the proposed thick

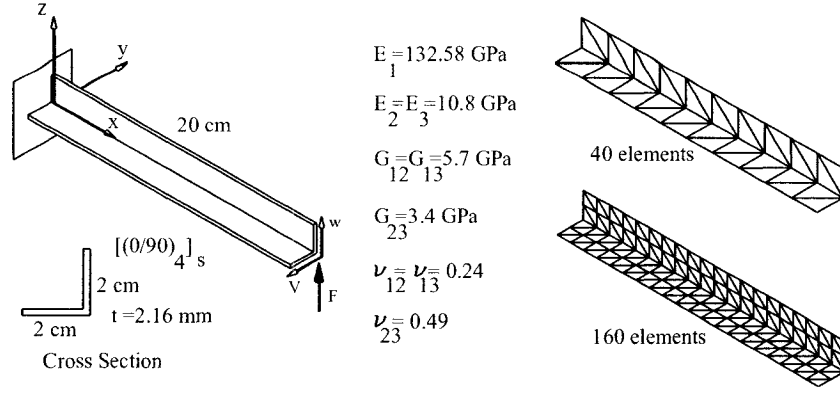


Figure 5.8: Cantilever laminated angle subjected to end shear force.

shell element are compared with those obtained using LST(Ret) and Allman(3M) membrane elements combined with DKMT. Two different meshes with 40 and 160 elements are considered in the analysis and results are shown in Figure 5.9 for each mesh. It is observed that the choice of the membrane element has a significant effect on the response of this structure. Interestingly, the results found by the proposed element are very close for two different meshes, and other elements lead to almost the same result when a fine mesh is used. It is concluded that the result found by the proposed element when a coarse mesh is used is the most reliable one. It should be mentioned that in this case as well, using DKT instead of DKMT leads to the same results due to negligible effect of shear deformation.

5.2.3 Thick cantilever beam subjected to end shear force

A thick beam with length $L = 20$ cm, thickness $h = 4$ cm and width $b = 0.1$ cm is considered under the tip load F . The beam is modeled with 160 optimal membrane elements (OPT), as shown in Figure 5.10, case(I). In order to eliminate the effect of mesh orientation, two different meshes are considered. A similar beam with the

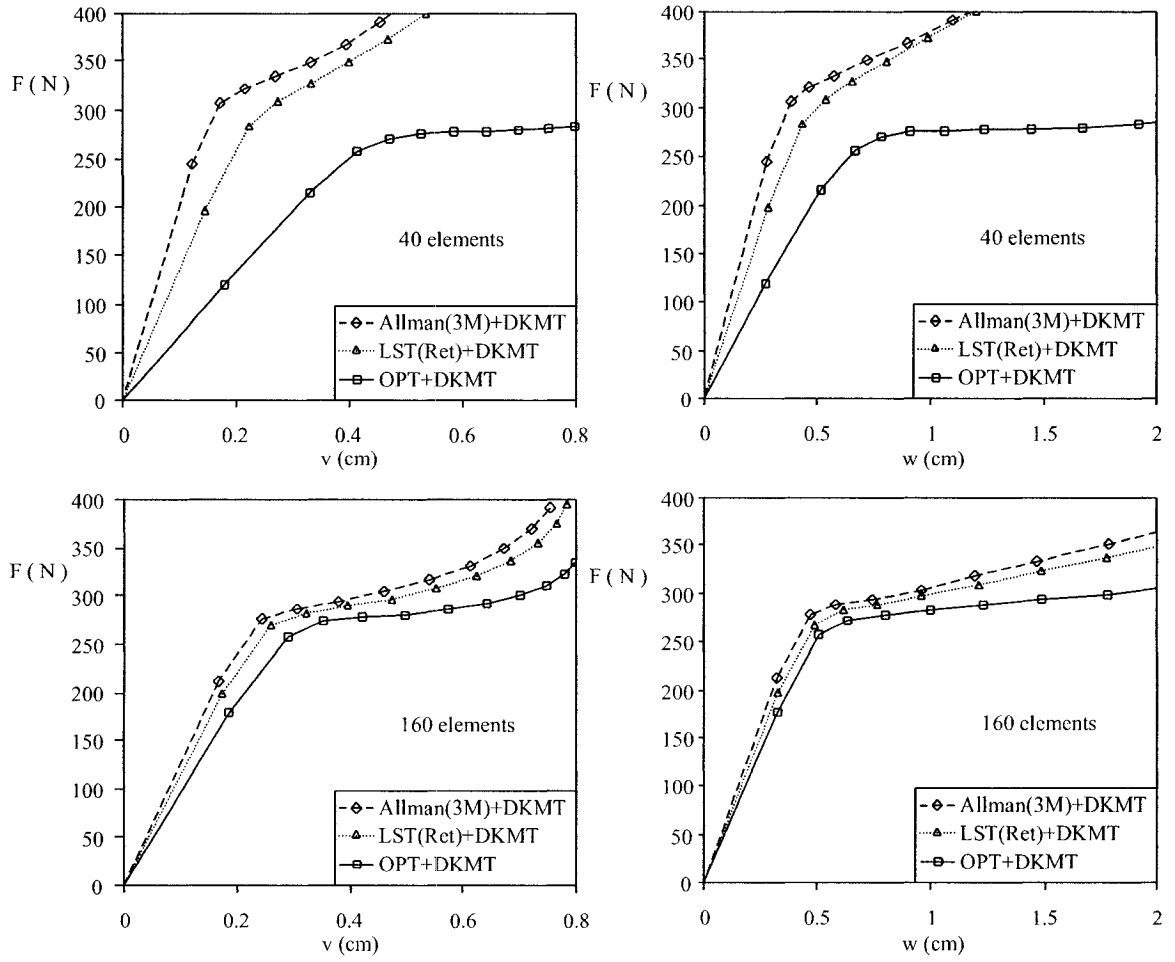


Figure 5.9: Response of the cantilever laminated angle (at the tip corner where the load is applied) subjected to end shear force modeled by 40 and 160 elements.

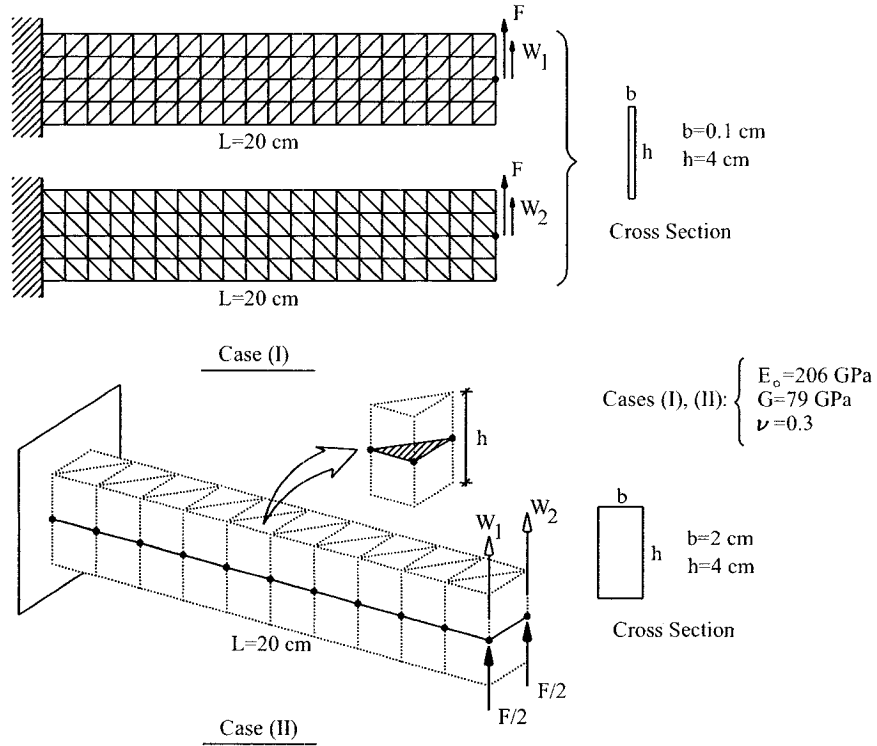


Figure 5.10: Thick cantilever beams modeled by triangular shell elements.

same length and thickness but different width $b = 2 \text{ cm}$ is also modeled by 20 triangular shell elements as shown in Figure 5.10, case(II). Two different shell elements (DKT+OPT) and (DKMT+OPT) are considered and for both cases (I) and (II), W is found by the relation $W = (W_1 + W_2)/2$.

Although the width of the beams in cases (I) and (II) are different, it is obvious that F/b , or load per unit width of each beam, should be the same at any tip deflection W . Figure 5.11 shows that the result found by the proposed thick shell element (DKMT+OPT) is almost the same as the result found for case (I) which means that the proposed thick shell element is capable to model the shear effect, accurately.

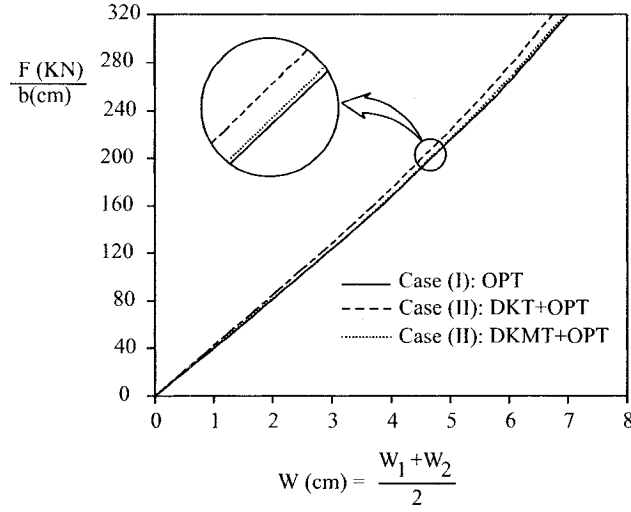


Figure 5.11: Nonlinear response of the thick cantilever plates.

5.2.4 Shallow shell under uniformly distributed transverse load

In this example, a shallow shell with dimensions shown in Figure 5.12 is considered under downward uniformly distributed load q . The shell is made of unidirectional laminate with 40 layers, and mechanical properties similar to those in the previous examples. Although the length to thickness ratio of this shell is about 37 but due to the high ratio of E_1/G_{13} in this unidirectional laminate, it is predicted that shear deformations are considerable. Two different meshes with 40 and 320 elements are considered, and the deflection of the center of the shell is obtained using different combinations of membrane and bending elements (Figure 5.13). In each case, limit and bifurcation points are also found and shown in the figure.

It is observed that again, the result found by the proposed element are very close for two different meshes, and other combinations of the membrane and bending elements converge to the same result when a fine mesh is used. The same structure

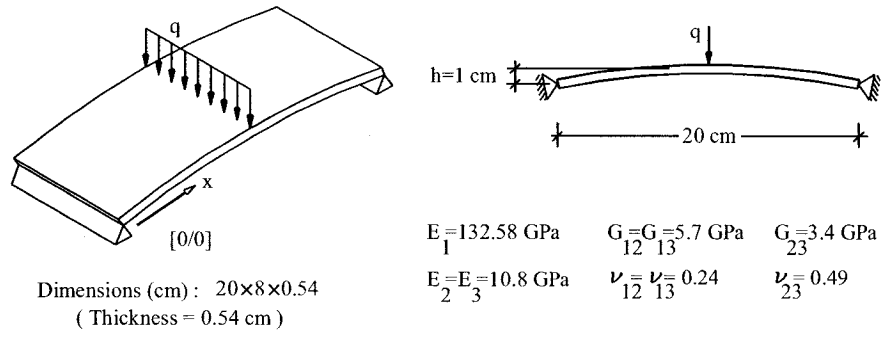


Figure 5.12: Shallow shell under downward uniformly distributed load.

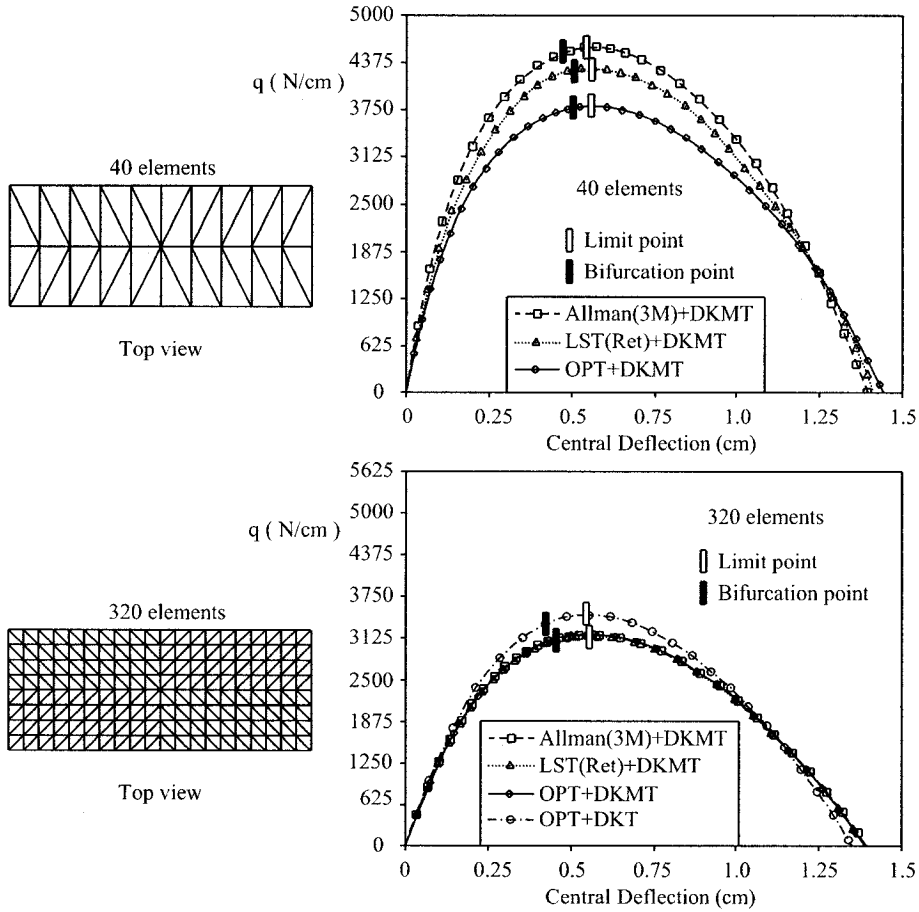


Figure 5.13: Response of the shallow shell modeled by 40 and 320 elements.

with fine mesh is also analyzed using DKT instead of DKMT, and the result for (DKT+OPT) is shown as a sample. As it was already predicted, in this case using DKT instead of DKMT leads to erroneous results for limit and bifurcation points which confirms the significant effect of shear deformations.

5.3 Numerical results for shape optimization

In order to demonstrate the efficiency and accuracy of the proposed design optimization methodology, some illustrative examples are presented considering stability or displacement constraints. Accuracy of the proposed algorithm is compared to that of the SQP (Sequential Quadratic Programming) gradient based method. Regarding the sensitivity analysis, since the main idea is to only evaluate the accuracy of the proposed method by comparing its results with that of the gradient based methods, finite difference method (FDM) is used as an alternative approach for sensitivity analysis in the SQP method.

5.3.1 Shape optimization of a shallow spherical shell: mass minimization subject to the constant load

Figure 5.14 shows a shallow spherical shell with overall thickness t subjected to a 8000 N downward load at the apex. The optimization problem is to minimize the total mass of the shell subject to stability constraint. This means that F_{cr} in the optimum design should be equal or very close to (but more than) 8000 N . The shell is modeled with 144 proposed triangular shell elements and due to symmetry, only a quarter of the shell is analyzed. Design variables are the thickness t , and the shape design variables h_1 , h_2 , and h_3 . The initial values for h_1 , h_2 , and h_3 are considered

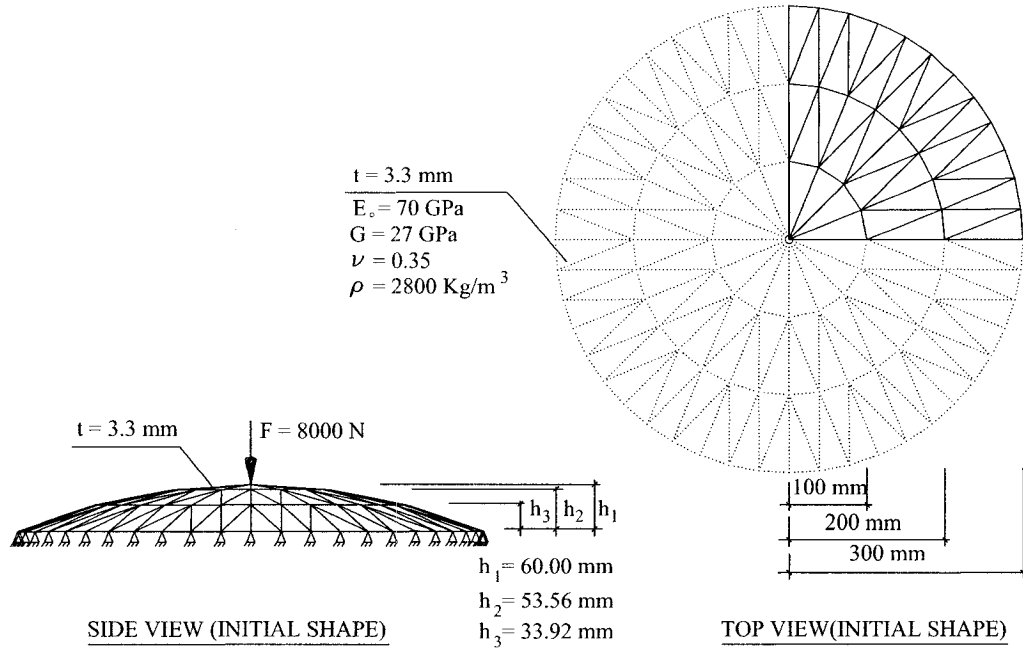


Figure 5.14: Shallow spherical shell subject to transverse load

60.00 mm, 53.56 mm and 33.92 mm, respectively. Initial value $t = 3.3 \text{ mm}$ is considered for the overall thickness of the shell. Initial total mass is equal to $M = 2.7110 \text{ Kg}$ for the mass density of 2800 Kg/m^3 . Optimization procedure starts by changing the nodal positions in vertical direction and considering step size parameter $r = 10$. Three regions have been considered ($h > h_2$, $h_2 > h > h_3$, $h_3 > h$), and average strain energy density in each region has been considered in optimization process.

Figure 5.15 shows the results of optimization (optimum shape, bending energy ratio and mass iteration histories) based on the proposed optimality criteria in section 4.6. In this analysis, the design is scaled at each iteration by changing the overall thickness of the shell, and the thickness is selected in mm to 1 decimal place. In the third iteration the bending energy ratio increases, which means that the change in the thickness due to the design scaling is not in the proper direction towards the optimal

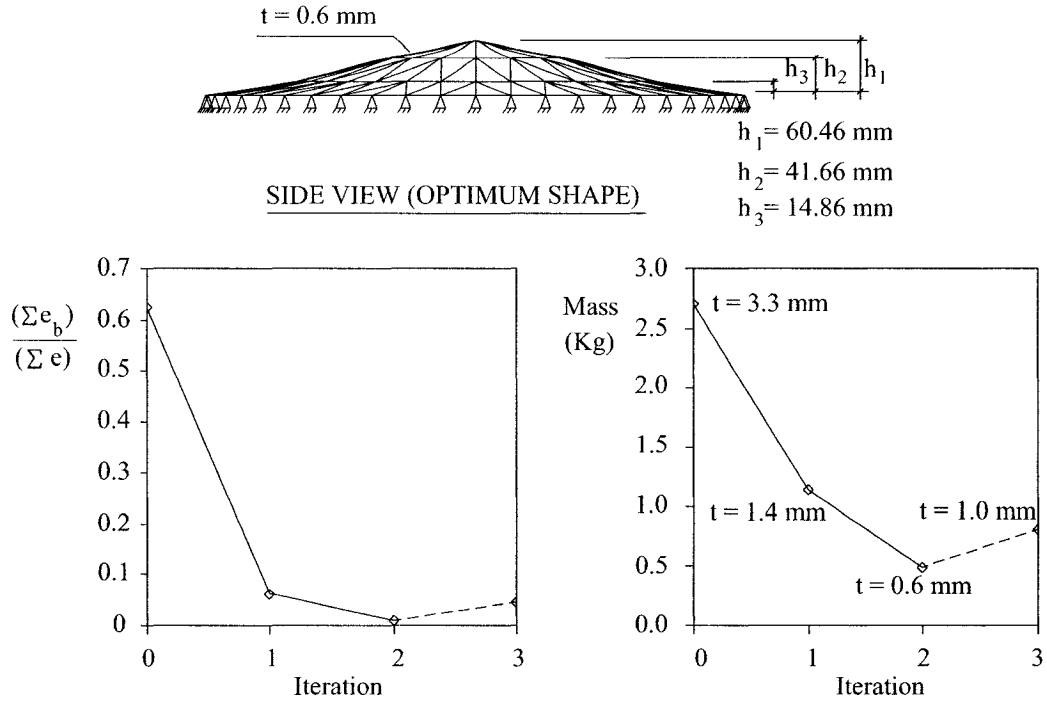


Figure 5.15: Optimum shape, and variation of the mass and bending energy ratio for the dome shell (thickness scaling)

design. As a result, the analysis should be continued with the previous thickness, but it is not possible because of the stability constraint. Thus the analysis terminates and the minimum mass $M = 0.4844 \text{ Kg}$ is achieved in the second iteration.

5.3.2 Width optimization of a cantilever plate: mass minimization subject to the constant load

In this example the proposed optimality criterion in section 4.6 is used to optimize a plate with displacement constraint. A cantilever plate with end load $F = 200 \text{ N}$ is shown in Figure 5.16, and the objective is to optimize the width of the plate in order to minimize the mass subject to a displacement constraint $W < 50 \text{ cm}$ at the tip. The initial dimensions $9 \text{ cm} \times 100 \text{ cm}$ and thickness $t = 4 \text{ mm}$ are considered for the plate. The initial total mass of the plate considering mass density of $\rho = 7850 \text{ Kg/m}^3$

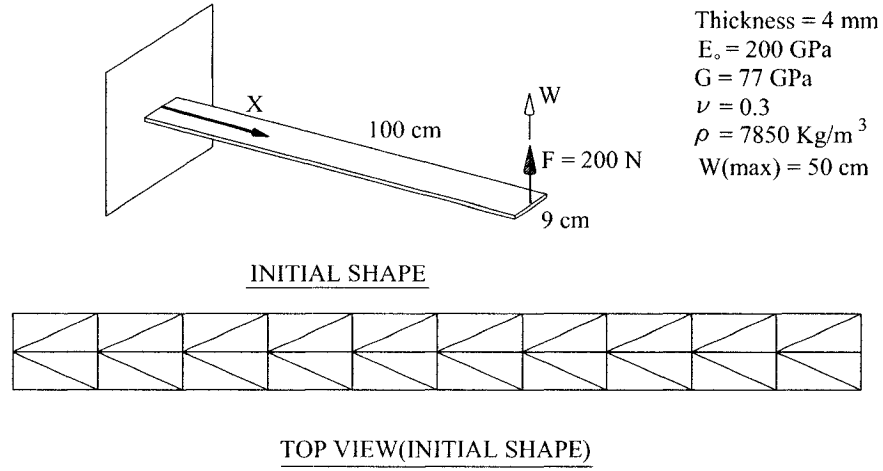


Figure 5.16: Cantilever plate with end load

is $M = 2.8260$ Kg. The plate is modeled with 40 proposed triangular shell elements, and due to symmetry only half of the plate is analyzed. The width of the plate at each station is considered as the shape design variable and design scaling is done by multiplying the width of the plate at every point by a scaling factor. The step size parameter is considered as $r = 10$.

Figure 5.17 shows the optimum shape and variation of $\rho \hat{e}_i$ over the length of the cantilever plate before and after optimization. It can be seen that the total mass decreases to $M = 2.0116$ Kg while the average strain energy density approaches the uniform distribution.

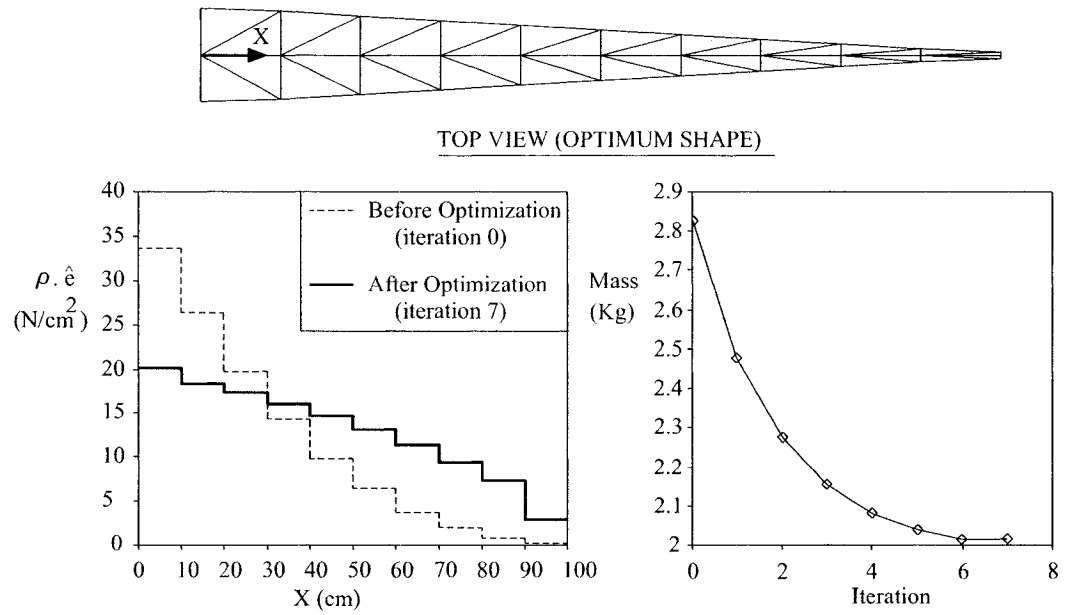


Figure 5.17: Optimum shape and variation of the mass and energy density for the cantilever plate

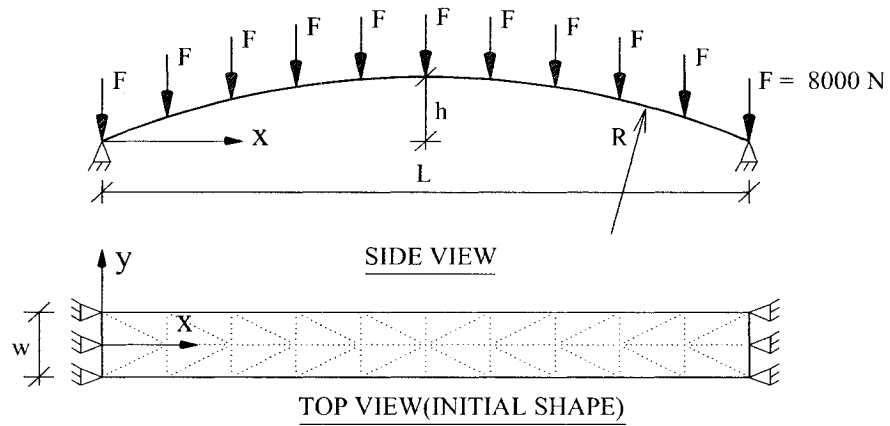


Figure 5.18: Shallow arch under downward loads

5.3.3 Width optimization of a shallow arch: mass minimization subject to the constant load

Figure 5.18 shows a shallow shell with thickness $t = 20 \text{ mm}$ subjected to eleven equally spaced concentrated vertical loads, each one equal to $F = 8000 \text{ N}$. Optimization problem is to find the best shape (by varying the width of the arch, and without any change in the thickness) in order to have minimum mass subject to the stability constraint. The plate is modeled with 40 proposed triangular shell elements and due to symmetry, only a quarter of the plate is analyzed. Step size parameter $r = 2$ is considered in analysis. The width of the shell at each station with initial value $W = 100 \text{ cm}$ is considered as the shape design variable, and design scaling is performed by changing the width of the shell at each point.

Figure 5.19 shows the result obtained by the proposed optimality criterion in section 4.6 compared to the one obtained by Sequential Quadratic Programming (SQP) method. Starting with the initial mass $M = 1611.12 \text{ Kg}$, the minimum mass obtained by the proposed method after 8 iterations and performing 8 nonlinear analysis is $M = 1226.30 \text{ Kg}$. Optimization by Sequential Quadratic Programming (SQP) method leads to a smaller mass equal to $M = 1213.10 \text{ Kg}$, but it requires 18 optimization iterations and 161 nonlinear analyzes. It may be seen that using the proposed design optimization methodology, one can efficiently obtain the optimum solution with an acceptable accuracy without any need to perform the time-consuming task of sensitivity analysis.

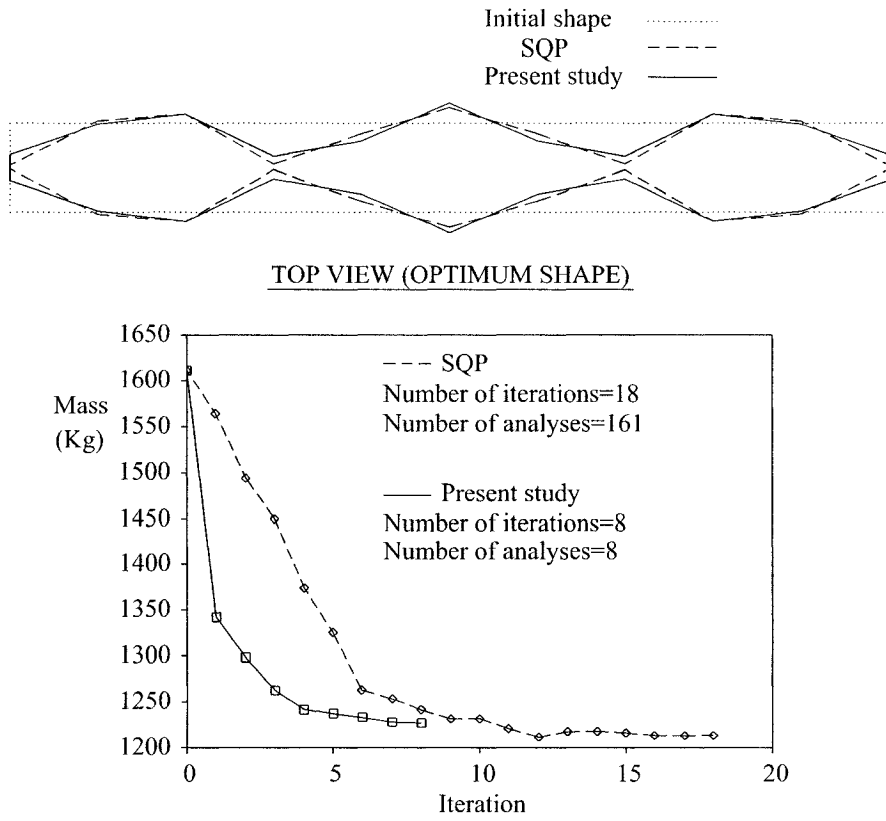


Figure 5.19: Optimum shapes and variation of the mass for shallow shell (present study vs SQP method)

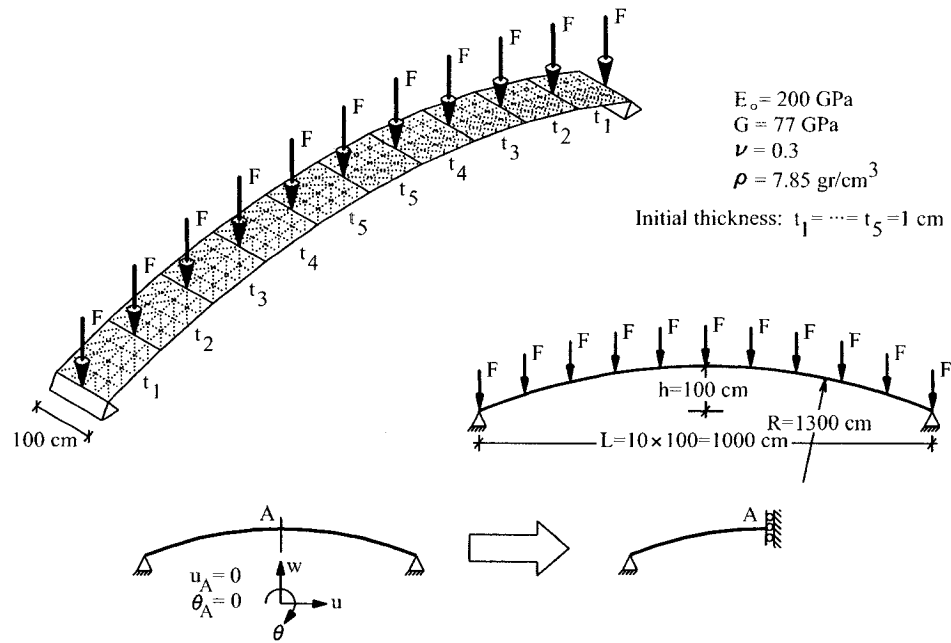


Figure 5.20: Shallow arch subjected to concentrated vertical loads.

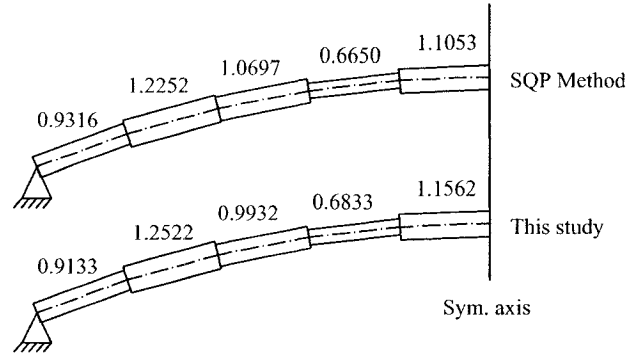


Figure 5.21: Optimum results of the thickness optimization (cm) for the shallow arch of Figure 5.20 subject to the constant mass (thicknesses have been exaggerated for better view.)

5.3.4 Thickness optimization of a shallow arch: limit load maximization subject to the constant mass

Figure 5.20 shows a shallow arch similar to the one in the previous example but with thickness $t = 1\text{ cm}$ subjected to eleven equal concentrated vertical loads F . The top of the arch is constrained such that only vertical movement is allowed. Optimization problem is to find the optimum thickness distribution in order to maximize the critical load subject to constant mass. The arch is modeled with 320 proposed triangular shell elements and due to symmetry, only a quarter of the arch is analyzed. Analysis is performed using five design variables t_1, t_2, \dots, t_5 for thickness values as shown in Figure 5.20, and $r = 10$ is considered as the step size parameter. Mass equality constraint is satisfied after each iteration by scaling the design variables using a scale factor. Analysis of the initial design ($t_1 = t_2 = \dots = t_5 = 1\text{ cm}$) leads to $F_{cr} = 1137.02\text{ N}$ as the critical load.

Figures 5.21 and 5.22 show the optimum results obtained by this study (proposed optimality criterion in section 4.5) compared to those obtained by using the Sequential

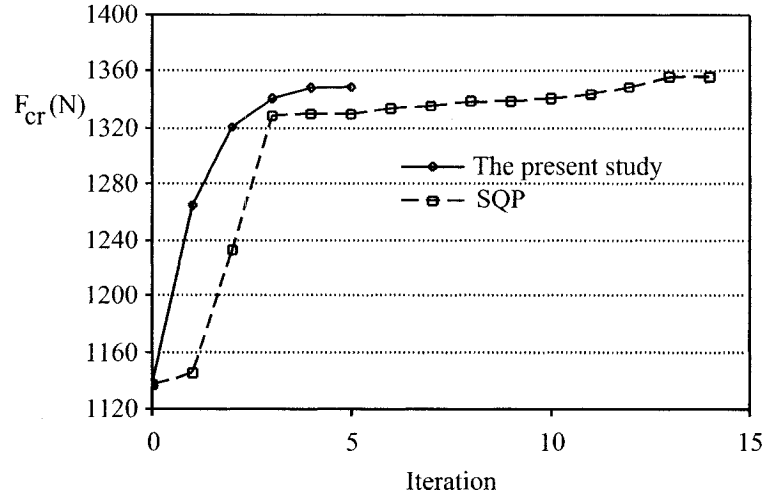


Figure 5.22: Variation of the critical load (limit load) during the thickness optimization for the shallow arch of Figure 5.20.

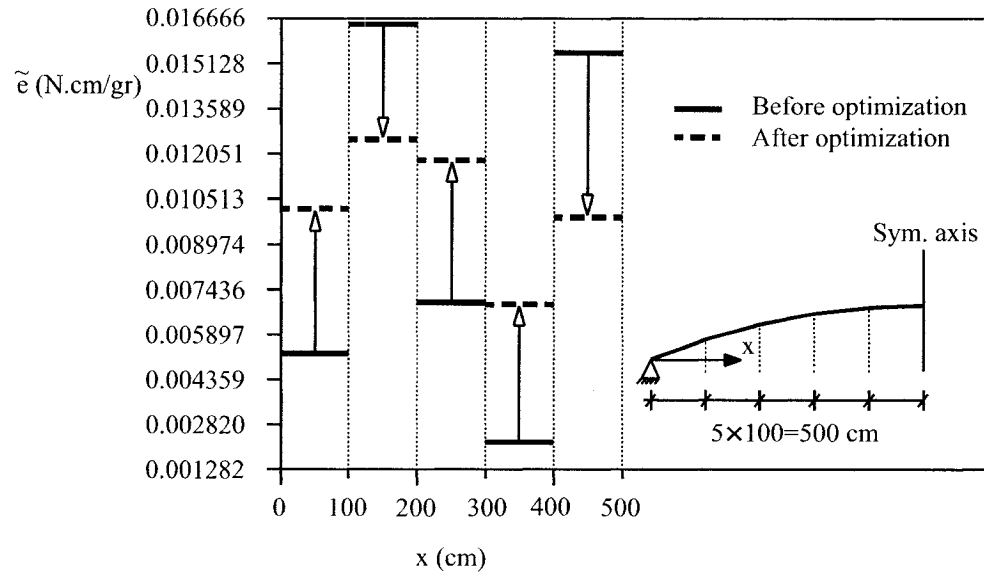


Figure 5.23: Variation of $\tilde{\sigma}$ during the thickness optimization for the shallow arch of Figure 5.20.

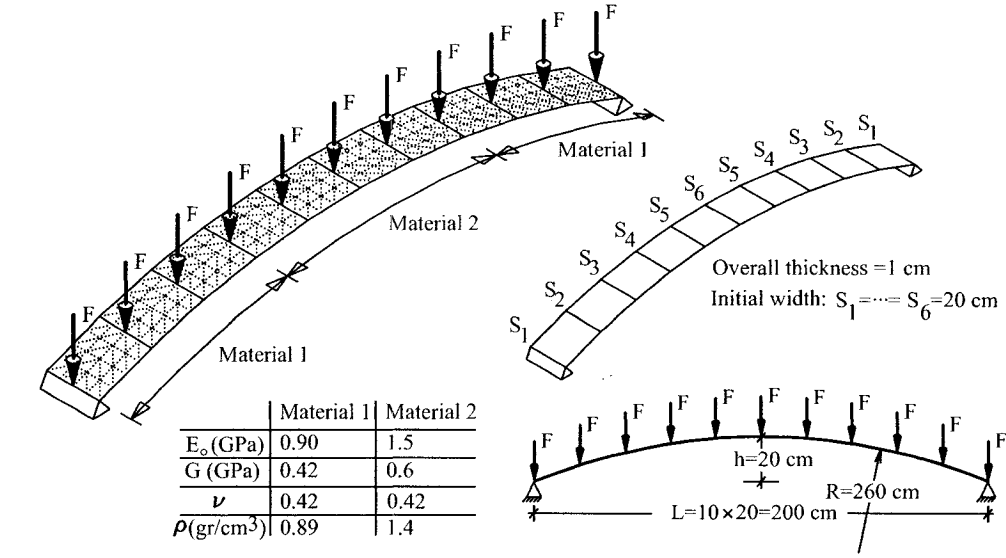


Figure 5.24: Shallow arch made of two different materials under top concentrated vertical loads.

Quadratic Programming (SQP) method. Since the lateral movement at the top of the arch is constrained, no bifurcation in the form of sideways deformation is observed, and the critical load is found to be only in the form of limit load (snap-through). It can be seen in Figure 5.22 that SQP method leads to a slightly higher critical load ($F_{cr} = 1356.40$ N) but it needs more iterations compared to the proposed method, which leads to $F_{cr} = 1349.69$ N at the optimum point. Figure 5.23 shows the values of \tilde{e} before and after optimization, confirming that \tilde{e} approaches a uniform distribution.

5.3.5 Width optimization of a shallow arch: bifurcation load maximization subject to the constant mass

In this example, a shallow arch similar to those in the previous examples, but with different dimensions and material properties, is considered again (Figure 5.24). This time, optimization is performed to find the optimum width for the arch at different stations in order to maximize the critical load subject to constant total mass. The

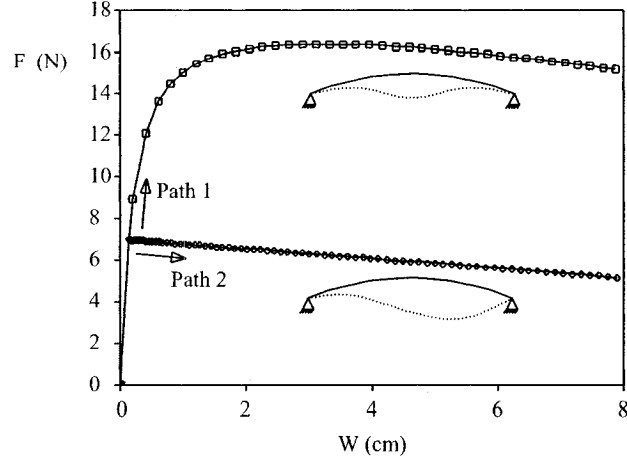


Figure 5.25: Limit and bifurcation points for the shallow arch in Figure 5.24 (before optimization.)

arch is made of two types of plastic with the following mechanical properties:

$$Type1 : E = 0.90 \text{ GPa}; G = 0.42 \text{ GPa}; \nu = 0.42; \rho = 0.89 \text{ gr/cm}^3$$

$$Type2 : E = 1.50 \text{ GPa}; G = 0.60 \text{ GPa}; \nu = 0.42; \rho = 1.40 \text{ gr/cm}^3$$

Analysis is performed using $r = 2$ as the step size parameter. By linking design variables in order to maintain the symmetry, six design variables S_1, S_2, \dots, S_6 for the width of the arch at different stations are considered, as shown in Figure 5.24.

Figure 5.25 shows the load–deflection (equilibrium) path for the arch before optimization. As it is seen, a critical point in the form of bifurcation happens at load $F_{cr} = 6.95 \text{ N}$ which is less than the limit load. Selecting the bifurcation load as the load carrying capacity of the structure, the proposed optimality criterion in section 4.5 is employed to optimize the width and maximize this bifurcation load. Figures 5.26 and 5.27 compare the results obtained by using the proposed optimality criterion method with those obtained by using the sequential quadratic programming (SQP) method. Again, it can be seen that the proposed method leads to almost the same

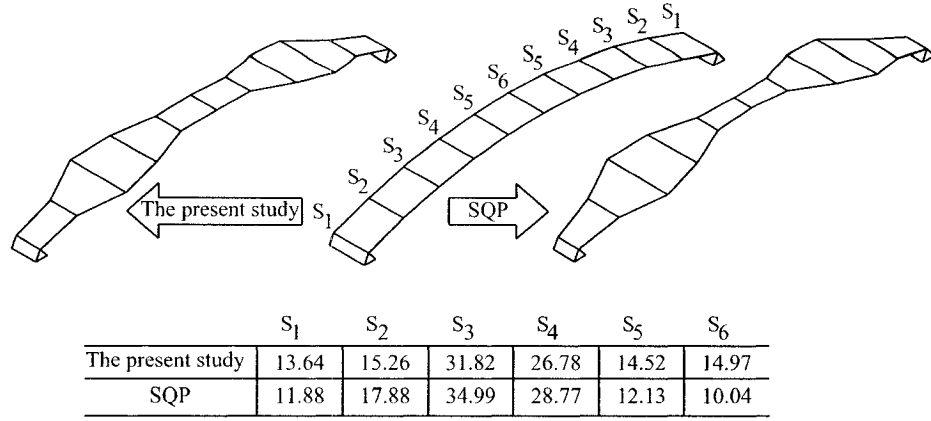


Figure 5.26: Results of the shape (width) optimization for the shallow arch in Figure 5.24 subject to constant mass.

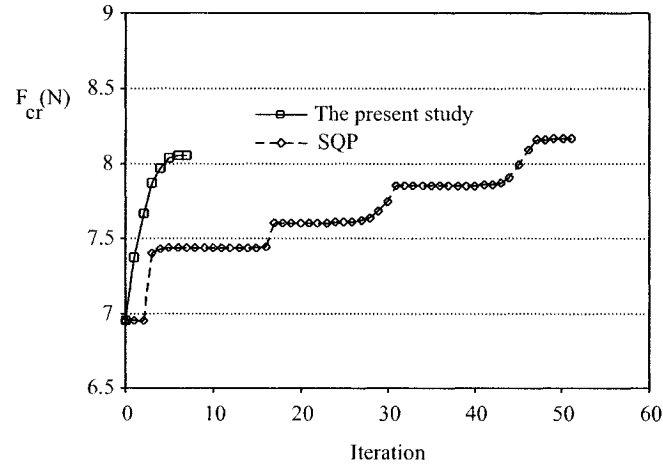


Figure 5.27: Variation of the critical load (bifurcation load) during the width optimization for the shallow arch in Figure 5.24.

optimum shape and critical load ($F_{cr} = 8.06 \text{ N}$) in much less number of iterations compared to the SQP method (which leads to $F_{cr} = 8.17 \text{ N}$), without any need to perform the time-consuming task of sensitivity analysis at every iteration.

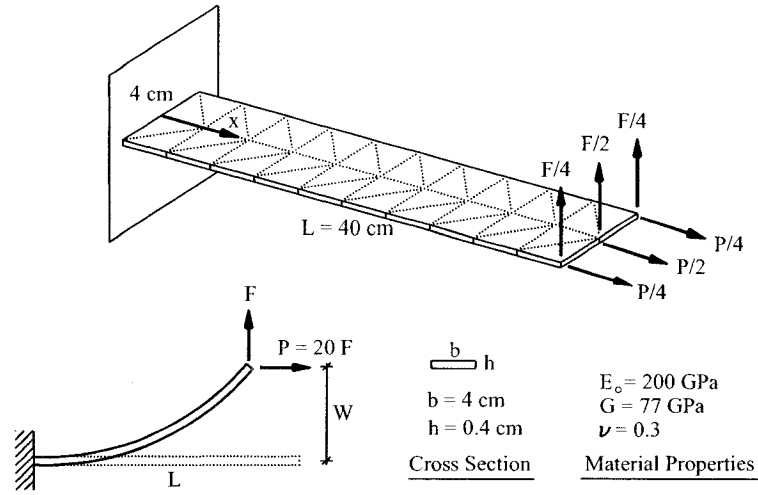


Figure 5.28: Cantilever plate subject to axial and shear forces at the tip.

5.3.6 Thickness optimization of a cantilever plate: load maximization subject to the constant mass

Figure 5.28 shows a cantilever plate subject to the shear load F and axial force $P = 20F$ at the tip. Dimensions of the plate are $40 \text{ cm} \times 4 \text{ cm}$ with overall thickness $t = 0.4 \text{ cm}$, and it is made of isotropic material (steel) with the following mechanical properties:

$$E_o = 200 \text{ GPa}, G = 77 \text{ GPa}, \nu = 0.3$$

The objective is to perform the thickness optimization in order to maximize the load capacity F subject to the constant volume or mass. In this example the load capacity F is found based on the displacement $W = 1 \text{ cm}$, where W is the vertical deflection at the tip of the plate. The plate is modeled by 40 proposed triangular shell elements, and due to the symmetry only half of the plate is analyzed.

Nonlinear analysis results in $F = 49.81 \text{ N}$ as the initial load capacity of the plate. Figure 5.29 shows the results of thickness optimization subject to constant volume, using UASEV and also USED criteria. In both cases, convergence is achieved in 5

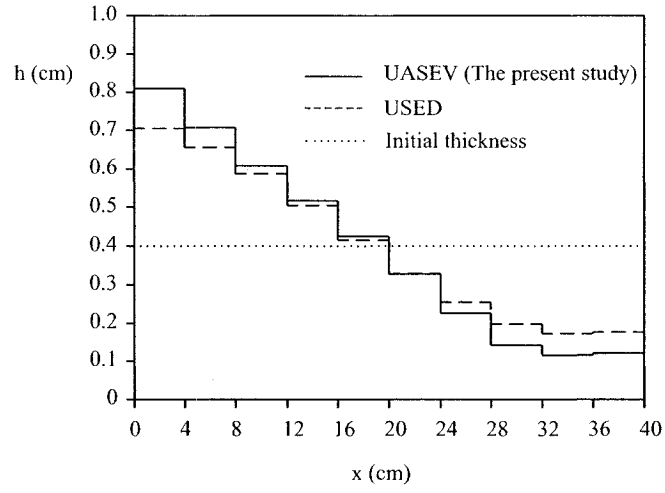


Figure 5.29: Variation of the thickness over the length of the cantilever plate of Figure 5.28 after optimization.

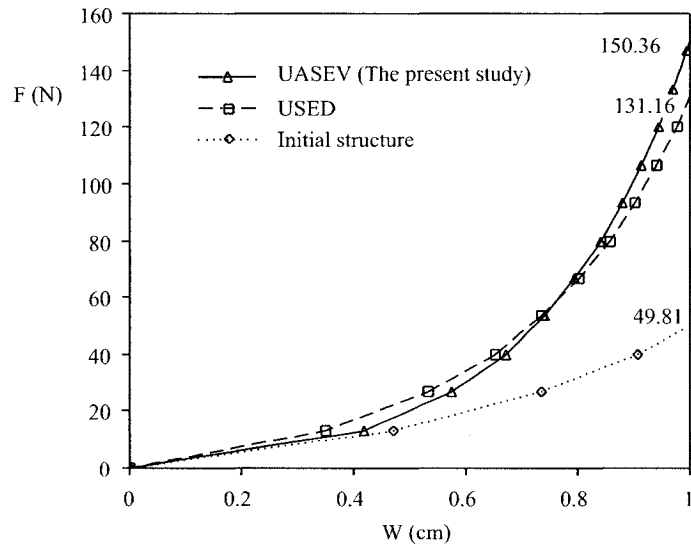


Figure 5.30: Nonlinear behavior of the cantilever plate of Figure 5.28 before and after optimization.

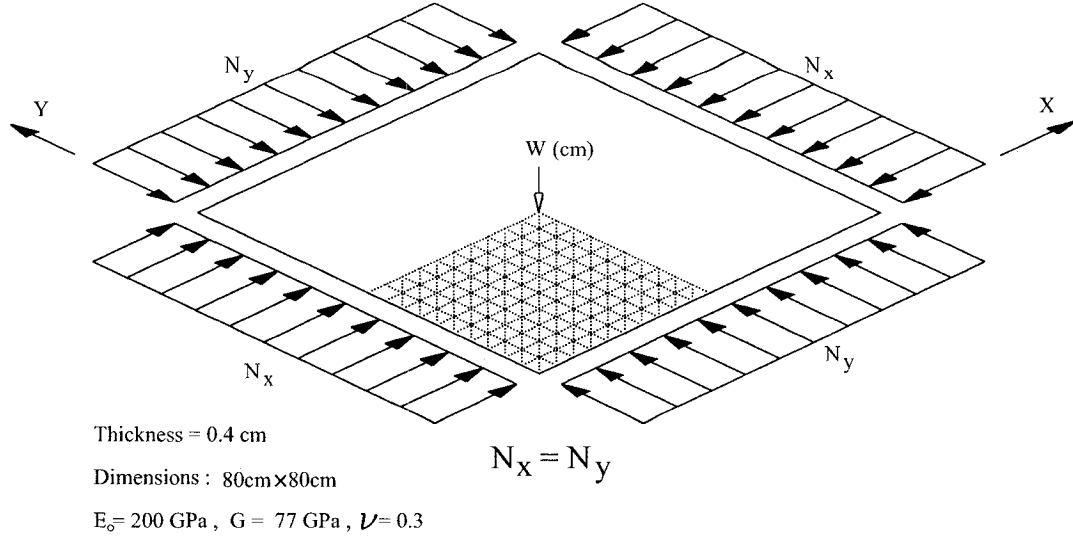


Figure 5.31: Square plate with simple supports subjected to biaxial compressive forces.

iterations, with $r = 2$ as the step size parameter. Nonlinear behavior of the plate optimized by UASEV and USED criteria is also shown in Figure 5.30.

It is observed that optimization using the UASEV criterion increases the load capacity of the plate to $F = 150.36 \text{ N}$, compared to $F = 131.16 \text{ N}$ obtained by using USED criterion. In Figure 5.30, it is interesting to note that in the range of $W \leq 0.75 \text{ cm}$, the load capacity of the plate optimized by UASEV criterion is slightly less than that of the one optimized by USED, however since the optimality criteria are applied at the limit point (i.e. $W = 1 \text{ cm}$) UASEV finally overcomes USED and leads to a higher load capacity.

5.3.7 Thickness optimization of a simply supported square plate: load maximization subject to the constant mass

Figure 5.31 shows a simply supported square plate under the biaxial compressive edge forces $N_x = N_y$. Dimensions of the plate are $80 \text{ cm} \times 80 \text{ cm}$ with overall thickness

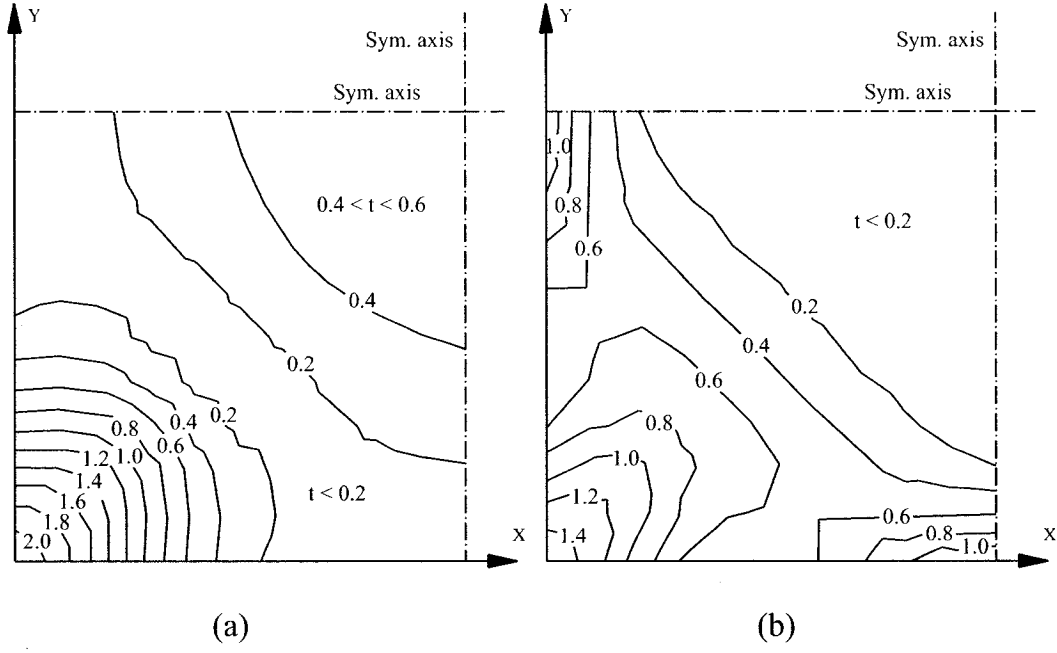


Figure 5.32: Results of thickness optimization (*cm*) for a quarter of the plate shown in Figure 5.31: (a) UASEV criterion. (b) USED criterion.

$t = 0.4$ *cm*, and it is made of isotropic material (steel) with the following mechanical properties:

$$E_o = 200 \text{ GPa}, G = 77 \text{ GPa}, \nu = 0.3$$

In order to initiate the lateral deflection, an imperfection in the form of a half sine wave with the maximum value 1 *mm* at the center of the plate is considered. The objective is to optimize the thickness of the plate, while having the same total volume or mass, in order to maximize the load capacity for $W = 0.4$ *cm*, where W is the vertical deflection at the center of the plate. The plate is modeled by 800 proposed triangular shell elements, and due to the symmetry only a quarter of the plate is analyzed. Performing the nonlinear analysis results in $N_x = N_y = 369.5$ *N/cm* as the initial load capacity of this plate.

Figure 5.32(a,b) shows the results of thickness optimization subject to constant

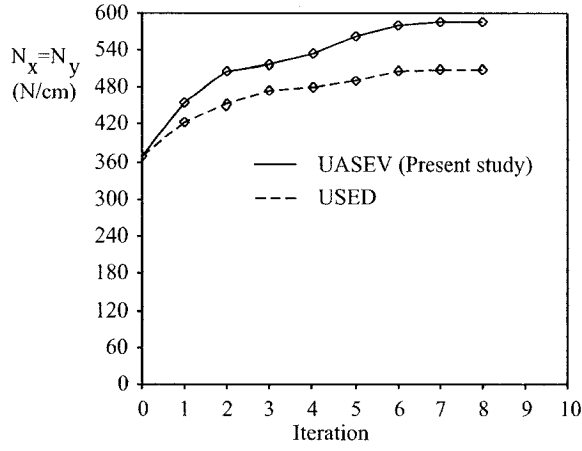


Figure 5.33: Change of load carrying capacity of the plate shown in Figure 5.31 during the thickness optimization using USED and UASEV criteria.

volume for a quarter of the plate using UASEV and USED criteria in 8 iterations, respectively. In both cases $r = 4$ has been considered as the step size parameter. It is observed that optimization based on USED criterion tends to reduce the thickness in the middle of the plate and to increase it on the corners and mid-sides, while UASEV criterion tends to reduce the thickness on the mid-sides and to increase it on the corners and somewhat in the middle. Figure 5.33 shows the change of load carrying capacity of the plate, during the thickness optimization. Nonlinear analysis of optimal plate shows that the load capacity has been increased to $N_x = N_y = 584.3 \text{ N/cm}$, and $N_x = N_y = 509.2 \text{ N/cm}$ for UASEV and USED criteria, respectively, while having the same total volume. Although using any one of these two criteria increases the strength (or load capacity) of the plate, it is obvious that UASEV criterion is more efficient than USED.

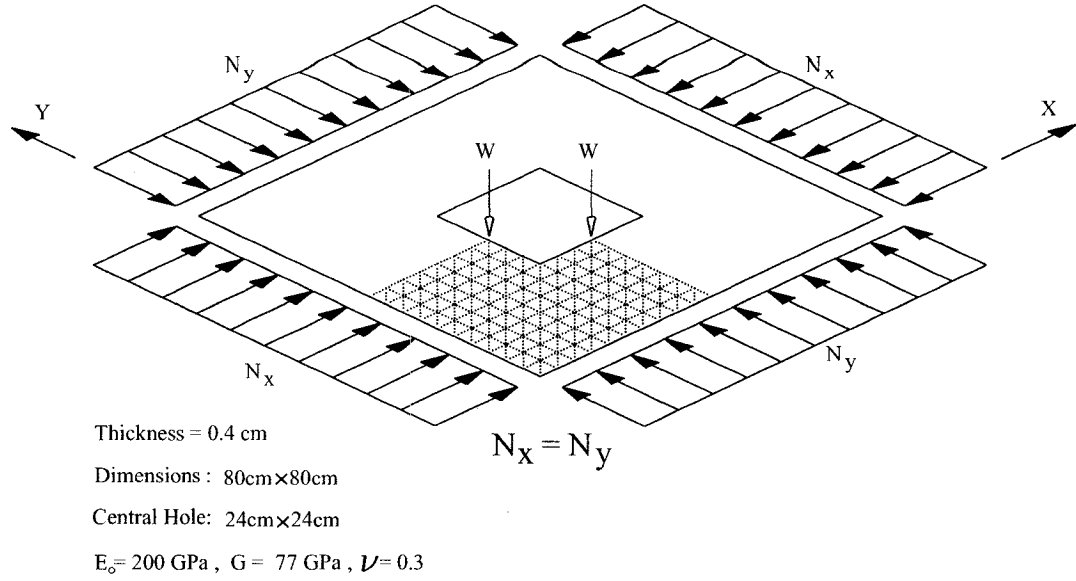


Figure 5.34: Square plate with a square hole in the center, and simple supports, subjected to biaxial compressive forces.

5.3.8 Thickness optimization and rib location for a simply supported square plate with square hole: load maximization subject to the constant mass

In this example the application of the UASEV criterion is shown for thickness optimization, and subsequently potential stiffener location for a stiffened plate. Figure 5.34 shows a $80\text{ cm} \times 80\text{ cm}$ simply supported square plate with overall thickness $t = 0.4\text{ cm}$ and a $24\text{ cm} \times 24\text{ cm}$ square hole in the center. Loading and material properties are similar to those in the previous example (section 5.3.7). Also, an imperfection in the form of a half sine wave with the value of 1 mm around the central hole is considered to initiate the lateral deflection. The objective is to optimize the thickness and find the potential stiffener locations subject to constant volume or mass, in order to maximize the load capacity for $W = 0.4\text{ cm}$, where W is the deflection at the midpoint of the hole edges. In this example, the following design

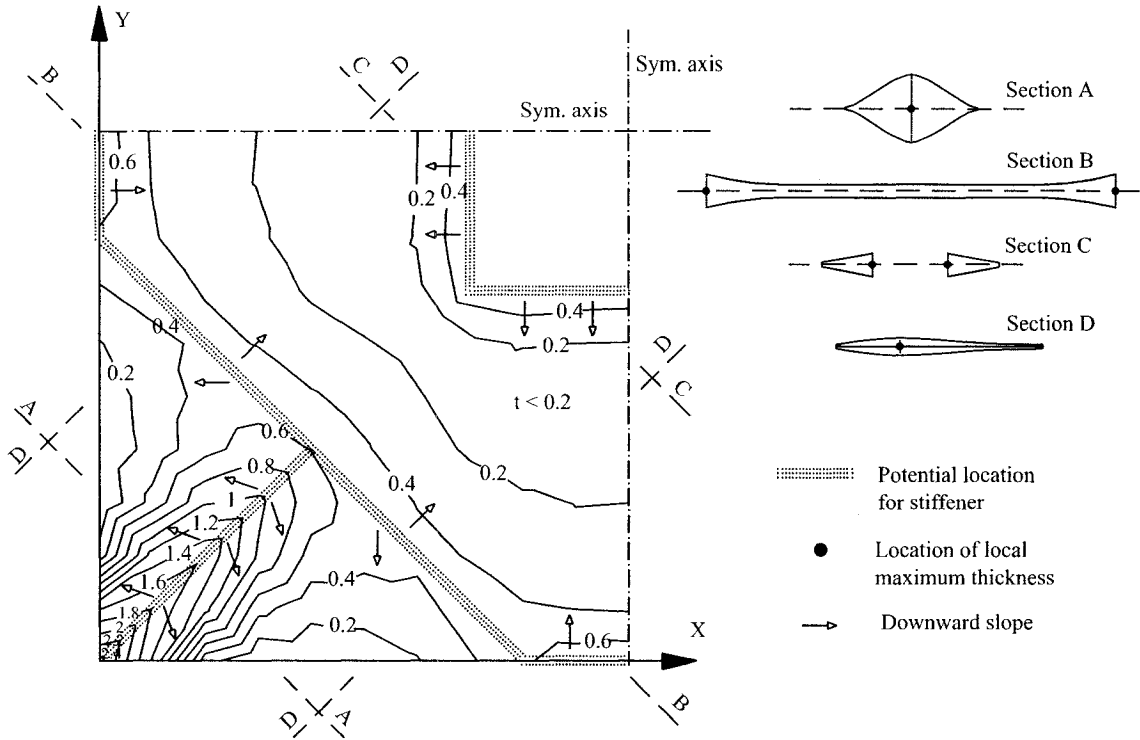


Figure 5.35: Result of thickness optimization (*cm*) for a quarter of the plate shown in Figure 5.34. Thicknesses of the sections have been exaggerated for better view.

constraints should also be satisfied for the final design:

- Maximum height of the stiffeners= 5 *cm*.
- Same thickness for the stiffeners and the plate in the final design.

Similar to the previous example, a quarter of the plate is modeled by 182 proposed triangular shell elements. Although usually in finite element analysis a finer mesh is used near notches and holes, a uniform mesh is used in this example to avoid computational difficulties due to large number of elements. Performing the nonlinear analysis results in $N_x = N_y = 290.8 \text{ N/cm}$ as the load capacity of this plate for $W = 0.4 \text{ cm}$. Thickness optimization is performed using UASEV criterion with $r = 4$ as the step size parameter. Iterative process converged after 9 iterations.

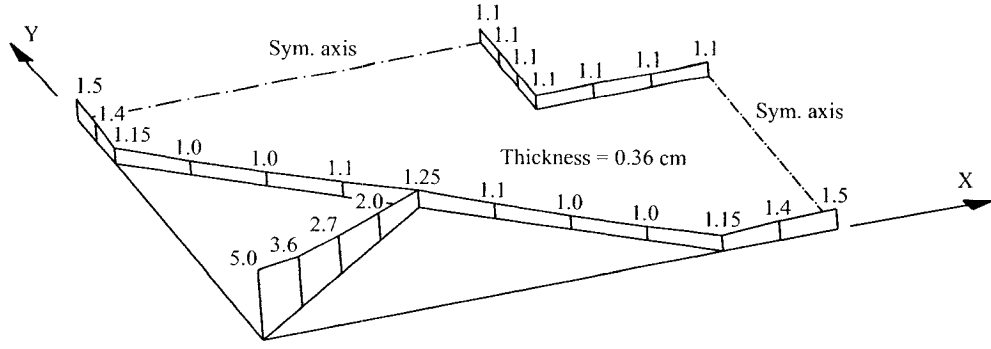


Figure 5.36: A quarter of the plate shown in Figure 5.34 with stiffeners at potential locations. Numbers show the height of the stiffeners (*cm*).

Variation of the thickness for a quarter of the plate found based on the results of thickness optimization subject to constant total volume, is shown in Figure 5.35. Load carrying capacity of the plate after performing the thickness optimization, has increased to $N_x = N_y = 654.3 \text{ N/cm}$.

Based on this shape, and predefined design constraints mentioned above, stiffeners are located on the lines of maximum thicknesses (as shown in Figure 5.36) on a plate with constant thickness. Height of the stiffeners are proportional to the thickness of the elements, with the maximum value of 5 *cm* according to the first design constraint. Keeping the total volume equal to the initial volume 2329.6 cm^3 , and considering the same thickness for stiffeners and plate (as per the second design constraint) a new overall thickness of $t = 0.36 \text{ cm}$ is found for the plate and the stiffeners. Nonlinear analysis of this stiffened plate shows that the load capacity has increased to $N_x = N_y = 560.4 \text{ N/cm}$ compared to $N_x = N_y = 290.8 \text{ N/cm}$ for the initial plate, however it has reduced compared to $N_x = N_y = 654.3 \text{ N/cm}$ for the plate with optimized thickness.

5.3.9 Thickness optimization and rib location for a simply supported square plate with square hole under downward surface load: load maximization subject to the constant mass

A plate similar to the one in Figure 5.34 is considered under the downward surface load q . Boundary conditions are similar to those in previous example except that in-plane deflections are not allowed for all four edges. As a result, membrane forces arise during the deflections due to bending. The objective is to maximize the load capacity for $W = 0.3 \text{ cm}$ using UASEV criterion, subject to constant total volume or mass. The following design constraints should also be satisfied at the final optimum design:

- Maximum height of the stiffeners= 10 cm .
- Thickness of the stiffeners= 0.4 cm .

A quarter of the plate is modeled by 182 proposed triangular shell elements. Nonlinear analysis results in $q = 0.318 \text{ N/cm}^2$ as the load capacity of this plate. In the next step, UASEV criterion with $r = 4$ is employed for thickness optimization. New thickness distribution and potential locations for stiffeners are shown in Figure 5.37, which are found after 9 iterations. Load carrying capacity of this plate after performing the thickness optimization, has increased to $q = 0.865 \text{ N/cm}^2$.

Figure 5.38 shows the stiffeners located on the the lines of maximum thickness, with their height proportional to the new thickness of the elements, but not more than 10 cm , and their thickness equal to 0.4 cm according to the design constraint. Keeping the total volume equal to the initial volume, a new thickness $t = 0.339 \approx 0.34 \text{ cm}$ is

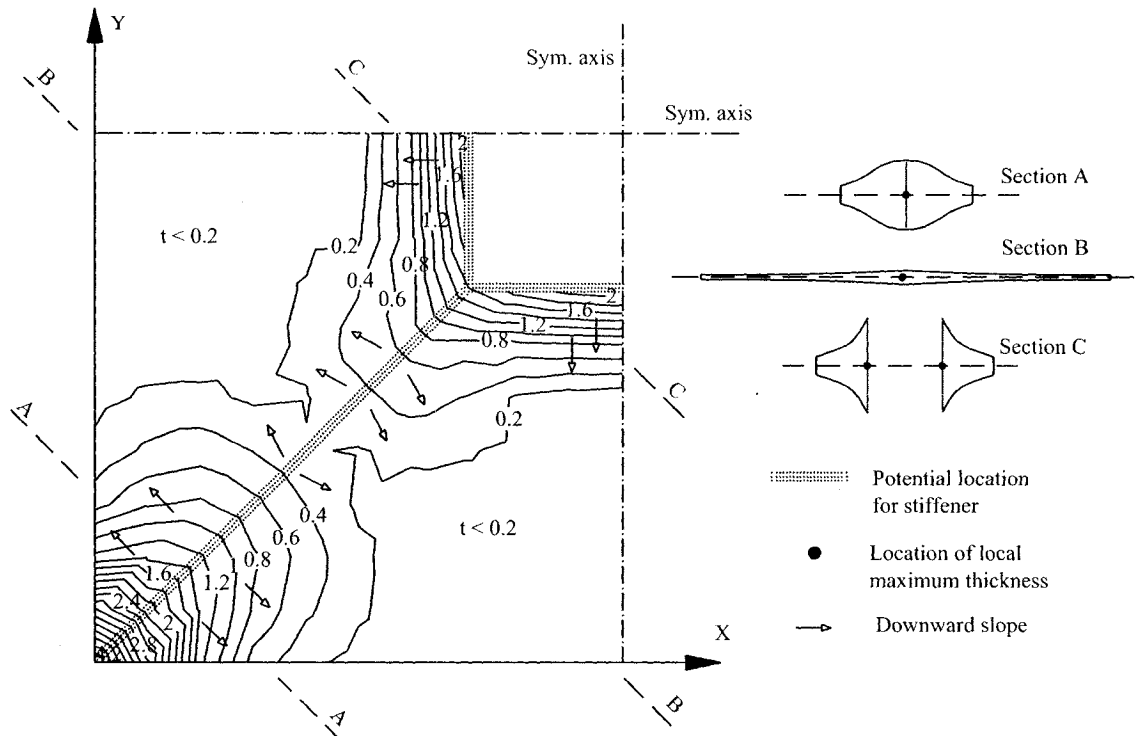


Figure 5.37: Result of thickness optimization (*cm*) for a quarter of the plate shown in Figure 5.34 with hinged supports ($u = v = w = 0$ at the edges) under the downward surface pressure load. Thicknesses of the sections have been exaggerated for better view.

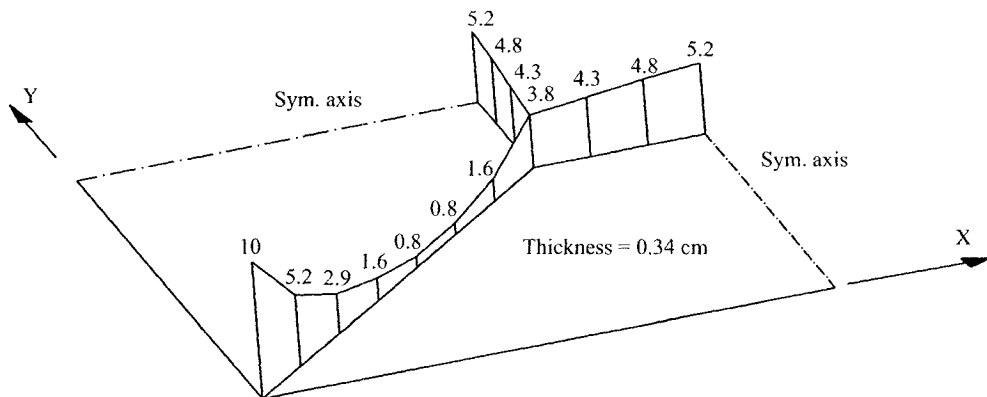


Figure 5.38: A quarter of the plate in Figure 5.34 with hinged supports under the downward surface with stiffeners at potential locations. Numbers show the height of the stiffeners (*cm*).

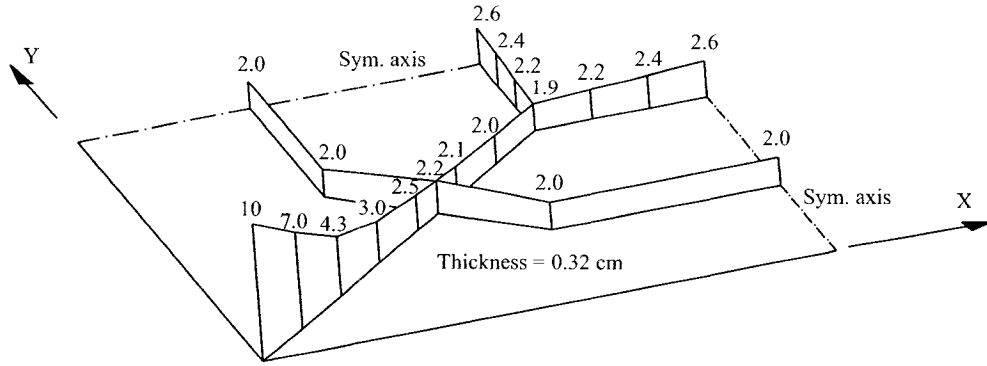


Figure 5.39: A quarter of the plate in Figure 5.34 with hinged supports under the downward surface and stiffeners at potential locations after the second rounds of rib locating. Numbers show the height of the stiffeners (*cm*).

found for the plate. Nonlinear analysis shows that the load capacity for $W = 0.3 \text{ cm}$ has increased to $q = 1.26 \text{ N/cm}^2$ compared to $q = 0.318 \text{ N/cm}^2$ for the initial plate, and compared to $q = 0.865 \text{ N/cm}^2$ for the plate with optimized thickness.

It should be mentioned that once the ribs are placed on a plate, structural behavior of the plate changes considerably. Thus, as mentioned before, it seems appropriate to repeat the optimization process for the stiffened plate, to obtain any further possible stiffener locations, and also modify the heights of the previously located stiffeners. Figure 5.39 shows the result of the optimized plate after the second round of optimization. It may be seen that a new series of stiffeners are found and the heights of the previous stiffeners have also been modified. Performing nonlinear analysis, the load capacity of the stiffened plate after the second round of optimization is found to be $q = 1.57 \text{ N/cm}^2$ compared to $q = 1.26 \text{ N/cm}^2$ after the first round.

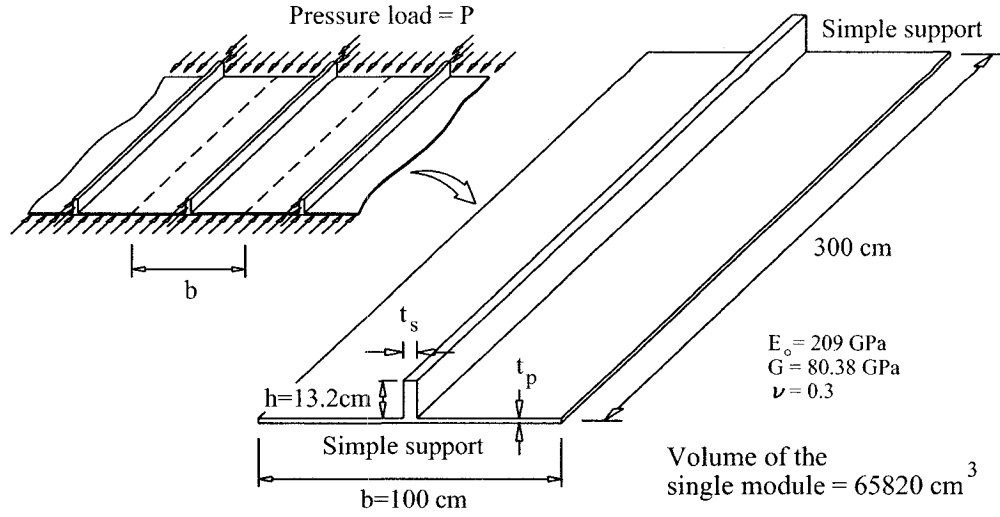


Figure 5.40: Stiffened panel under axial load.

5.4 Shape optimization of stiffened panels considering local buckling

In this section, two numerical examples are presented. The first example, is basically a one-variable problem and allows us to focus on the aspects of local buckling during the change of the shape, without going through the details of optimization process. The second example is a multi-variable problem which is solved using the proposed method (section 4.8) to consider local buckling and mode switching during the optimization process.

5.4.1 One-variable design of a stiffened panel

As the first example, a stiffened panel shown in Figure 5.40 is considered under both stress and stability constraints. The panel is infinitely wide and only a single module of the panel with the boundary conditions shown in Figure 4.10 is considered with the dimensions and material properties given in Figure 5.40. Thickness of the plate and stiffeners (t_p and t_s) are considered as the design variables. The objective is to

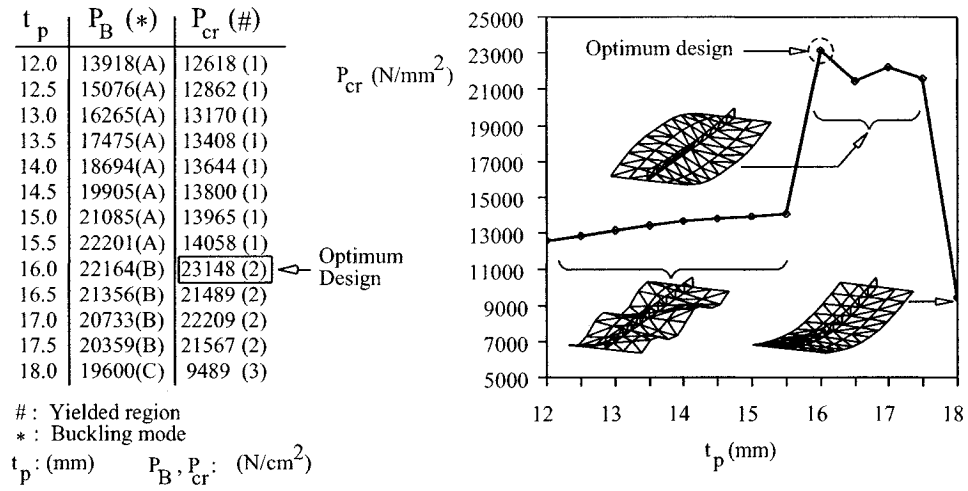


Figure 5.41: Results of the analysis of the stiffened panel of Figure 5.40 for different values of t_p (mm)

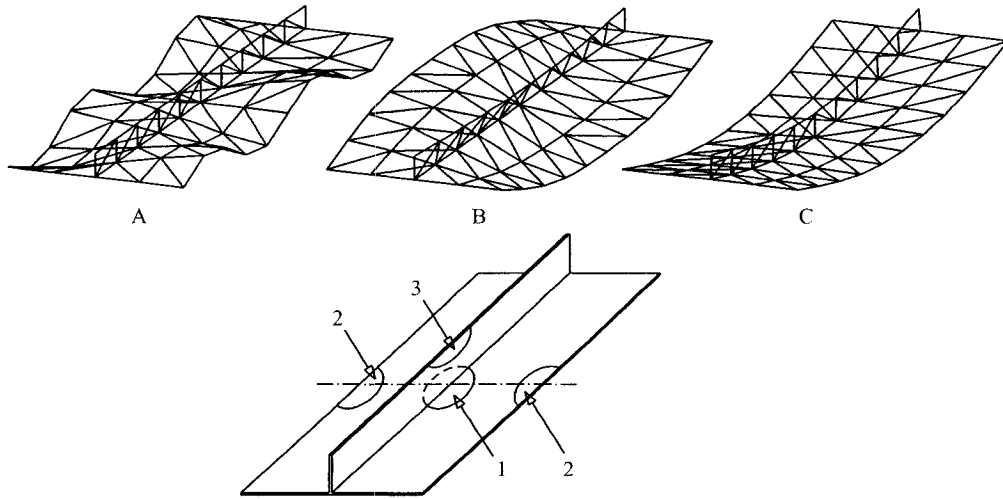


Figure 5.42: Buckling modes and yielded regions for the stiffened panel in Figure 5.40.

maximize the load capacity of a single module of this stiffened panel subject to the volume equality constraint $V = 65820 \text{ cm}^3$. Stress constraint $\sigma_{VM} \leq 25000 \text{ N/cm}^2$ (with σ_{VM} representing the von Mises stress), and also stability constraint (limit load) are considered in the design. The inequality side constraint $12 \text{ mm} \leq t_p \leq 18 \text{ mm}$ is also considered for the plate thickness. This problem may actually be reduced to a one-variable problem, since the thickness of the stiffener may be obtained when changing the plate thickness, using the volume equality constraint. Thus, it is possible to analyze the panel within the range $12 \text{ mm} \leq t_p \leq 18 \text{ mm}$ for several thicknesses of the plate and corresponding stiffener thickness.

Figure 5.41 shows the result of analysis for different values of t_p . For each case, the first bifurcation load (P_B) and the corresponding mode shape are found by the linear buckling analysis of the single module, as shown in the second column of the table in the Figure 5.41 (mode shapes A, B and C are shown in Figure 5.42). Then for each case, nonlinear analysis is performed considering an imperfection similar to the first buckling mode, and maximum value of 1 cm . Load capacity of the imperfect stiffened panel is found based on the stress and stability constraints, and is shown in the third column of the table in Figure 5.41 (P_{cr}). It is seen that in this example always a region in the imperfect structure reaches to the maximum stress prior reaching to the nonlinear limit load. The region where yielding happens first in the imperfect structure is mentioned in the third column of the table as (1), (2), or (3), and are also shown in Figure 5.42. Load capacities (P_{cr}) for different designs have been plotted in Figure 5.41. It is observed that the design with $t_p = 16 \text{ mm}$ has the highest load capacity and is therefor the optimum design.

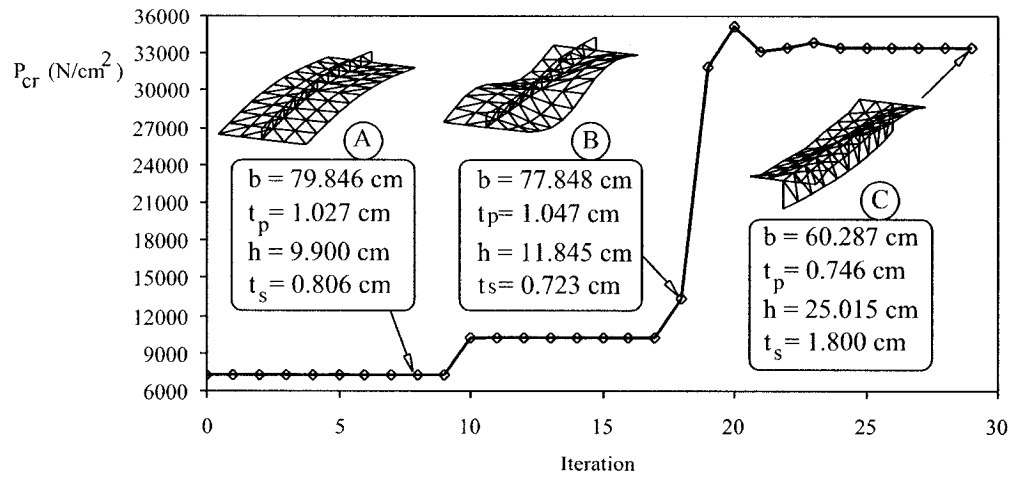


Figure 5.43: Iteration history for the multi-variable design optimization of a stiffened panel.

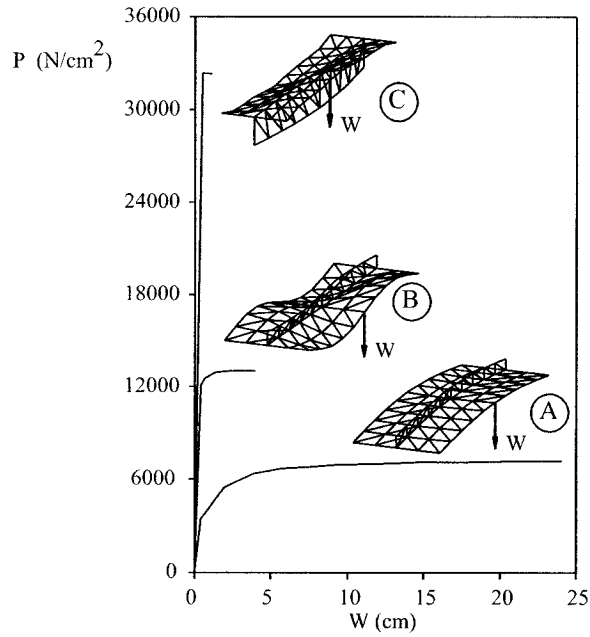


Figure 5.44: Change of the nonlinear behavior during the multi-variable design optimization of a stiffened panel.

As it is seen, for the lower values of t_p , the stiffened panel fails by local buckling of the panel, however as t_p is increased the buckling mode changes and finally at $t_p = 18 \text{ mm}$ the structure tends to fail by global buckling. This example shows that as the shape of the structure changes during optimization process, failure mode may also change as well, and a single unique failure mode may not be considered throughout the whole process.

5.4.2 Multi-variable design of a stiffened panel

A stiffened panel similar to the one in the previous example with constant length of 250 cm and four design variables b , t_p , h , and t_s is considered. The objective is to maximize the load capacity of this stiffened panel subject to the volume equality and stability constraints. No stress constraint is considered in the design. Here again, the first bifurcation load and the corresponding mode shape are found by the linear buckling analysis of the single module, and then nonlinear analysis is performed considering a small imperfection similar to the first buckling mode. Optimization is performed using the gradient-based sequential quadratic programming (SQP) method of optimization, and sensitivity analysis is performed by the finite difference method. Figure 5.43 shows the iteration history, along with three sample points A , B , and C . Optimization process starts with $b = 80 \text{ cm}$, $t_p = 1 \text{ cm}$, $h = 10 \text{ cm}$, $t_s = 1 \text{ cm}$ as the initial point, and leads to the optimum design with $b = 60.287 \text{ cm}$, $t_p = 0.746 \text{ cm}$, $h = 25.015 \text{ cm}$, $t_s = 1.800 \text{ cm}$ (point C). Figure 5.44 shows the nonlinear behavior of three sample points A , B and C . Again it is seen that a unique failure mode may not be considered throughout the whole optimization process, and the proposed method

captures the mode switching which happens during the optimization process due to the change in shape of the structure.

Chapter 6

Discussions, Contributions and Conclusions, Future Work, and Publications

6.1 Discussions

This study presented an efficient, accurate and robust methodology for nonlinear analysis and design optimization of thin-walled structures. The proposed optimization method seems to be suitable for the cases in which the shape of the structure can be defined by a few number of design variables, and the nodal positions in the finite element mesh are linked to the design variables by a suitable relation. It should be mentioned that structural optimization techniques based on optimality criteria method may suffer convergence difficulties and other numerical instabilities when they are applied to the optimum design of large structures. This is why stochastic search techniques such as genetic algorithm and simulated annealing have recently found wide application in structural optimization.

It should also be mentioned that recently, some doubts have been raised about the mathematical convergence of facet elements [164]. In particular, when refining the mesh, finite element solutions are expected to converge to the exact solution of a well-

defined mathematical model. However, some numerical experiments have shown that facet shell elements may not exactly converge when the mesh is refined, although their results lie within a few percent of the reference values [164]. It is believed that best shell elements are formulated using 3D continuum mechanics incorporating shell theory assumptions. However, facet element was used in this study due to its computational efficiency and also since the formulation of corotational approach using curved elements is extremely difficult to perform and it is not even well developed.

During the nonlinear deformations, plastic zones may appear in the structure which affects the nonlinear behavior significantly. This study does not consider material nonlinearity during deformation. Also in the case of composite structures, local failures inside the laminate might be initiated if the interlaminar stresses are very high and allowable strengths of the composite ply are low. Again this study does not consider the failure of composite materials, during nonlinear deformations.

6.2 Contributions and conclusions

Contributions and conclusions of this study can be categorized into the following two major groups:

1) Development of the new shell elements, applicable in corotational non-linear analysis:

- A new thin shell element was formulated based on the combination of DKT (Discrete Kirchhoff Triangle) plate bending element and OPT (OPTimal) membrane element.

- A new moderately thick shell element was formulated based on the combination of DKMT (Discrete Kirchhoff-Mindlin Triangle) plate bending element and OPT (OPTimal) membrane element.
- The membrane-bending coupling terms in the stiffness matrix were determined for the case of laminated composite plates and shells.
- Inconsistent stress stiffness was formulated based on the shape functions of BCIZ plate bending element and LST(Ret) membrane element.
- A robust non-linear analysis program based on the corotational method has been developed and applied on numerous benchmark problems with geometric non-linearity (large displacements and rotations, and small strains) using new shell elements. Solutions of these problems showed very good agreement with the analytical solutions.
- Based on the numerical results, it is concluded that using membrane elements other than OPT usually overestimates the stiffness of the structure and leads to erroneous results. Based on the results of this study, whenever the membrane action has a considerable role in providing the stiffness of the structure, the choice of the membrane element can significantly affect the nonlinear response of the structure.
- It was shown that analysis using the proposed elements will lead to the accurate result using less number of the elements compared to the other shell elements. This would be a great advantage when performing nonlinear analysis, since any reduction in number of elements affects the computational time significantly.

2) Development of the optimization methodology for shape optimization of thin-walled structures with geometric nonlinearity:

- Two optimality criteria have been proposed and combined with a geometrically nonlinear analysis program. The proposed method changes the shape of the structure so that the average strain energy densities (or average strain energy variation for the case of thickness optimization) for all design variables become uniform.
- It was shown that the proposed method converges to the optimum shape in less number of iterations compared to the standard gradient-based methods of optimization without performing the sensitivity analysis.
- It was shown that in general case of the combination of membrane and bending deformations, using USED criterion instead of UASEV is unjustified, and only in case of pure membrane or pure bending behavior results based on USED and UASEV criteria are the same.
- A methodology for establishing rib location and design optimization of stiffened plates based on an optimality criterion for thickness optimization was presented. Applying the proposed criterion for thickness optimization through an iterative process, it is possible to find the potential locations to add the stiffeners and increase the strength of the plate while consuming the same amount of material.
- The effect of local buckling in optimization of stiffened panels was studied and a robust method of optimization was presented to consider the change of the buckling mode during the optimization process. In this method always the first

buckling mode (whether it is local or global) is captured and selected in the form of an initial imperfection in nonlinear analysis during the optimization process.

6.3 Future work

The work done in this thesis can be extended in the following directions:

- Dynamic corotational analysis of thin-walled structures:

In this research, dynamic analysis of geometrically nonlinear thin-walled structures could be formulated using corotational method. Dynamic analysis of nonlinear structures using this method has not been developed yet. Results of this study would be extremely useful, since recently corotational method has gained a lot of popularity and there is an ongoing effort to use this method in commercial structural analysis codes.

- Nonlinear structural analysis using genetic algorithm:

In traditional methods of nonlinear structural analysis, equilibrium equations are satisfied by minimization of potential energy through a gradient-based method (e.g. Newton-Raphson method). As an alternative method, genetic algorithm may be used for minimization of potential energy. This method may be used for both geometrically and materially nonlinear structures.

- Design optimization of composite laminated structures using optimality criteria:

In this study, optimality criteria could be presented in order to optimize the fiber angles and thickness of the layers in composite laminates. Failure of the

composite laminate as well as geometric nonlinearity could be considered in this research.

- Optimum design of composite stiffened panels:

In this research, the present study could be extended to stiffened panels made of composite laminates, and their strength could be maximized subject to local and global bucklings. Failure of the composite laminate could be also considered in this study. Applications of this study would be mainly in aerospace industries.

6.4 Publications

The work presented in this thesis is based on the following journal and conference papers, and presentations:

Journal papers, published or accepted for publication:

- Khosravi P., Ganesan R., Sedaghati R., “Corotational nonlinear analysis of thin plates and shells using a new shell element”, *International Journal for Numerical Methods in Engineering*, (69)(4), pp. 859–885, 2007.
- Khosravi P., Sedaghati R., Ganesan R., “Optimization of geometrically nonlinear thin shells subject to displacement and stability constraints”, *AIAA Journal*, (45)(3), pp. 684–692, 2007.
- Khosravi P., Ganesan R., Sedaghati R., “An efficient facet shell element for corotational nonlinear analysis of thin and moderately thick laminated composite structures”, *Computers and Structures*, In press.

- Khosravi P., Sedaghati R., Ganesan R., “Optimization of stiffened panels considering geometric nonlinearity”, *Journal of Mechanics of Materials and Structures*, In press.

Journal papers, to be communicated:

- Khosravi P., Ganesan R., Sedaghati R., “Optimization of thin-walled structures with geometric nonlinearity for maximum critical load using optimality criteria”.
- Khosravi P., Sedaghati R., Ganesan R., “Effect of local buckling on the optimum design of stiffened panels”.

Conference papers:

- Khosravi P., Ganesan R., Sedaghati R., “Limit load analysis of thin geometrically nonlinear structures using a new shell element”, *47th AIAA/ ASME/ ASCE/ AHS/ ASC Structures, Structural Dynamics, and Materials Conference*, 1–4 May 2006, Newport, RI, US.
- Khosravi P., Sedaghati R., Ganesan R., “Shape optimization of thin-walled structures based on a new shell element and uniform strain energy density criterion”, *The Eighth International Conference on Computational Structures Technology*, 12–15 September 2006, Las Palmas de Gran Canaria, Spain.
- Khosravi P., Ganesan R., Sedaghati R., “Nonlinear analysis of composite plates and shells using a new shell element”, *III European Conference on Computational Mechanics Solids, Structures and Coupled Problems in Engineering*, 5–8 June 2006, Lisbon, Portugal.

- Khosravi P., Ganesan R., Sedaghati R., “Optimality criteria for shape optimization of thin plate and shell structures”, *21st Canadian Congress of Applied Mechanics*, 3–7 June 2007, Toronto, Canada.

Poster presentations:

- Khosravi P., Ganesan R., Sedaghati R., “Nonlinear analysis of thin-walled composite structures using a new shell element”, *Centre for Applied Research on Polymers and Composites, CREPEC*, 2005, University of Montreal, Montreal, Canada.
- Khosravi P., Ganesan R., Sedaghati R., “Nonlinear analysis of laminated composite structures using optimal membrane element, and considering shear deformation”, *Centre for Applied Research on Polymers and Composites, CREPEC*, 2006, Ecole de Technologie Supérieure, Montreal, Canada.

References

- [1] Bendsøe, M. P., “Optimal shape design as a material distribution problem”, *Structural Optimization*, **1**, 1989, pp. 193-202.
- [2] Bendsøe, M. P. and Mota Soares, C. A., “Topology design of structures”, in *Proc. NATO ARW. Sesimbra*, 1993, Kluwer, Dordrecht.
- [3] Bendsøe, M. P. and Sigmund, O., “Material interpolation schemes in topology optimization”, *Archive of Applied Mechanics*, **69**, 1999, pp. 635-654.
- [4] Bendsøe, M. P. and Sigmund, O., *Topology optimization theory, methods and applications*, 2003, Springer, Berlin.
- [5] Lógó, J. and Ghaemi, M., “Topology optimization by SIMP method”, in *Proceedings of the 9th International Conference on Numerical Methods and Computational Mechanics*, edited by A. Galántay and G. Szeidl, 2002, Miskolc, Hungary, pp. 165-166.
- [6] Maute, K., Swartz, S., and Ramm, E., “Adaptive topology optimization of elastoplastic structures”, *Structural Optimization*, **15**, 1998, pp. 81-91.
- [7] Rozvany, G. I. N., *Optimization in structural mechanics*, CISM courses and lectures notes 374, 1997, Springer Verlag, Vienna.

- [8] Kiusalaas, J., “Optimal design of structures with buckling constraints”, *International Journal of Solids and Structures*, **9**, 1973, pp. 863–878.
- [9] Khot, N. S., Venkayya, V. B., and Berke, L., “Optimum structural design with stability constraints”, *International Journal for Numerical Methods in Engineering*, **10**, 1976, pp. 1097–1114.
- [10] Khot, N. S., “Optimal design of a structure for system stability for a specified eigenvalue distribution”, *International Symposium on Optimum Structural Design*, 1981, University of Arizona, Tucson, AZ.
- [11] Khot, N. S., “Nonlinear analysis of optimized structure with constraints on system stability”, *AIAA Journal*, **21(8)**, 1983, pp. 1181–1186.
- [12] Levy, R., and Perng, H. S., “Optimization for nonlinear stability”, *Computers and Structures*, **30(3)**, 1988, pp. 529–535.
- [13] Szyskowski, W., Watson, L. G., and Fietkiewicz, B., “Bimodal optimization of frames for maximum stability”, *Computers and Structures*, **32(5)**, 1989, pp. 1093–1104.
- [14] Canfield, R. A., “Design of frames against buckling using a rayleigh quotient approximation”, *AIAA Journal*, **31(6)**, 1993, pp. 1144–1149.
- [15] Levy, R., “Optimal design of trusses for overall stability”, *Computers and Structures*, **53(5)**, 1994, pp. 1133–1138.
- [16] Reitinger, R., Bletzinger, K. U. and Ramm, E., “Shape optimization of buckling sensitive structures”, *Computer Systems in Engineering*, **5(1)**, 1994, pp. 65–75.

- [17] Reitinger, R. and Ramm, E., “Buckling and imperfection sensitivity in the optimization of shell structures”, *Thin-Walled Structures*, **23**, 1995, pp. 159-177.
- [18] Parente, E., *Análise de Sensibilidade e Otimização de Forma de Estruturas Geometricamente Não-Lineares— Sensitivity analysis and shape optimization of geometrically nonlinear structures*, Ph.D. Thesis, 2000, Civil Engineering Department, PUC-Rio, Brazil.
- [19] Lee, S. J., and Hintonz, E., “Dangers inherited in shells optimized with linear assumptions”, *Computers and Structures*, **78**, 2000, pp. 473–486.
- [20] Thompson, J. M. T., and Hunt, G. W., *A general theory of elastic instability*, 1973, Wiley, New York.
- [21] Zienkiewicz, O. C. and Taylor, R. L., *The finite element method*, (Vol. 1&2, forth edition), 1989 & 1991, McGraw Hill, London.
- [22] Bathe, K. J., *Finite element procedures*, 1996, Prentice Hall, Englewood Cliffs.
- [23] Mohan, P., *Development and applications of a flat triangular element for thin laminated shells*, Ph.D. Dissertation, 1997, Department of Aerospace Engineering, Virginia Polytechnic Institute and State University, Blacksburg, Virginia.
- [24] Chapelle, D., “A locking-free approximation of curved rods by straight beam elements”, *Numerische Mathematik*, **77**, 1997, pp. 299–322.
- [25] Allman, D. J., “A compatible triangular element including vertex rotations for plane elasticity analysis”, *Computers and Structures*, **19**, 1984, pp. 1–8.

- [26] Allman, D. J., “Evaluation of the constant strain triangle with drilling rotations”, *International Journal for Numerical Methods in Engineering*, **26**, 1988, pp. 2645–2655.
- [27] Felippa, C. A., “A study of optimal membrane triangles with drilling freedoms”, *Computer Methods in Applied Mechanics and Engineering*, **192(16)**, 2003, pp. 2125–2168.
- [28] Bazeley, G. P., Cheung, Y. K., Irons, B. M. and Zienkiewicz, O. C., “Triangular elements in plate bending- conforming and nonconforming solutions”, *Proceeding First Conference on Matrix in Structural Mechanics*, 1966, Air Force Institute of Technology, Dayton, Ohio, pp. 66–80.
- [29] Batoz, J. L., “An explicit formulation for an efficient triangular plate-bending element”, *International Journal for Numerical Methods in Engineering*, **18**, 1982, pp. 1077–1089.
- [30] Batoz, J. L., Bathe, K. J. and Ho, L. W., “A study of three-node triangular plate bending elements”, *International Journal for Numerical Methods in Engineering*, **15**, 1980, pp. 1771–1812.
- [31] Katili, I., “A new discrete Kirchhoff-Mindlin element based on Mindlin-Reinssner plate theory and assumed shear strain fields- Part I: An extended DKT element for thick-plate bending analysis”, *International Journal for Numerical Methods in Engineering*, **36**, 1993, pp. 1859–1883.

- [32] Felippa, C. A., “A systematic approach to the element-independent corotational dynamics of finite elements”, *IASS-IACM 2000, Fourth International Colloquium on Computation of Shell and Spatial Structures*, Chania-Crete, Greece, June, 2000.
- [33] Wempner, G. A., “Finite elements, finite rotations and small strains of flexible shells”, *International Journal of Solids and Structures*, **5**, 1969, pp. 117-153.
- [34] Belytschko, T. and Hsieh, B. J., “Non-linear transient finite element analysis with convected co-ordinates”, *International Journal for Numerical Methods in Engineering*, **7**, 1973, pp. 255–271.
- [35] Bergan, P. G. and Horrigmoe, G., “Incremental variational principles and finite element models for nonlinear problems”, *Computer Methods in Applied Mechanics and Engineering*, **7**, 1976, pp. 201-217.
- [36] Argyris, J., “An excursion into large rotations”, *Computer Methods in Applied Mechanics and Engineering*, **32**, 1982, pp. 85–155.
- [37] Rankin, C. C. and Brogan, F. A., “An element independent corotational procedure for the treatment of large rotations”, *Journal of Pressure Vessel Technology*, **108**, 1986, pp. 165–174.
- [38] Szwabowicz, M. L., “Variational formulation in the geometrically nonlinear thin elastic shell theory”, *International Journal of Engineering Science*, **22**, 1986, pp. 1161-1175.

- [39] Rankin, C. C. and Nour-Omid, B., “The use of projectors to improve finite element performance”, *Computers and Structures*, **30**, 1988, pp. 257–267.
- [40] Nour-Omid, B. and Rankin, C. C., “Finite rotation analysis and consistent Linearization using projectors”, *Computer Methods in Applied Mechanics and Engineering*, **93**, 1991, pp. 353–384.
- [41] Crisfield, M. A., “A consistent co-rotational formulation for nonlinear three-dimensional beam elements”, *Computer Methods in Applied Mechanics and Engineering*, **81**, 1990, pp. 131–150.
- [42] Peng, X. and Crisfield, M. A., “A consistent co-rotational formulation for shells using the constant stress/constant moment triangle”, *International Journal for Numerical Methods in Engineering*, **35(9)**, 1992, pp. 1829–1847.
- [43] Pacoste, C., “Co-rotational flat facet triangular elements for shell instability analyses”, *Computer Methods in Applied Mechanics and Engineering*, **156(1)**, 1998, pp. 75–110.
- [44] Battini, J. M. and Pacoste, C., “Co-rotational beam elements with warping effects in instability problems”, *Computer Methods in Applied Mechanics and Engineering*, **191(17)**, 2002, pp. 1755–1789.
- [45] Battini, J. M. and Pacoste, C., “Plastic instability of beam structures using co-rotational elements”, *Computer Methods in Applied Mechanics and Engineering*, **191(51)**, 2002, pp. 5811–5831.

- [46] Felippa, C. A., “Unified formulation of small-strain corotational finite elements: I. theory”, *Computer Methods in Applied Mechanics and Engineering*, **194**(21–24), 2005, pp. 2285–2335.
- [47] Marguerre, K., “Die mittragende Breite der gedrückten Platte”, *Luftfahrtforschung*, **14**(3), 1937, pp. 121-128.
- [48] Kromm, A. and Marguerre, K., “Verhalten eines von Schub- und Druckkräften beanspruchten Plattenstreifens oberhalb der Beulgrenze”, *Luftfahrtforschung*, **14**(12), 1937, pp. 627-639.
- [49] Levy, S., *Bending of rectangular plates with large deflections*, 1942, NACA Report No. 737.
- [50] Paik, J. K., Thayamballi, A. K., Lee, S. K. and Kang, S. J., “A semi-analytical method for the elastic-plastic large deflection analysis of welded steel or aluminum plating under combined on-plane and lateral pressure loads”, *Thin-Walled Structures*, **39**(2), 2001, pp. 125-152.
- [51] Ueda, Y., Rashed, S. M. H. and Paik, J. K., “An incremental galerkin method for plates and stiffened plates”, *Computers and Structures*, **27**(1), 1987, pp. 147-156.
- [52] Paik, J. K., Thayamballi, A. K. and Kim, B. J., “Large deflection orthotropic plate approach to develop ultimate strength formulations for stiffened panels under combined biaxial compression/tension and lateral pressure”, *Thin-Walled Structures*, **39**(3), 2001, pp. 215-246.

- [53] Paik, J. K. and Kim, B. J., “Ultimate strength formulations for stiffened panels under combined axial load, in-plane bending and lateral pressure: a benchmark study”, *Thin-Walled Structures*, **40(1)**, 2002, pp. 45-83.
- [54] Byklum, E. and Amdahl, J., “A simplified method for elastic large deflection analysis of plates and stiffened panels due to local buckling”, *Thin-Walled Structures*, **40(11)**, 2002, pp. 925-953.
- [55] Byklum, E., Steen, E. and Amdahl, J., “A semi-analytical model for global buckling and postbuckling analysis of stiffened panels”, *Thin-Walled Structures*, **42(5)**, 2004, pp. 701-717.
- [56] Byklum, E., *Ultimate strength analysis of stiffened steel and aluminium panels using semi-analytical methods*, PhD Thesis, 2002, Norwegian University of Science and Technology.
- [57] Koiter, W. T., *Over de stabiliteit van het elastisch evenwicht*, *Ph.D. Thesis*, *Polytechnic Institute Delft*, 1945, (*English translation: On the stability of elastic equilibrium*), 1967, NASA TT F-10, 833.
- [58] Roorda, J., “On the buckling of symmetric structural systems with first and second order imperfection”, *International Journal of Solids and Structures*, **4**, 1968, pp. 1137-1148.
- [59] Roorda, J., “Stability of structures with small imperfections”, *Journal of Engineering Mechanics Division ASCE*, **91(1)**, 1965, pp. 87–106.

- [60] Arbocz, J. and Babcock, C. D., “The effect of general imperfections on the buckling of cylindrical shells”, *Journal of Applied Mechanics*, **36(1)**, 1969, pp. 28–38.
- [61] Hutchinson, J. W., “Axial buckling of pressurized imperfect cylindrical shells”, *AIAA Journal*, **3**, 1965, pp. 1461–1466.
- [62] Arbocz, J., “The effects of initial imperfections on shell stability”, *In Thin Shell Structures—Theory, Experiment and Design* Edited by Fung YC. and Sechler EE., 1974, Prentice-Hall, Englewood Cliffs, N. J., pp. 205–245.
- [63] Godoy, L. A. and Mook, D. T., “Higher-order sensitivity to imperfections in bifurcation buckling analysis”, *International Journal of Solids and Structures*, **33(4)**, 1996, pp. 511–520.
- [64] Deml, M. and Wunderlich, W., “Direct evaluation of the worst imperfection shape in shell buckling”, *Computer Methods in Applied Mechanics and Engineering*, **149**, 1997, pp. 201–222.
- [65] Wunderlich, W. and Albertin, U., “Buckling behaviour of imperfect spherical shells”, *International Journal of Non-Linear Mechanics*, **37**, 2002, pp. 589–604.
- [66] Singer, J., Arbocz, J. and Weller, T., “*Buckling experiments*, Vol. 1, 1998, Wiley, New York.
- [67] Arbocz, J., Potier-Ferry, M., Singer, J. and Tvergaard, V., *Buckling and post-buckling*, 1985, Springer-Verlag, Berlin.

- [68] Ohsaki, M. and Uetani, K., “Sensitivity analysis of bifurcation load of finite dimensional symmetric systems”, *International Journal of Numerical Methods in Engineering*, **39**, 1996, pp. 1707–1720.
- [69] Ohsaki, M., Uetani, K. and Takeuchi, M., “Optimization of imperfection-sensitive symmetric systems for specified maximum load factor”, *Computer Methods in Applied Mechanics and Engineering*, **166**, 1998, pp. 349–362.
- [70] Fraser, W. B. and Budiansky, B., “The buckling of a column with random initial deflections”, *Journal of Applied Mechanics*, **36**, 1969, pp. 232–240.
- [71] Roorda, J., *Buckling of elastic structures*, 1980, University of Waterloo Press, Waterloo.
- [72] Amazigo, J. C., “Buckling under axial compression of long cylindrical shell with random axisymmetric imperfections”, *Quarterly Applied Mathematics*, **26**, 1969, pp. 537–566.
- [73] Cederbaum, G. and Arbocz, J., “On the reliability of imperfection-sensitive long isotropic cylindrical shells”, *Structural Safety*, **18(1)**, 1996, pp. 1–9.
- [74] Godoy, L. A., Barbero, E. J. and Raftoyiannis, I., “Interactive buckling analysis of fiber-reinforced thin-walled columns”, *Journal of Composite Materials*, **29(5)**, 1995, pp. 591–613.
- [75] Graves, S. T. R., *The ultimate strength of locally buckled columns of arbitrary length*, Ph.D. Thesis, 1966, Cambridge University, England.

- [76] Thompson, J. M. T and Lewis, G. M., “On the optimum design of thin-walled compression members”, *Journal of the Mechanics and Physics of Solids*, **22**, 1972, pp. 101–109.
- [77] Van der Neut A., “The sensitivity of thin-walled compression members to column axis imperfection”, *International Journal of Solid and Structures*, **9**, 1973, pp. 999–1011.
- [78] Tvergaard, V., “Influence of postbuckling behavior in optimum design of stiffened panels”, *International Journal of Solid and Structures*, **9**, 1973, pp. 1519–1534.
- [79] Byskov, E. and Hutchinson, J. W., “Mode interaction in axially stiffened cylindrical shells”, *AIAA Journal*, **15(7)**, 1977, pp. 941–948.
- [80] Koiter, W. T. and Pignataro, M., *An alternative approach to the interaction of local and overall buckling in stiffened panels*, In: Budiansky B. (Ed.), *Buckling of structures*, 1976, Springer, New York, pp. 133–148.
- [81] Koiter, W. T. and Pignataro, M., *General theory of mode interaction in stiffened plate and shell structures*, 1976, Report WTHD-19, Delft University of Technology, Delft, The Netherlands.
- [82] Das, P. K. and Garside, J. E., *Structural redundancy for continuous and discrete systems*, 1991, Ship Structure Committee, Report No. SSC-354.

- [83] Hughes, O. F., Nikolaidis, E., Ayyub, B., White, G. and Hess, P. E., “*Uncertainty in strength models for marine structures*, 1994, Ship Structure Committee, Report No. SSC-375.
- [84] Rigo, P., Moan, T., Frieze, P. A. and Chryssanthopoulos, M., “Benchmarking of ultimate strength prediction for longitudinally stiffened panels”, *Proceedings of the Sixth International Symposium on Practical Design of Ship and Mobile Units (PRADS95)*, Seoul, September, **2**, 1995, pp. 869-882.
- [85] Paik, J. K. and Kim, D. H., “A benchmark study of the ultimate compressive strength formulations for stiffened panels”, *Journal of Research Institute of Industrial Technology; Pusan National University*, **53**, 1997, pp. 373-405.
- [86] Tanaka, Y. and Endo, H., “Ultimate strength of stiffened plates with their stiffeners locally buckled in compression”, *Journal of the Society of Naval Architects of Japan*, **164**, 1988, pp. 456-467.
- [87] Hu, S. Z., Chen, Q., Pegg, N. and Zimmerman, T. J. E., “Ultimate collapse tests of stiffened plate ship structural units”, *Marine Structures*, **10**, 1997, pp. 587-610.
- [88] Hopperstad, O. S., Langseth, M. and Tryland, T., “Ultimate strength of aluminum alloy outstands in compression: experiments and simplified analysis”, *Thin-Walled Structures*, **34(4)**, 1999, pp. 279-294.
- [89] Smith, C. S., Davidson, P. C., Chapman, J. C. and Dowling, P. J., “Strength and stiffness of ships plating under in-plane compression and tension”, *Transactions of The Royal Institution of Naval Architects*, **130**, 1988, pp. 277-296.

- [90] Smith, C. S., Anderson, N., Chapman, J. C., Davidson, P. C. and Dowling, P. J.,
 “Strength of stiffened plating under combined compression and lateral pressure”,
Transactions of The Royal Institution of Naval Architects, **134**, 1992, pp. 131-148.
- [91] Davidson, P. C., Chapman, J. C., Smith, C. S. and Dowling, P. J., “The design
 of plate panels subject to in-plane shear and biaxial compression”, *Transactions
 of The Royal Institution of Naval Architects*, **132**, 1990, pp. 267-286.
- [92] Davidson, P. C., Chapman, J. C., Smith, C. S. and Dowling, P. J., “The design
 of plate panels subject to biaxial compression and lateral pressure”, *Transactions
 of The Royal Institution of Naval Architects*, **134**, 1992, pp. 149-154.
- [93] Paik, J. K., Thayamballi, A. K. and Park, Y. I., “Local buckling of stiffeners in
 ship plating”, *Journal of Ship Research*, **42(1)**, 1998, pp. 56-67.
- [94] Hughes, O. F. and Ma, M., “Elastic tripping analysis of asymmetrical stiffeners”,
Computers and Structures, **60(3)**, 1996, pp. 369-389.
- [95] Hughes, O. F. and Ma, M., “Inelastic analysis of panel collapse by stiffener
 buckling”, *Computers and Structures*, **61(1)**, 1996, pp. 107-117.
- [96] Hu, Y., Chen, B. and Sun, J., “Tripping of thin-walled stiffeners in the axially
 compressed stiffened panel with lateral pressure”, *Thin-Walled Structures*, **37(1)**,
 2000, pp. 1-26.
- [97] Stroud, W. J. and Agranoff, N., *Minimum-mass design of filamentary compos-
 ite panels under combined loads: Design procedure based on a rigorous buckling
 analysis*, 1977, NASA-TN D-8417.

- [98] Bushnell, D., “PANDA2 - Program for minimum weight design of stiffened, composite, locally buckled panels”, *Computers and Structures*, **25(4)**, 1987, pp. 469–605.
- [99] Butler, R. and Williams, F. W., “Optimum design using VICONOPT, a buckling and strength constraint program for prismatic assemblies of anisotropic plates”, *Computers and Structures*, **43(4)**, 1992, pp. 699–708.
- [100] Butler, R., “Optimum Design and evaluation of stiffened panels with practical loading”, *Computers and Structures*, **52(6)**, 1994, pp. 1107–1118.
- [101] Bushnell, D. and Bushnell, W. D., “Optimum design of Composite Stiffened Panels under combined loads”, *Computers and Structures*, **55(5)**, 1995, pp. 819–856.
- [102] Brosowski, B. and Ghavami, K., “Multi-criteria optimal design of stiffened plates II. Mathematical modelling of the optimal design of longitudinally stiffened plates”, *Thin-Walled Structures*, **28(2)**, 1997, pp. 179–198.
- [103] Haftka, R. T. and Grandhi, R. V., “Structural shape optimization a survey”, *Computer Methods in Applied Mechanics and Engineering*, **30**, 1982, pp. 263–284.
- [104] Herskovits, J., *Proceedings of the structural optimization the world congress on optimal design of structural systems*, 1993, Federal University of Rio de Janeiro, Brazil.
- [105] Olhoff, N. and Rozvany, G., *Structural and multidisciplinary optimization*, 1995, Pergamon Press, Oxford.

- [106] Khot, N. S., and Kamat, M. P., “Minimum weight design of truss structures with geometric nonlinear behavior”, *AIAA Journal*, **23(1)**, 1985, pp. 139–144.
- [107] Kamat, M. P. and Ruangsilasingha, P., “Optimization of space trusses against instability using design sensitivity derivatives”, *Engineering Optimization*, **8**, 1985, pp. 177–188.
- [108] Smaoui, H. and Schmit, L. A., “An integrated approach to the synthesis of geometrically non-linear structures”, *International Journal for Numerical Methods in Engineering*, **26**, 1979, pp. 555–570.
- [109] Ringertz, U. T., *Optimal design of nonlinear shell structures*, 1991, Report FFA TN 1991-18, Structures Department, The Aeronautical Research Institute of Sweden.
- [110] Le Tallec, P. and Halard, M., “Second order methods for the optimal design of non-linear structures”, *In Computational Methods in Applied Sciences*, ed. Ch. Hirsch, Elsevier Science Publishers B.V., Amsterdam, 1992, pp. 247–251.
- [111] Wu, C. C. and Arora, J. S., “Design sensitivity analysis of non-linear buckling load”, *Computational Mechanics*, **3**, 1988, pp. 129–140.
- [112] Ryu, Y. S., Haririan, M., Wu, C. C. and Arora, J. S., “Structural design sensitivity analysis of nonlinear response”, *Computers and Structures*, **21(12)**, 1985, pp. 245–255.

- [113] Park, J. S. and Choi, K. K., “Design sensitivity analysis of critical load factor for nonlinear structural systems”, *Computers and Structures*, **36(5)**, 1990, pp. 823-838.
- [114] de Boer, H. and van Keulen, F., “Improved semi-analytic design sensitivities for a linear and finite rotation shell element”, *In WCSMO-2, 2nd World Congress of Structural and Multidisciplinary Optimization*, Gutkowski W, Mroz Z (eds), 1997, Zakopane, Poland, pp. 199-204.
- [115] de Boer, H. and van Keulen, F., “Refined semi-analytical design sensitivities”, *International Journal of Solids and Structures*, **37(46-47)**, 2000, pp. 6961-6980.
- [116] Parente, E. and Vaz, L. E., “Shape sensitivity analysis of geometrically nonlinear structures”, *Design Optimization*, **1(3)**, 1999, pp. 305-327.
- [117] Parente, E. and Vaz, L. E., “Improvement of semi-analytical design sensitivities of non-linear structures using equilibrium relations”, *International Journal for Numerical Methods in Engineering*, **50(9)**, 2001, pp. 2127-2142.
- [118] Parente, E. and Vaz, L. E., “On evaluation of shape sensitivities of non-linear critical loads”, *International Journal for Numerical Methods in Engineering*, **56**, 2003, pp. 809-846.
- [119] Mróz, Z. and Haftka, R. T., “Design sensitivity analysis of non-linear structures in regular and critical states”, *International Journal of Solids and Structures*, **31(15)**, 1994, pp. 2071-2098.

- [120] Mróz, Z. and Piekarski, J., “Sensitivity analysis and optimal design of non-linear structures”, *International Journal for Numerical Methods in Engineering*, **42**, 1998, pp. 1231-1262.
- [121] Saka, M. P., “Optimum design of space trusses with buckling constraints”, *Proceedings of the Third International Conference on Space Structures*, 1984, University of Surrey, Guildford, UK.
- [122] Saka, M. P. and Ulker, M., “Optimum design of geometrically nonlinear space trusses”, *Computers and Structures*, **42**, 1992, pp. 289–299.
- [123] Khan, M. R., “Optimality criterion techniques applied to frames having general cross-sectional relationships”, *AIAA Journal*, **22(5)**, 1984, pp. 669–676.
- [124] Khan, M. R., Willmert, K. D. and Thornton, W. A., “A new optimality criterion method for large scale structures”, *Proceedings of AIAA/ASME 19th SDM Conference*, 1978, Bethesda, USA, pp. 47–58.
- [125] Sedaghati, R. and Tabarrok, B., “Optimum design of truss structures undergoing large deflections subject to a system stability constraint”, *International Journal of Numerical Methods in Engineering*, **48(3)**, 2000, pp. 421–434.
- [126] Grandhi, R. V. and Venkayya, V. B., “Structural optimization with Frequency Constraints”, *AIAA Journal*, **26**, 1988, pp. 858–866.
- [127] Lógó, J., “New types of optimal topologies by iterative method”, *Mechanics based design of structures and machines*, **33**, 2005, pp. 149-171
- [128] Arora, J. S., *Introduction to optimum design*, 1989, McGraw-Hill.

- [129] Gallagher, R. H., *Fully stressed design*, In: Gallagher, R. H., Zienkiewicz, O. C., eds. *Optimum Structural Design Theory and Applications*., 1973, Wiley, London, pp. 19-32.
- [130] Prager, W. and Taylor, J. E., "Problems of optimal structural design", *Journal of Applied Mechanics, ASME*, **35**, 1968, pp. 102-106.
- [131] Venkayya, V. B., Khot, N. S. and Reddy, V. S., *Optimization of structures based on the study of strain energy distribution*, 1968, AFFDLTR-68-150.
- [132] Venkayya, V. B., Khot, N. S. and Reddy, V. S., *Energy distribution in an optimum structural design*, 1969, AFFDLTR-68-156.
- [133] Venkayya, V. B., "Design of optimum structures", *Computers and Structures*, **1**, 1971, pp. 265-309.
- [134] Berke, L., *An efficient approach to the minimum weight design of deflection limited design*, 1970, AFFDL-TM-70-4-FDTR, Wright-Patterson AFB.
- [135] Gellatly, R. A. and Berke, L., *Optimal structural design*, 1971, AFFDL-TM-70-165.
- [136] Gellatly, R. A. and Berke, L., *Optimality criterion based algorithms*, in *Optimum Structural Design Theory and Applications*, edited by R. H. Gallagher and O. C. Zienkiewicz, 1973, Wiley, London, pp. 33-49.
- [137] Nagtegaal, J. C., "A new approach to optimal design of elastic structures", *Computer Methods in Applied Mechanics and Engineering*, **2**, 1973, pp. 255-264.

- [138] Berke, L. and Khot, N. S., “Use of optimality criteria methods for large scale system”, *Agard Lecture Series*, **70**, 1974, pp. 1-29.
- [139] Khot, N. S., Berke, L. and Venkayya, V. B., “Comparison of optimality criteria algorithms for minimum weight design of structures”, *AIAA Journal*, **17**, 1979, pp. 182-190.
- [140] Bendsøe, M. P. and Kikuchi, N., “Generating optimal topologies in structural design using a homogenization method”, *Computer Methods in Applied Mechanics and Engineering*, **71**, 1988, pp. 197-224.
- [141] Rozvany, G. I. N., Bendsøe, M. P. and Kirsch U., “Layout optimization of structures”, *Applied Mechanics Reviews*, **48**, 1995, pp. 41-111.
- [142] Stok, B. and Mihelic, A., “Two-stage design optimization of shell structures”, *Structural Engineering Review*, **8**, 1996, pp. 91-97.
- [143] Chung, J. and Lee, K., “Optimal design of rib structures using the topology optimization technique”, *Proceedings of the Institution of Mechanical Engineers, Part C*, **211**, 1997, pp. 425-437.
- [144] Lee, T. H., Han, S. Y. and Lim, J. K., “Topology optimization of the inner reinforcement for an automobile hood using modal design sensitivity analysis”, *Key Engineering Materials*, **183-187**, 2000, pp. 439-444.
- [145] Lam, Y. C. and Santhikumar, S., “Automated rib location and optimization for plate structures”, *Structural and Multidisciplinary Optimization*, **25**, 2003, pp. 35-45.

- [146] Berthelot, J. M., *Composite Materials : Mechanical behaviour and structural analysis*, 1999, Springer, New York.
- [147] Cook, R. D., *Concepts and applications of finite element analysis*, 3rd edition, 1989, Wiley, New York.
- [148] Felippa, C. A., *Refined finite element analysis of linear and nonlinear two-dimensional structures*, Ph.D. Dissertation, 1966, Department of Civil Engineering, University of California at Berkeley, Berkeley, CA.
- [149] Batoz, J. L. and Dhett, G., “Incremental displacement algorithms for non-linear problems”, *International Journal for Numerical Methods in Engineering*, **14**, 1979, pp. 1262-1266.
- [150] Yang, Y. and Kuo, S., *Theory and analysis of nonlinear framed structures*, 1994, Prentice-Hall, Englewood Cliffs, NJ.
- [151] Rajan, S. D. and Belegundu, A. D., “Shape optimal design using fictitious loads”, *AIAA Journal*, **27(1)**, 1989, pp. 102–107.
- [152] Belegundu, A. D. and Rajan, S. D., “A shape optimization approach based on natural design variables and shape functions”, *Computer Methods in Applied Mechanics and Engineering*, **66**, 1988, pp. 87–106.
- [153] Díaz, A. R. and Sigmund, O., “Checkerboard patterns in layout optimization”, *Structural Optimization*, **10**, 1995, pp. 40-45.

- [154] Jog, C. S. and Haber, R. B., “Stability of finite elements models for distributed-parameter optimization and topology design”, *Computer Methods in Applied Mechanics and Engineering*, **130**, 1996, pp. 203-226.
- [155] Poulsen, T. A., “A simple scheme to prevent checkerboard patterns and one node connected hinges in topology optimization”, *Structural and Multidisciplinary Optimization*, **24**, 2002, pp. 396-399.
- [156] Sigmund, O. and Petersson, J., “Numerical instabilities in topology optimization-a survey on procedures dealing with checkerboards, mesh-dependencies and local minima”, *Structural Optimization*, **16**, 1998, pp. 68-75.
- [157] Zhou, M. , Shyy, Y. K. and Thomas, H. L., “Checkerboard and minimum member size control in topology optimization”, *Structure and Multidisciplinary Optimization*, **21**, 2001, pp. 152-158.
- [158] Gáspár, Z. S., Lógó, J. and Rozvany, G. I. N., “On design-dependent constraints and singular topologies”, *Structural and Multidisciplinary Optimization*, **24(4)**, 2002, pp. 338-342.
- [159] Paik, J. K. and Kim, B. J., “Ultimate strength formulations for stiffened panels under combined axial load, in-plane bending and lateral pressure: a benchmark study”, *Thin-Walled Structures*, **40(1)**, 2002, pp. 45-83.
- [160] Bushnell, D., “Nonlinear equilibrium of imperfect, locally deformed stringer-stiffened panels under combined in-plane loads”, *Computers and Structures*, **27(4)**, 1987, pp. 519-539.

- [161] Timoshenko, S. P. and Gere, J. M., *Theory of elastic stability*, 2nd edition, 1961, McGraw-Hill, New York.
- [162] Riks, E., “An incremental approach to the solution of snapping and buckling problems”, *International Journal of Solids and Structures*, **15**, 1979, pp. 529-551.
- [163] Crisfield, M. A., “A fast incremental/iterative solution procedure that handles snap-through”, *Computers and Structures*, **13**, 1981, pp. 55-62.
- [164] Chapelle, D., *The finite element analysis of shells—fundamentals*, 2003, Springer.